On-board Robotic Multi-pinhole SPECT System for Region-of-interest (ROI) Imaging

by

Susu Yan

Graduate Program in Medical Physics
Duke University

Date:_____

Approved:

_____

Fang-Fang Yin, Co-supervisor

_____

James E. Bowsher, Co-supervisor

_____

Sua Yoo

_____

Rachel C. Blitzblau

_____

James G. Colsher

Dissertation submitted in partial fulfillment of
the requirements for the degree of Doctor of Philosophy
in Graduate Program in Medical Physics
in the Graduate School
of Duke University

2014

ABSTRACT

On-board Robotic Multi-pinhole SPECT System for Region-of-interest (ROI) Imaging

by

Susu Yan

Graduate Program in Medical Physics
Duke University

Date:_____
Approved:

_____
Fang-Fang Yin, Co-supervisor

_____
James E. Bowsher, Co-supervisor

_____
Sua Yoo

_____
Rachel C. Blitzblau

_____
James G. Colsher

An abstract of a dissertation submitted in partial fulfillment of
the requirements for the degree of Doctor of Philosophy
in Graduate Program in Medical Physics
in the Graduate School
of Duke University

2014

Abstract

On-board image guidance, such as cone-beam CT (CBCT) and kV/MV 2D imaging, is essential in many radiation therapy procedures, such as intensity modulated radiotherapy (IMRT) and stereotactic body radiation therapy (SBRT). These imaging techniques provide predominantly anatomical information for treatment planning and target localization. Recently, studies have shown that treatment planning based on functional and molecular information about the tumor and surrounding tissue could potentially improve the effectiveness of radiation therapy. However, current on-board imaging systems are limited in their functional and molecular imaging capability. Single Photon Emission Computed Tomography (SPECT) is a candidate to achieve on-board functional and molecular imaging. Traditional SPECT systems typically take 20 minutes or more for a scan, which is too long for on-board imaging. A robotic multi-pinhole SPECT system was proposed in this dissertation to provide shorter imaging time by using a robotic arm to maneuver the multi-pinhole SPECT system around the patient in position for radiation therapy.

A 49-pinhole collimated SPECT detector and its shielding were designed and simulated in this work using the computer-aided design (CAD) software. The trajectories of robotic arm about the patient, treatment table and gantry in the radiation therapy room and several detector assemblies such as parallel holes, single pinhole and 49 pinholes collimated detector were investigated. The rail mounted system was

designed to enable a full range of detector positions and orientations to various crucial treatment sites including head and torso, while avoiding collision with linear accelerator (LINAC), patient table and patient.

An alignment method was developed in this work to calibrate the on-board robotic SPECT to the LINAC coordinate frame and to the coordinate frames of other on-board imaging systems such as CBCT. This alignment method utilizes line sources and one pinhole projection of these line sources. The model consists of multiple alignment parameters which maps line sources in 3-dimensional (3D) space to their 2-dimensional (2D) projections on the SPECT detector. Computer-simulation studies and experimental evaluations were performed as a function of number of line sources, Radon transform accuracy, finite line-source width, intrinsic camera resolution, Poisson noise and acquisition geometry. In computer-simulation studies, when there was no error in determining angles (α) and offsets (ϱ) of the measured projections, the six alignment parameters (3 translational and 3 rotational) were estimated perfectly using three line sources. When angles (α) and offsets (ϱ) were provided by Radon transform, the estimation accuracy was reduced. The estimation error was associated with rounding errors of Radon transform, finite line-source width, Poisson noise, number of line sources, intrinsic camera resolution and detector acquisition geometry. The estimation accuracy was significantly improved by using 4 line sources rather than 3 and also by using thinner line-source projections (obtained by better intrinsic detector resolution).

With 5 line sources, median errors were 0.2 mm for the detector translations, 0.7 mm for

the detector radius of rotation, and less than 0.5° for detector rotation, tilt and twist. In

experimental evaluations, average errors relative to a different, independent registration

technique were about 1.8 mm for detector translations, 1.1 mm for the detector radius of

rotation (ROR), 0.5° and 0.4° for detector rotation and tilt, respectively, and 1.2° for

detector twist.

Simulation studies were performed to investigate the improvement of imaging

sensitivity and accuracy of hot sphere localization for breast imaging of patients in

prone position. A 3D XCAT phantom was simulated in the prone position with nine hot

spheres of 10 mm diameter added in the left breast. A no-treatment-table case and two

commercial prone breast boards, 7 and 24 cm thick, were simulated. Different pinhole

focal lengths were assessed for root-mean-square-error (RMSE). The pinhole focal

lengths resulting in the lowest RMSE values were 12 cm, 18 cm and 21 cm for no table,

thin board, and thick board, respectively. In both no table and thin board cases, all 9 hot

spheres were easily visualized above background with 4-minute scans utilizing the 49-

pinhole SPECT system while seven of nine hot spheres were visible with the thick board.

In comparison with parallel-hole system, our 49-pinhole system shows reduction in

noise and bias under these simulation cases. These results correspond to smaller radii of

rotation for no-table case and thinner prone board. Similarly, localization accuracy with

the 49-pinhole system was significantly better than with the parallel-hole system for

both the thin and thick prone boards. Median localization errors for the 49-pinhole

system with the thin board were less than 3 mm for 5 of 9 hot spheres, and less than 6

mm for the other 4 hot spheres. Median localization errors of 49-pinhole system with the

thick board were less than 4 mm for 5 of 9 hot spheres, and less than 8 mm for the other

4 hot spheres.

Besides prone breast imaging, respiratory-gated region-of-interest (ROI) imaging

of lung tumor was also investigated. A simulation study was conducted on the potential

of multi-pinhole, region-of-interest (ROI) SPECT to alleviate noise effects associated with

respiratory-gated SPECT imaging of the thorax. Two 4D XCAT digital phantoms were

constructed, with either a 10 mm or 20 mm diameter tumor added in the right lung. The

maximum diaphragm motion was 2 cm (for 10 mm tumor) or 4 cm (for 20 mm tumor) in

superior-inferior direction and 1.2 cm in anterior-posterior direction. Projections were

simulated with a 4-minute acquisition time (40 seconds per each of 6 gates) using either

the ROI SPECT system (49-pinhole) or reference single and dual conventional broad

cross-section, parallel-hole collimated SPECT. The SPECT images were reconstructed

using OSEM with up to 6 iterations. Images were evaluated as a function of gate by

profiles, noise versus bias curves, and a numerical observer performing a forced-choice

localization task. Even for the 20 mm tumor, the 49-pinhole imaging ROI was found

sufficient to encompass fully usual clinical ranges of diaphragm motion. Averaged over

the 6 gates, noise at iteration 6 of 49-pinhole ROI imaging (10.9 μCi/ml) was

approximately comparable to noise at iteration 2 of the two dual and single parallel-hole, broad cross-section systems (12.4 µCi/ml and 13.8 µCi/ml, respectively). Corresponding biases were much lower for the 49-pinhole ROI system (3.8 µCi/ml), versus 6.2 µCi/ml and 6.5 µCi/ml for the dual and single parallel-hole systems, respectively. Median localization errors averaged over 6 gates, for the 10 mm and 20 mm tumors respectively, were 1.6 mm and 0.5 mm using the ROI imaging system and 6.6 mm and 2.3 mm using the dual parallel-hole, broad cross-section system. The results demonstrate substantially improved imaging via ROI methods. One important application may be gated imaging of patients in position for radiation therapy.

A robotic SPECT imaging system was constructed utilizing a gamma camera detector (Digirad 2020tc) and a robot (KUKA KR150-L110 robot). An imaging study was performed with a phantom (PET CT Phantom™), which includes 5 spheres of 10, 13, 17, 22 and 28 mm in diameter. The phantom was placed on a flat-top couch. SPECT projections were acquired with a parallel-hole collimator and a single-pinhole collimator both without background in the phantom, and with background at 1/10th the sphere activity concentration. The imaging trajectories of parallel-hole and pinhole collimated detectors spanned 180 degrees and 228 degrees respectively. The pinhole detector viewed a 14.7 cm-diameter common volume which encompassed the 28 mm and 22 mm spheres. The common volume for parallel-hole was a 20.8-cm-diameter cylinder which encompassed all five spheres in the phantom. The maneuverability of the robotic system

was tested by navigating the detector to trace the flat-top table while avoiding collision

with the table and maintaining the closest possible proximity to the common volume.

For image reconstruction, detector trajectories were described by radius-of-rotation and

detector rotation angle θ. These reconstruction parameters were obtained from the robot

base and tool coordinates. The robotic SPECT system was able to maneuver the parallel-

hole and pinhole collimated SPECT detectors in close proximity to the phantom,

minimizing impact of the flat-top couch on detector to center-of-rotation (COR) distance.

In no background case, all five spheres were visible in the reconstructed parallel-hole

and pinhole images. In with background case, three spheres of 17, 22 and 28 mm

diameter were readily observed with the parallel-hole imaging, and the targeted spheres

(22 and 28 mm diameter) were readily observed in the pinhole ROI imaging.

In conclusion, the proposed on-board robotic SPECT can be aligned to

LINAC/CBCT with a single pinhole projection of the line-source phantom. Alignment

parameters can be estimated using one pinhole projection of line sources. This alignment

method may be important for multi-pinhole SPECT, where relative pinhole alignment

may vary during rotation. For single pinhole and multi-pinhole SPECT imaging onboard

radiation therapy machines, the method could provide alignment of SPECT coordinates

with those of CBCT and the LINAC. In simulation studies of prone breast imaging and

respiratory-gated lung imaging, the 49-pinhole detector showed better tumor contrast

recovery and localization in a 4-minute scan compared to parallel-hole detector. On-

board SPECT could be achieved by a robot maneuvering a SPECT detector about patients in position for radiation therapy on a flat-top couch. The robot inherent coordinate frames could be an effective means to estimate detector pose for use in SPECT image reconstruction.

To My Beloved Grandparents

Contents

List of Tables

List of Figures

List of Abbreviations

2D	Two dimensional
3D	Three dimensional
BTV	Biological target volume
CAD	Computer-aided design
CBCT	Cone beam computed tomography
COR	Center of rotation
CTV	Clinical target volume
CV	Common Volume
DRR	Digital reconstructed radiography
FOV	Field of view
GTV	Gross tumor volume
IGRT	Image guidance radiation therapy
IMRT	Intensity modulated radiotherapy
ITV	Internal target volume
LEAP	Low energy all purpose
LEHR	Low energy high resolution
LINAC	Linear accelerator
MLEM	Maximum Likelihood Expectation Maximization
OAR	Organ at risk

OSEM	Ordered Subsets Expectation Maximization
PET	Positron emission tomography
PTV	Planning target volume
RMSE	Root-mean-square-error
ROI	Region of interest
ROR	Radius of rotation
SBRT	Stereotactic body radiation therapy
SPECT	Single photon emission computed tomography

Acknowledgements

This dissertation would not have been possible without the support from my mentors, friends and parents.

First of all, I would like to thank my advisors Dr. James Bowsher and Dr. Fang-Fang Yin for guiding me through my Ph.D. study at Duke University. Dr. Bowsher has been a very supportive, considerate and knowledgeable advisor. He not only shared his insights of SPECT with me, but also guided me on my professional development, for example writing scientific papers, preparing presentations and most importantly, the positive attitudes in research. I also appreciate his help and support on our "Marathon" experiments in the lab. I would like to thank Dr. Yin for his patience, encouragement and insightful criticisms of my work which helped me conquer the difficulties I had during my study at Duke. Dr. Yin has always been willing to share his expertise in medical physics and exhibiting his enthusiasm in the field. I have learnt the importance of leadership and teamwork from Dr. Yin which are beneficial to my career as a medical physicist. I would like to thank Dr. Yoo, Dr. Blitzblau and Dr. Colsher for being my dissertation committee members.

Special thanks go to KUKA Robotics Corporation and Digirad Company for the technical support of the robot and detector. For many times, I was frustrated with the robot and I called KUKA's 24/7 technical support line – the technicians were so patient

xxxi

1. Introduction

1.1 General Introduction

This dissertation investigates the design, imaging feasibilities and hardware implementation of a novel on-board robotic multi-pinhole SPECT system for region-of-interest (ROI) imaging.

On-board imaging is essential for target localization when the patient is on the radiation treatment table. The on-board imaging system is aligned with planning CT or digitally reconstructed radiography (DRR) to record and correct the patient positioning discrepancies. Current on-board imaging, such as CBCT and kV/MV imaging, generally provides anatomical information. However, the lack of tumor and soft tissue contrast for certain types of tumor requires registration with other imaging methods that provide better target delineation. SPECT is a nuclear medicine imaging technique that can provide better tumor to background contrast. In addition, multidimensional radiotherapy that incorporates biological information of the tumor has been increasingly used to enhance the dose distribution[1]. Dose escalation, personalized radiation therapy and adaptive therapy can be achieved by integrating functional imaging which is a complement to anatomical imaging. This biological information can be obtained from functional and molecular imaging modalities such as SPECT.

We propose an on-board SPECT imaging system to provide the functional and molecular imaging information in addition to current on-board imaging modalities.

1

However, there are challenges to implement SPECT with LINAC. One major

consideration is the geometric feasibility of the integration. The on-board SPECT system

needs to acquire images while the patient is on the treatment table. After imaging, the

system needs to make way to allow space for radiation treatment. Therefore, a robotic

arm is proposed here to maneuver the detector about the patient with great flexibility.

Another challenge is that the imaging time of the conventional SPECT takes 20 minutes

or more, which is impractical for imaging patients on the treatment couch before the

radiotherapy. A multi-pinhole collimator is proposed here to increase the imaging

sensitivity and to reduce the imaging time to as short as 4 minutes.

More specifically, this dissertation investigates the design of a 49-pinhole

collimator through computer-aided design (CAD) software, the geometric feasibility of

robotic SPECT in radiation therapy treatment rooms, the alignment of robotic SPECT to

LINAC coordinates, the imaging capability of multi-pinhole SPECT through computer-

simulation and the actual hardware implementation of a robotic SPECT system. Our

results demonstrate that the 49-pinhole SPECT can image lesions in 4 minutes scan time

and provides better tumor contrast recovery in comparison to parallel-hole SPECT. The

robotic SPECT system coordinate frame can be aligned to that of a LINAC to a precision

within 3 mm and 1 degree. The novel robotic SPECT system achieves the required

imaging trajectories around a radiation therapy flat-top table and provides excellent

image quality.

1.2 Overview of Chapters

The rest of this dissertation is organized as follows:

Chapter 2: *Background* provides an overview of radiation therapy and current on-board imaging modalities. The Single Photon Emission Computed Tomography (SPECT) technique is introduced with the focus on reviewing multi-pinhole SPECT systems that have been developed prior to this work. This chapter concludes with the motivation for developing the on-board robotic multi-pinhole SPECT system.

Chapter 3: *Computer-Aided Design (CAD) Studies for On-board Robotic SPECT System* were performed to design the multi-pinhole SPECT system, to evaluate the shielding of this system and to investigate the operating feasibility of the robotic SPECT in the radiation treatment room.

Chapter 4: *Spect-map Validation* was performed to evaluate the resolution and sensitivity modeling in the in-house code *spect-map*. This validation ensures the image reconstruction accuracy for the imaging studies performed in Chapter 5-8.

Chapter 5: *Line-Source Method for Aligning On-board and other Pinhole SPECT Systems* describes an alignment method that utilizes line sources and one pinhole projection. The alignment of on-board SPECT to the LNAC is essential for target localization and image reconstruction. Furthermore, this alignment method may be important for multi-pinhole SPECT, where relative pinhole alignment may vary during

rotation. This chapter was published in a peer-reviewed journal *Medical Physics*, 40(12), 2013.

Chapter 6: *Breast Imaging with a Robotic Multi-pinhole SPECT System* is a simulation study of breast tumor imaging when the patient is in prone position for treatment. The effects of prone breast position board on imaging sensitivity and resolution were investigated. The reconstructed images from the 49-pinhole system were compared to that from a parallel-hole SPECT system. Findings from the simulation study have been prepared in a manuscript "Prone Breast Imaging for On-Board and Other Applications with a Robotic Multi-pinhole SPECT System: A Simulation Study" and submitted to peer review in *Medical Physics*.

Chapter 7: *Noise Reduction of Respiratory-gated Imaging Using Region-of-interest (ROI) Robotic Multi-Pinhole SPECT System* is a simulation study of lung tumor imaging for radiation therapy. The capability of the ROI imaging system in covering the tumor and its motion in the detector FOV were investigated by simulating different tumor sizes and diaphragm motion ranges. Images reconstructed from the ROI imaging system were compared to those from the broad cross-section imaging system to evaluate the effectiveness of ROI imaging techniques in improving sensitivity and reducing image noise. Findings from this study will soon be submitted for publication in *Physics in Medicine and Biology* with the title "Noise Reduction of Respiratory-gated Imaging Using Region-of-interest (ROI) Robotic Multi-Pinhole SPECT System".

Chapter 8: *Hardware Robotic SPECT System* describes the design and development of the robotic SPECT lab. The installation and operation of the detector are described. The connection of the detector to the robotic arm and the procedures of operating the robot are explained in detail. The robotic single pinhole and parallel-hole SPECT detectors demonstrate their capabilities to image a thorax phantom on a radiation therapy flat-top couch for potential on-board functional and molecular imaging in radiation therapy. Findings have been prepared in a manuscript "A Hardware Investigation of Robotic SPECT for Onboard and Other Functional and Molecular Imaging Applications" and submitted to peer review in *Medical Physics*.

2. Background

2.1 Radiation Therapy and On-board Imaging

Radiation therapy is an important clinical process to treat malignant or benign tumors with curative or palliative goal. The rational of radiation therapy is to maximize local control of tumor and to minimize normal tissue complication. To achieve this goal, different target volumes[2, 3] are defined. The gross tumor volume (GTV) generally consists of primary tumor and metastases. The GTV is extended to clinical target volume (CTV) to account for the microscopic extension of disease. To account for motion effects on tumor, an internal margin (IM) is added to the CTV to define the internal target volume (ITV). The planning target volume (PTV) is then defined as the ITV plus the set-up margin (SM).

Besides these volumes, biological target volume (BTV) has been proposed to complement the anatomical information obtained from planning CT, thereby improving target delineation and dose delivery[1, 4]. Imaging techniques, such as Positron Emission Tomography (PET) and Single Photon Emission Computed Tomography (SPECT), are used to provide biological information about tumors, such as metabolism and hypoxia[5]. With these imaging techniques, the primary tumor region could be defined more accurately, therefore maximizing the local tumor control and minimizing the normal tissue complication. Moreover, dose could be modulated, for example delivering higher dose to hypoxic regions or additional dose can be selectively delivered to cell

6

proliferation regions. These specific dose deliveries enable personalized radiation

therapy. In addition, biological function of the tumor can be used to monitor the

response to radiation therapy during treatment, therefore enabling adaptive therapy,

such as dose escalation[6-8].

Radiation therapy techniques have been developed over decades, among which

intensity modulated radiation therapy (IMRT) has greatly improved three-dimensional

conformal radiotherapy (3D-CRT). The major advantage of IMRT is to deliver more

conformal high dose to the target volume while minimizing the dose to the organs-at-

risk (OARs). The challenge in precisely delivering the planning radiation beam is that

this relies on accurate target localization.

Image-guided radiation therapy (IGRT) therefore has been developed to improve

the accuracy and precision of radiation treatment. Imaging is involved in every step of

radiation treatment including diagnosis of tumor, immobilization, tumor localization,

treatment planning, patient positioning, treatment verification, beam delivery and

quality assurance[9]. Among these steps, on-board imaging is one of the major

components of IGRT focusing on verifying patient setup and target localization while

the patient is on the treatment table. Current on-board imaging techniques are generally

cone-beam CT (CBCT) and kV/MV 2D imaging which are essential in many radiation

therapy procedures, such as IMRT and stereotactic body radiation therapy (SBRT).

These imaging tools enable high doses to be delivered precisely to the target with less

injury of surrounding normal tissues. These imaging techniques provide predominantly anatomic information for treatment planning and target localization[10].

2.2 Single Photon Emission Computed Tomography

2.2.1 Overview

SPECT is one of the nuclear medicine imaging modalities, which detects a single photon emitted from radionuclides. Gamma cameras are generally used as the detectors for SPECT. The major components of gamma cameras include the collimator, the scintillation crystal and the photo multiplier tubes. Among these components, collimators are closely related to this research project. There are four different basic collimators: parallel-hole, diverging, converging and single pinhole.

Parallel-hole collimators are used widely in diagnostic imaging. The common systems are single-head SPECT and dual-head SPECT. The imaging trajectory of the parallel-hole collimated detector is generally 180 degrees for most cardiac applications or 360 degrees for non-cardiac imaging.

A diverging collimator has holes that diverge from the detector surface. With a diverging collimator, objects projected onto the detector are minified. A converging collimator has holes that converge from the detector. With a converging collimator, objects projected onto the detector are magnified.

The pinhole collimator is a special case of a converging collimator. The pinhole collimator consists of a small aperture generally made of tungsten, placed at the tip of a lead cone. The pinhole focal length is the distance from pinhole to the detector surface. The projected object is magnified if the distance from the object to the pinhole is less than the focal length. The object is minified vice versa. The imaging requirement for acquiring all line integrals in the central plane is 180 degrees plus the full pinhole opening angle.

Resolution and sensitivity have always been challenging for SPECT. Resolution depends on the intrinsic resolution of the SPECT detector and the extrinsic resolution which degrades as the distance between the detector and the object increases. The system sensitivity depends on the type and the number of the collimators. The detailed calculation of resolution and sensitivity is shown in Chapter 4.

2.2.2 Multi-pinhole SPECT system

Multi-pinhole SPECT systems have been investigated as early as 1978 when Vogel *et. al.* developed a seven-pinhole collimator which was used for myocardial Tl-201 perfusion imaging[11]. This system showed improved detection sensitivity in comparison with a parallel-hole SPECT system. Subsequently, this seven-pinhole system has been used to perform studies on different anatomical sites: dynamic cardiac imaging of the multigated blood-pool[12], brain and thyroid imaging[13], and cisternography[14]. To reduce

the degradation of resolution and sensitivity, 12 pinholes were later proposed instead of 7 pinholes[15]. To further improve the resolution of the multi-pinhole system, the imaging geometry has been optimized. Three, four, five and seven-pinhole collimators and different angular positions of the multi-pinhole system have been studied[16]. A 9-pinhole collimator was designed and constructed for cardiac imaging[17]. This 9-pinhole system has been demonstrated to have detection efficiency 5 times that of the conventional parallel-hole system for the same resolution. In addition, an 81-pinhole SPECT detector was designed and computer simulated to enable stationary cardiac imaging with 8 of the 81-pinhole detectors[18]. This system provided four times higher sensitivity than conventional dual-detector cardiac imaging. Furthermore, a 20-pinhole detector was designed and constructed for 10-minute rest/stress myocardial perfusion imaging[19]. Recently, Discovery NM 530c[20], a cardiac SPECT system, was developed by GE Healthcare (Waukesha, WI). This system utilized CZT detectors and had 19-pinholes. In addition to the systems discussed above, multi-pinhole SPECT systems have also been widely designed used for small animal studies[21-23]. Besides the multi-pinhole ROI SPECT systems, cone beam SPECT has also been developed as another ROI imaging system[24-26].

In this dissertation, a 49-pinhole collimator was proposed to provide SPECT imaging times of 4 minutes[27] which is suitable for on-board imaging applications with the patient on the treatment table. The sensitivity of the 49-pinhole SPECT system is much higher than conventional commercially available parallel-hole SPECT systems.

The detailed comparison is shown in Chapter 4 Section 4.3. This 49-pinhole collimator

has 7 detector pods with 7 pinholes each. All 49 pinholes focus on the same target region

which is an 8.24 cm-diameter sphere that encompasses the lesions for imaging, therefore

enabling region-of-interest (ROI) imaging. The detailed design and configuration of the

49-pinhole collimator geometry are shown in Chapter 3 Section 3.3.

2.2.3 On-board Robotic Multi-pinhole SPECT

Studies have shown that radiation therapy based on functional and molecular

information about the tumor and surrounding tissue has the potential to enhance the

effectiveness of radiation therapy[1, 28, 29]. The biological information obtained from

functional and molecular imaging techniques can be integrated into current

radiotherapy in different stages. This information can be used for pre-treatment

diagnosis and then registered with planning CT for treatment planning. Target regions

can be improved by knowing the hypoxic cells in the tumor region[30]. Dose painting and

dose escalation have been used in the biological region, such as for hypoxia and cell

proliferation, to improve dose delivery effectiveness and tumor control[1, 31, 32]. Tumor cell

radioresistance can be monitored after several treatment fractions, thereby enabling

adaptive radiation therapy[33, 34].

PET and SPECT play an important role in providing biological information about

the tumor and have been utilized for tumor staging and treatment planning in

combination of Computed Tomography (CT)[35-37]. MRI has also been actively used to assistant with treatment planning and post-treatment assessment[38]. However, these modalities have not been used for on-board functional imaging applications. Currently, on-board PET and on-board MRI are under development[39-41].

As discussed in Section 2.1, current on-board imaging systems are limited in their functional and molecular imaging capability. SPECT is a candidate to achieve on-board functional and molecular imaging. However, traditional SPECT systems have limitations that must be overcome before SPECT can be integrated into the LINAC treatment room: the traditional SPECT imaging system takes 20 minutes or more for one scan, which is long for on-board imaging applications; the gantry mounted detector configuration is hard to integrate with a LINAC; and the resolution and sensitivity of SPECT systems are limited.

Hence, the aim of this dissertation is to develop an on-board functional and molecular SPECT imaging system. Several criteria were considered and investigated for system development: (a) convenient integration of the on-board imager with the LINAC, (b) short imaging time, (c) better resolution and sensitivity tradeoffs, (d) non-circular imaging trajectories feasible for radiation therapy flat-top couches and (e) imaging versatility. To achieve integration with LINACs, a robotic arm is proposed to maneuver the SPECT detector in the radiation treatment room[42-44]. The robotic arm provides flexibility to achieve non-circular imaging trajectories of the SPECT detector tracing the

flat-top radiation treatment table while minimizing the distance between the detector

and target and avoiding collision, as shown in Chapter 8. The robotic arm can be

retracted after SPECT imaging which allows fully normal LINAC gantry motion for

treatment.

3. Computer-Aided Design (CAD) studies for On-board Robotic SPECT Systems

3.1 Introduction

Computer-aided design (CAD) studies were performed to broadly assess the feasibility of on-board robotic multi-pinhole SPECT. The design of the multi-pinhole collimated SPECT detector, detector shielding, detector and robotic arm attachment, robotic SPECT placement in radiation therapy treatment room, and robot/detector trajectories about the patient, treatment table and gantry were investigated.

3.2 Vender CAD drawing of SPECT detector and robotic arm

Digirad (DIGIRAD Corp., Poway, CA) provided realistic CAD models of their compact Digirad gamma detector (Figure 1 (a)), parallel-hole collimator (Figure 1(b)) and single pinhole collimator (Figure 1(c)).

Kuka (KUKA Robotics Corporation, Shelby Township, MI) provided CAD drawings of the robotic arm and the robot mounting rail for this study, shown in Figure 2 and Figure 3 respectively. A KUKA KR 150-L110 robot was used with the payload capacity of 110 kg at full speed (2 m/s) and an arm length of 1500 mm, Figure 2. The robot itself has a weight of 1263 kg. The rail used to mount the robot can be positioned on the floor or on the ceiling.
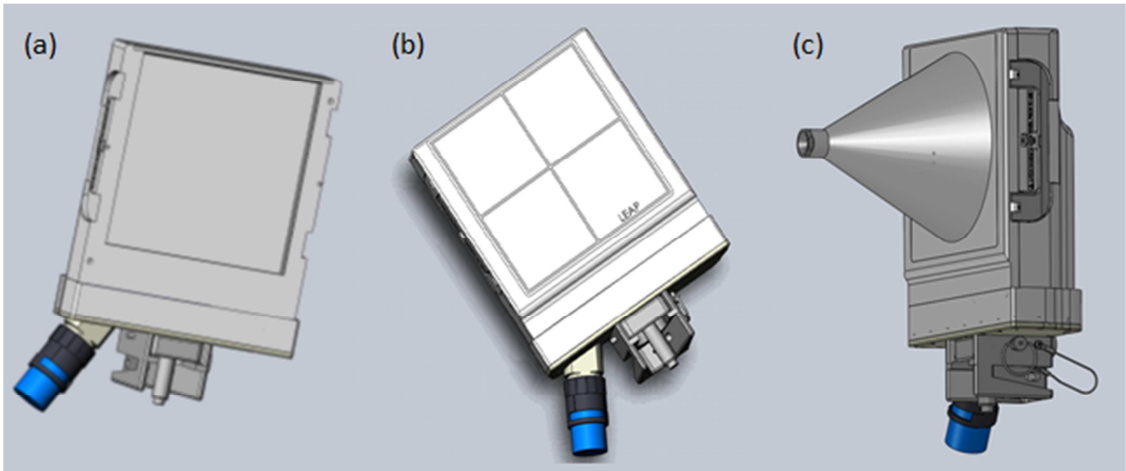
Figure 1: (a) Digirad SPECT detector without collimator. (b) Digirad low energy all-purpose parallel-hole collimated SPECT detector. (c) Digirad pinhole collimated SPECT detector.
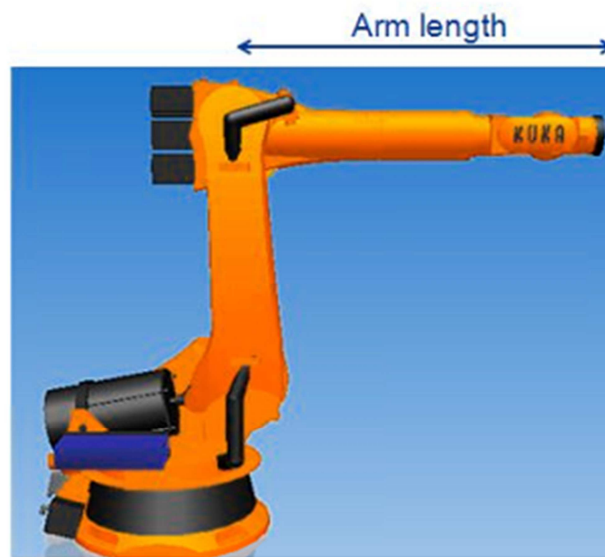
Figure 2: KUKA KR 150-L110 robotic arm with arm length of 1500 mm, and weight of 1263 kg. The payload is 110 kg at full speed of 2 m/s.

Figure 3: Rail for mounting the robotic arm.

3.3 CAD studies of 7x7 pinholes vs. 9x9 pinholes design

The CAD package SolidWorks (SolidWorks Corp. Concord, MA) was used to investigate and design the multi-pinhole SPECT system.

A key design criterion for the multi-pinhole system was that every pinhole focuses on the same target region[43].

A 9-pinhole SPECT[43] was proposed and further investigated using CAD software, as shown in Figure 4. Nine detectors and their associated pinhole collimators were arranged in a 3x3 pattern. Figure 4(a) shows five of the nine detectors. Figure 4(b-c) shows all 9 detectors. The corner detectors collide with the side detectors when they were tilted to fully cover the ROI, as shown in Figure 4(b) and (c). To avoid collision, the four detectors at the corner were shifted and tilted, as shown in Figure 5.
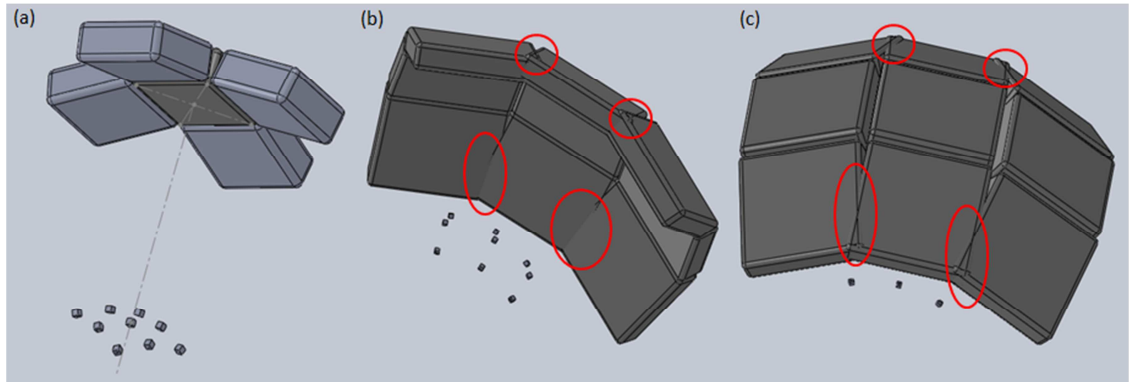
Figure 4: 9-pinhole system: 9 detectors with one pinhole each in a 3x3 pattern. (a) Nine pinholes and five of nine detectors. The pinholes were arranged to cover the same target region and the detectors are tilted to have the same pinhole focal length. (b) and (c) Different views of nine detectors. The red circle shows the collision of the corner detectors with the side detectors.
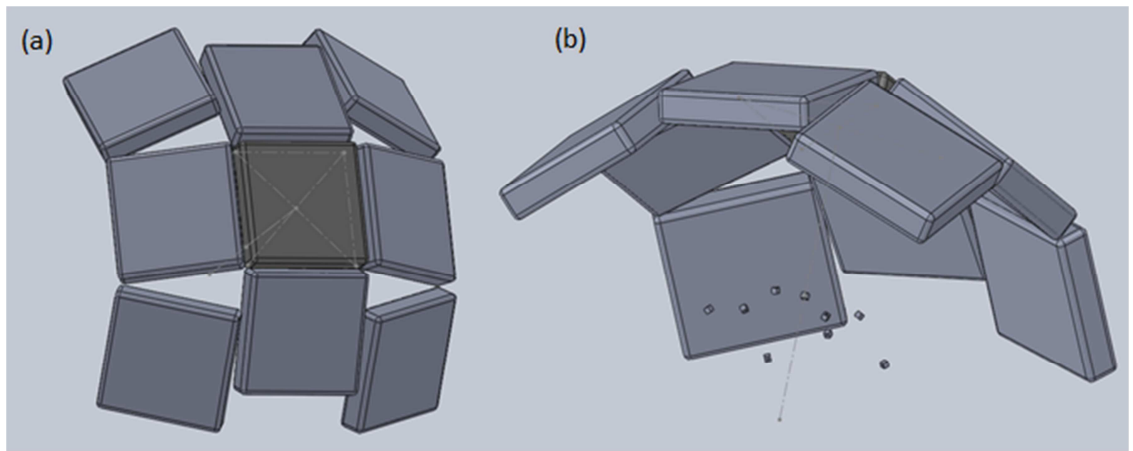
Figure 5: (a) and (b) 9-pinhole system. The four corner detectors were tilted to avoid collision with four side detectors.

To further improve image sensitivity, an 81-pinhole SPECT system was designed

and investigated based on the 9-pinhole system introduced in the previous paragraph.

This 81-pinhole system consisted of 9 of the previously discussed 9-pinhole collimated detectors, as shown in Figure 6. Each one of the detectors has an area of 21x21 cm^2. However, this design is not practical because the 81-pinholes configuration folds to such an extent that the target region is within the convex hull of the detector system, which is not suitable for patient imaging.
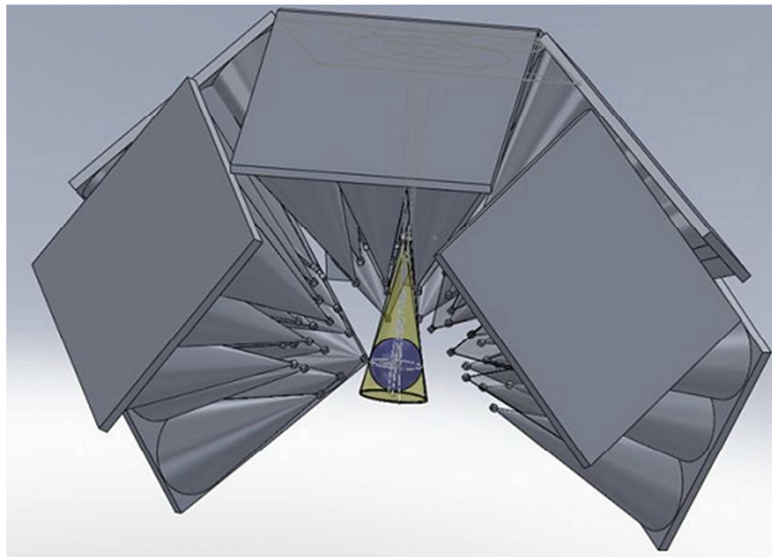
Figure 6: 81-pinhole system. Note here, each 9-pinhole system has been simplified to one big detector of 21 cm side length instead of 9 individual detectors as shown in Figure 5. The blue sphere is the ROI.

A 49-pinhole system was then designed as illustrated in Figure 7. This 49-pinhole system involves a central detector and 6 peripheral detectors with 7 pinholes per detector. Each pinhole is tilted such that all pinholes focus on the same imaging target region, shown by the red sphere. The gray and yellow cones in the figure illustrate the

hypothetical imaging rays of the pinhole collimator. The CAD simulation illustrates that

the ROI can be well outside of the convex hull of the 49-pinhole system. Figure 8 shows

a computer simulation of the 49-pinhole system[27]. A red circle shows each detector pod.

Within each pod, there are 7 individual detectors and their corresponding pinhole

collimators. Each detector corresponds to one pinhole.
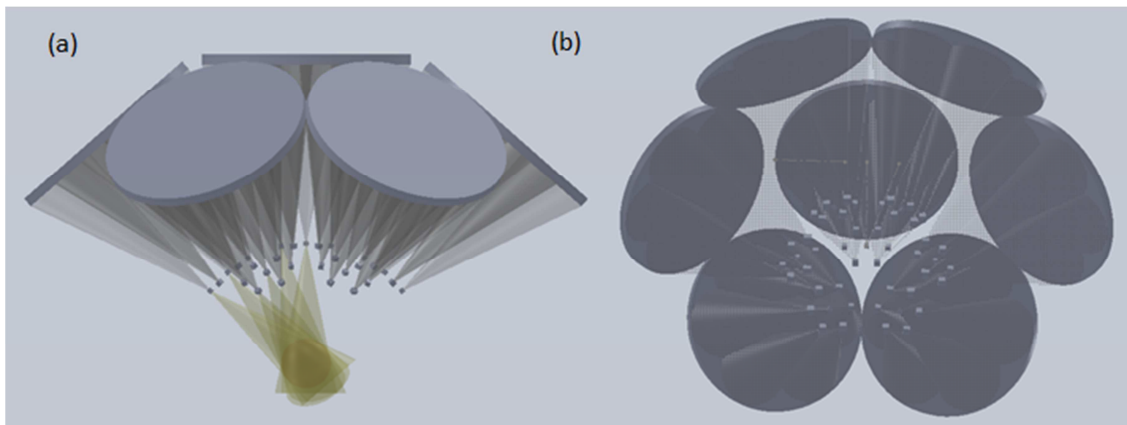
Figure 7: CAD model of a 49-pinhole SPECT design. Seven detector pods with a central detector pod and six peripheral pods. Each pod has seven pinholes, with one central pinhole and six peripheral pinholes. The red sphere in (a) is the imaging ROI.
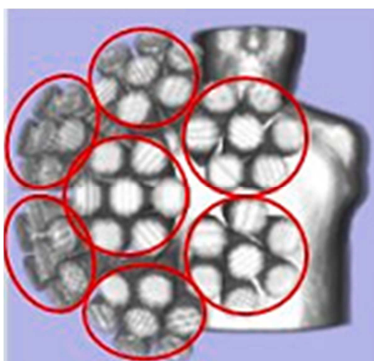
Figure 8: 49-pinhole SPECT system in spect-map computer simulation. There are 7 pods as indicated by the red large circles -- one center pod and six peripheral pods. Each pod has seven individual detectors with one pinhole each.

This 49-pinhole system can be attached to the robot with a robot-detector end effector, as suggested schematically in Figure 9(a). The angle between the peripheral pods and the central pod can be adjusted at different imaging positions to keep the entire ROI in the field of view (FOV) of all detectors while minimizing the distance between the detector system and the imaging target region[42], e.g. suggested schematically by the flexible joint in Figure 9(a).
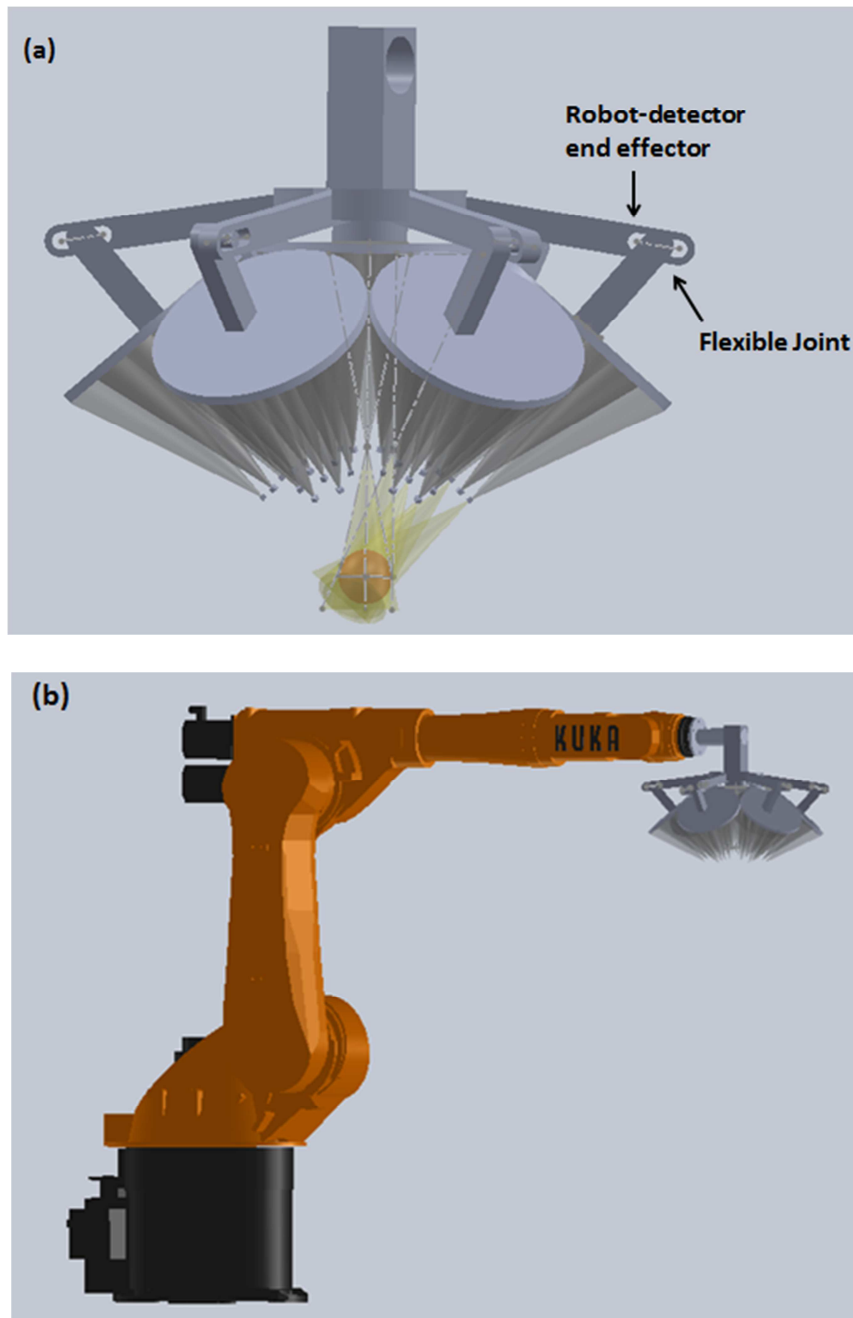
Figure 9: (a) The robot-detector end effector and the 49-pinhole system. The flexible joint can be rotated to adjust the angle between the peripheral pods and the central pod. (b) The 49-pinhole system attached to the Kuka robotic arm (KR 150-L110).

3.4 Shielding feasibility

Lead is generally used for Tc-99m (140keV) shielding. The density of lead (ρ) is 11.35 g/cm³ and the mass attenuation coefficient (μ/ρ) at 140 keV in lead is 2.721 cm²/g[45]. The linear attenuation coefficient (μ)

$$\mu = \frac{\mu}{\rho} \times \rho = 2.721 \frac{cm^2}{g} \times 11.35 \frac{g}{cm^3} = 30.86 \; cm^{-1} \tag{1}$$

The half value layer is calculated

$$HVL = \frac{\ln 2}{\mu} = \frac{\ln 2}{30.86 \; cm^{-1}} = 0.022 \; cm = 0.22 \; mm \tag{2}$$

The lead shielding thickness for Tc-99m can range from 3 mm up to 12 mm. The lead shielding designed for the 49-pinhole system is shown in Figure 10 and Figure 11. The weight of the Digirad 2020tc detector without collimator is 13 kg[46]. This weight was used to estimate the total weight of each pod in the 49-pinhole system. The total estimated detector weight for all 7 pods is 91 kg. Table 1 shows the weight of the lead shielding. The total estimated weight of the 49-pinhole system is from 114 kg to 189 kg. This is a ballpark estimate for the shielding weight.
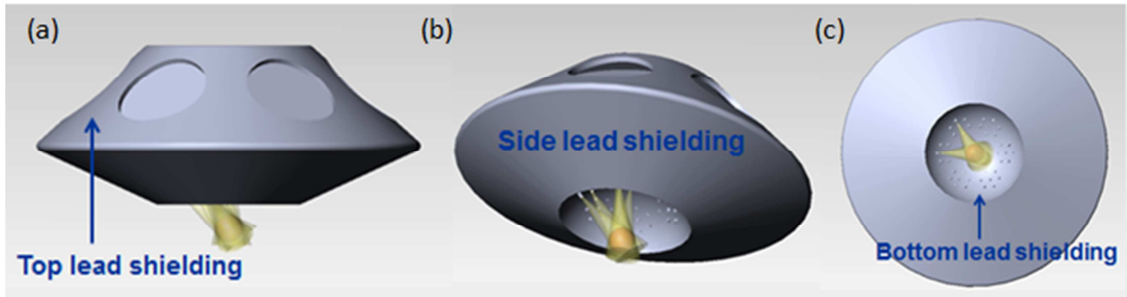
Figure 10: Lead shielding design for the 49-pinhole SPECT system. (a) Top (b) side and (c) bottom part of the lead shielding.
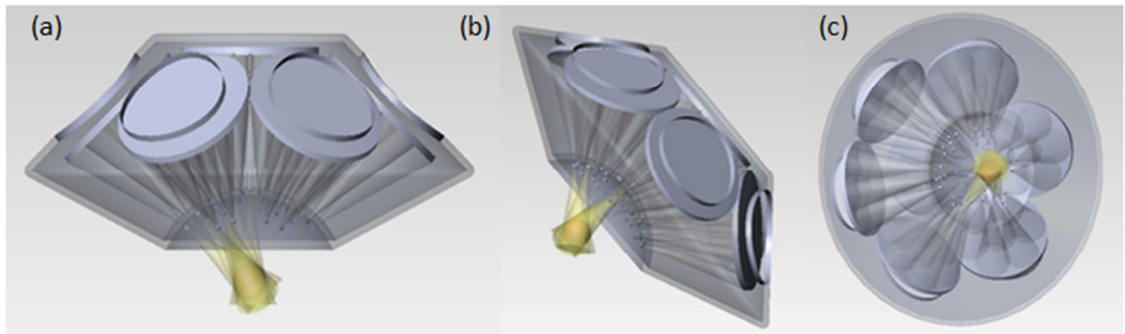
Figure 11: Transparent view of lead shielding for the 49-pinhole SPECT system.

Table 1: Weight of the lead shielding designed for 49-pinhole SPECT system.

Lead shielding thickness	Seven Digirad 2020tc detectors weight (kg)	Lead shielding weight (kg)			Total system weight (kg)
		Top	Side	Bottom	
3 mm	91	9.87	11.43	2.34	114.64
6 mm	91	19.74	22.87	4.68	138.29
9 mm	91	29.61	34.30	7.02	161.93
12 mm	91	39.48	45.74	9.36	185.58

3.5 Detector Attachment to Robotic Arm

For the parallel-hole collimated detector, two joints were investigated to attach

the detector to the robotic arm in either the parallel or the perpendicular orientation, as

shown in Figure 12.
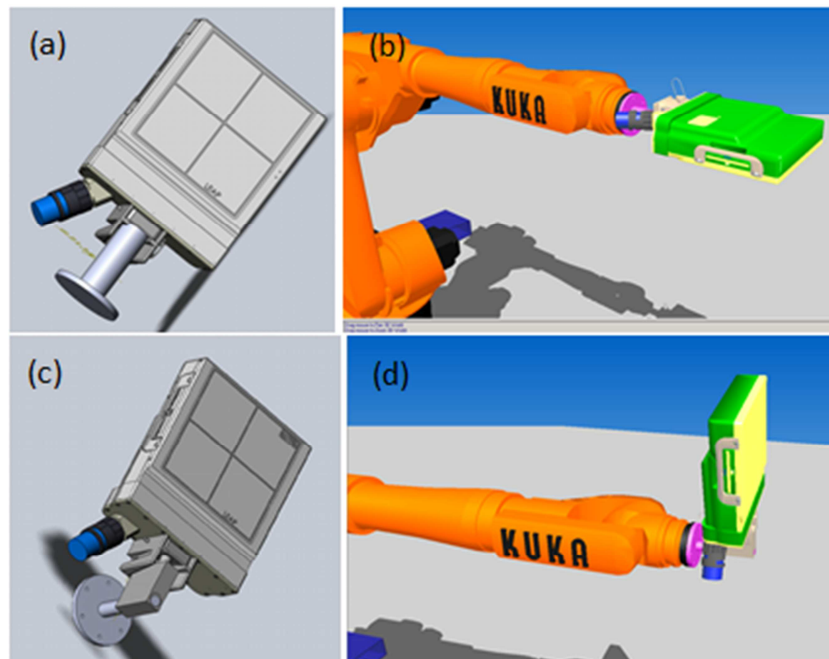
Figure 12: (a) Parallel-hole detector with a parallel joint. (b) Parallel-hole detector attached to the robotic arm with the parallel joint. (c) Parallel-hole detector with a perpendicular joint. (d) Parallel-hole detector attached to the robotic arm with the perpendicular joint.

3.6 CAD studies of robotic SPECT in the radiation therapy treatment room

Different robot configurations, including mounting the robot on ceiling or floor

and positioning the robot on a rail or bolted in place, were investigated to determine the

geometric feasibility of robotic SPECT for patients in position for radiation therapy. Imaging trajectories were investigated for different collimators of parallel-hole, single pinhole and multi-pinhole, and for different anatomical sites of brain and thorax.

3.6.1 Rail on Ceiling

To minimize the occupancy of the LINAC treatment room, the robotic arm was attached to the rail and positioned on the ceiling. The imaging trajectories about the patient thorax are shown in Figure 13. The robot used in the simulation was a KR 60 model which has a maximum payload of 60 kg that is sufficient for the Digirad 2020tc parallel-hole and single pinhole detector. Based on the shielding calculation in Table 1, a larger robot would be required for the 49-pinhole system. The robot model KR 150-L110 was considered, however, this robot cannot be mounted on the ceiling.
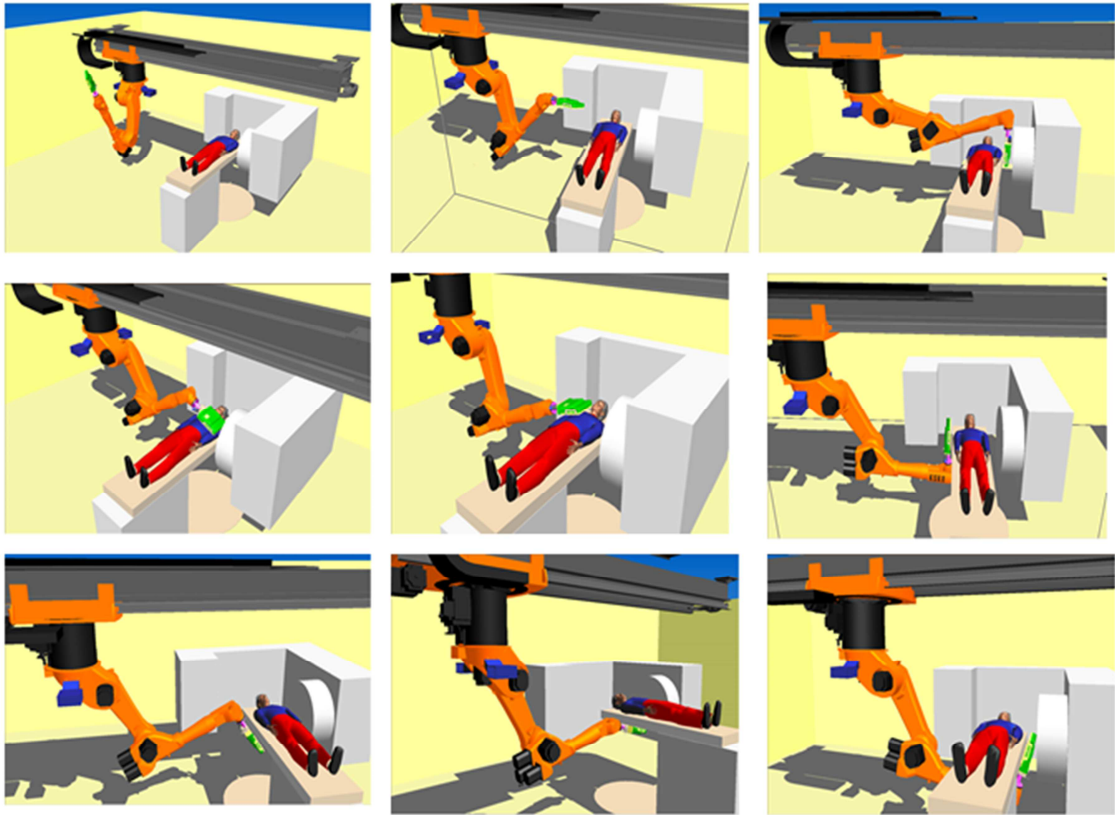
Figure 13: Robotic arm (KR 60) attached to the rail and positioned on the ceiling with a parallel-hole detector. The imaging trajectories of the patient thorax region are shown in sequence from left to right. The LINAC gantry is rotated 90 degrees to provide space for robotic SPECT imaging.

3.6.2 Rail on Floor

The KR 150 L110 robot was attached to the rail and positioned on the floor. The

rail was perpendicular to the treatment couch which is at 0 degree. The robotic arm with

parallel-hole detector attached in parallel to the arm was sufficiently flexible to enable

almost a 360 degree imaging trajectory of the thorax region, as shown in Figure 14. The

LINAC gantry is rotated 90 degree.
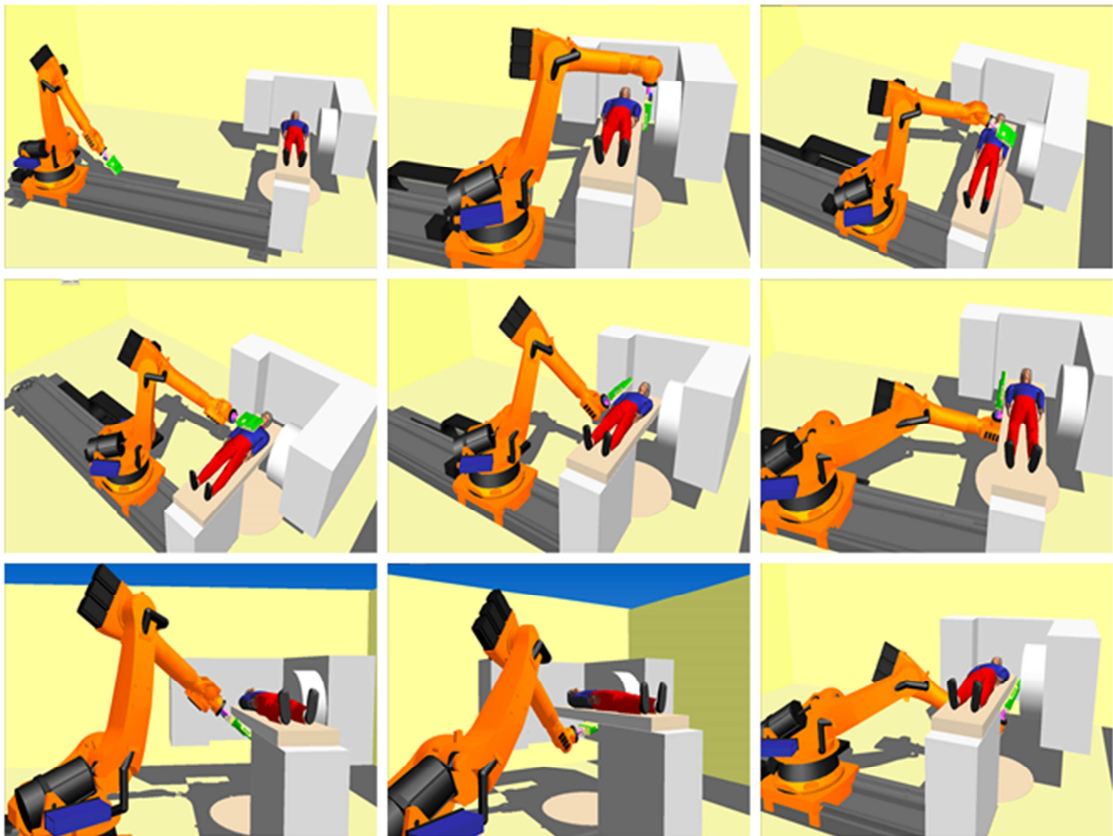
Figure 14: Robotic arm (KR 150-L110) attached to a rail and positioned on the floor with a parallel-hole detector attached parallel to the robotic arm, imaging the patient thorax region. Also shown are a patient table and the LINAC. The LINAC gantry is rotated 90 degrees to provide space for robotic SPECT imaging.

Figure 15 shows a parallel-hole detector attached to the robotic arm in the

parallel orientation to image the patient head. The robotic arm configuration could

provide non-traditional imaging trajectories of the patient head.
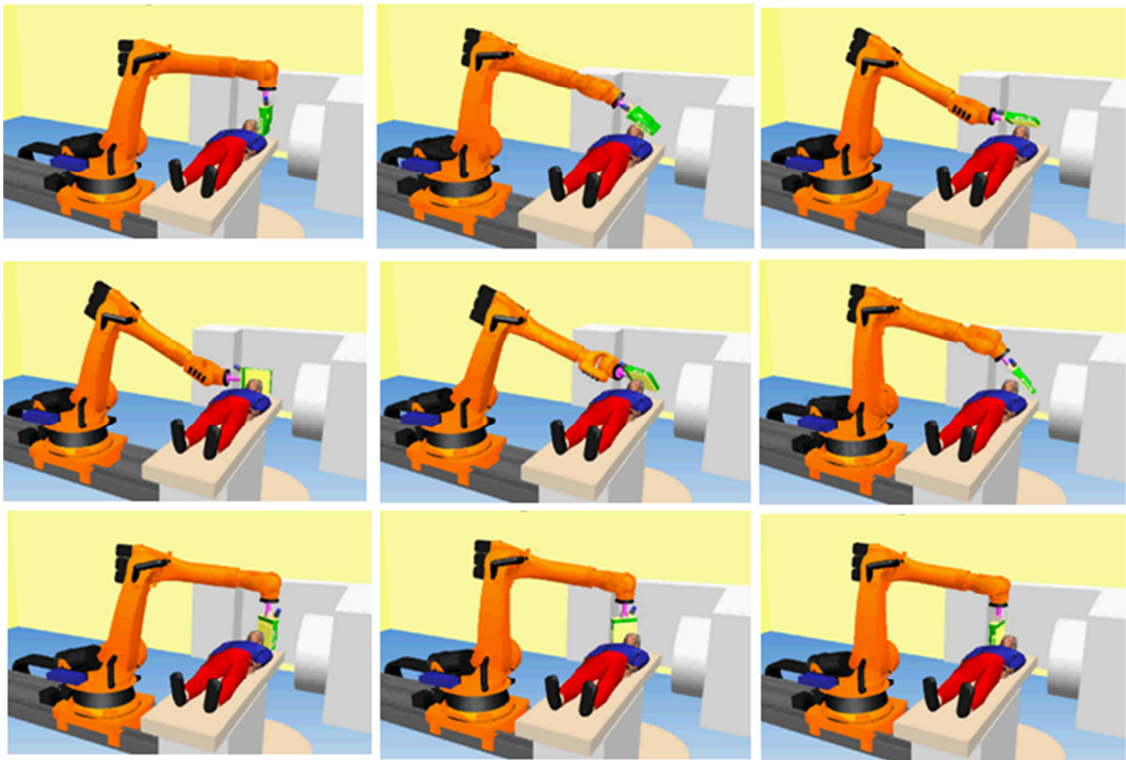
Figure 15: Robotic arm (KR 150-L110) attached to the rail and positioned on the floor with parallel-hole detector attached parallel to the robotic arm, imaging the patient head. Also shown are a patient table and the LINAC. The LINAC gantry is rotated 90 degrees to provide space for robotic SPECT imaging.

When the parallel-hole detector was attached to the robotic arm in a perpendicular orientation, it has limited access to the left side of the patient because the robotic arm would collide with the LINAC gantry, as shown in Figure 16.
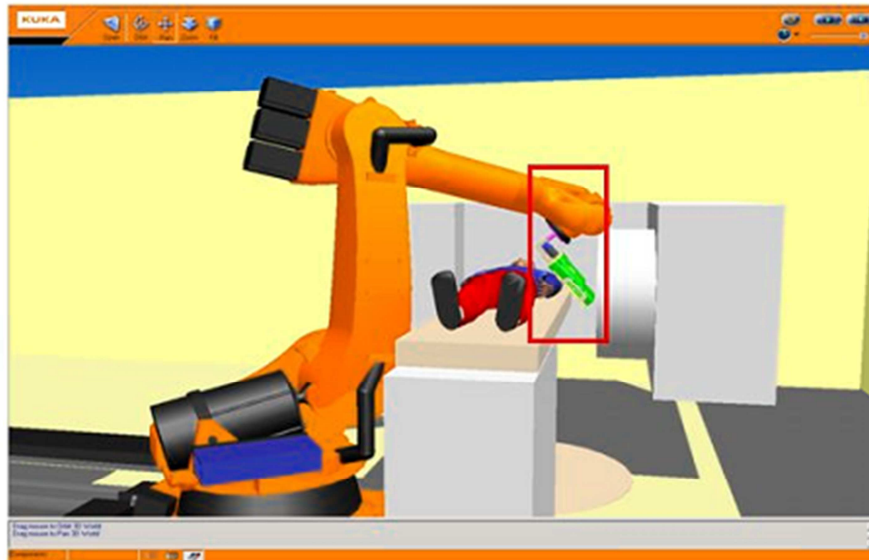
Figure 16: Robotic arm (KR 150-L110) attached to the rail and positioned on the floor with parallel-hole detector attached perpendicular to the robotic arm. The detector has limited access to the patient left as indicated by the red square box because of collision with the LINAC gantry.

Figure 17 shows the robotic arm with single pinhole detector attached parallel to the arm imaging the patient thorax region. The LINAC gantry is rotated 90 degree. With the pinhole collimator, the detector may have limited access to the gantry side of the patient because the pinhole collimator extends out from the detector surface with a typical focal length of 12 cm to 20 cm.
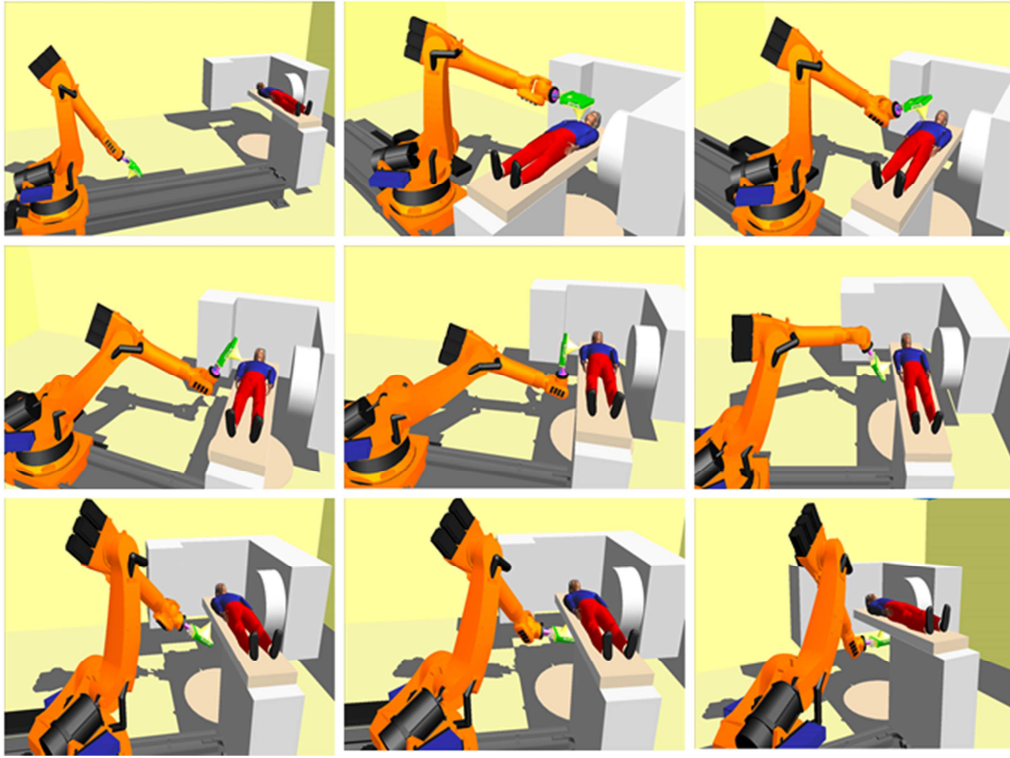
Figure 17: Robotic arm (KR 150-L110) attached to the rail and positioned on the floor with pinhole detector attached parallel to the robotic arm, imaging the patient thorax region. The LINAC gantry is rotated 90 degrees to provide space for robotic SPECT imaging.

Figure 18 and Figure 19 show the multi-pinhole detector attached to the robotic arm positioned on the rail in imaging the patient thorax and brain while the patient is in therapy position.

30
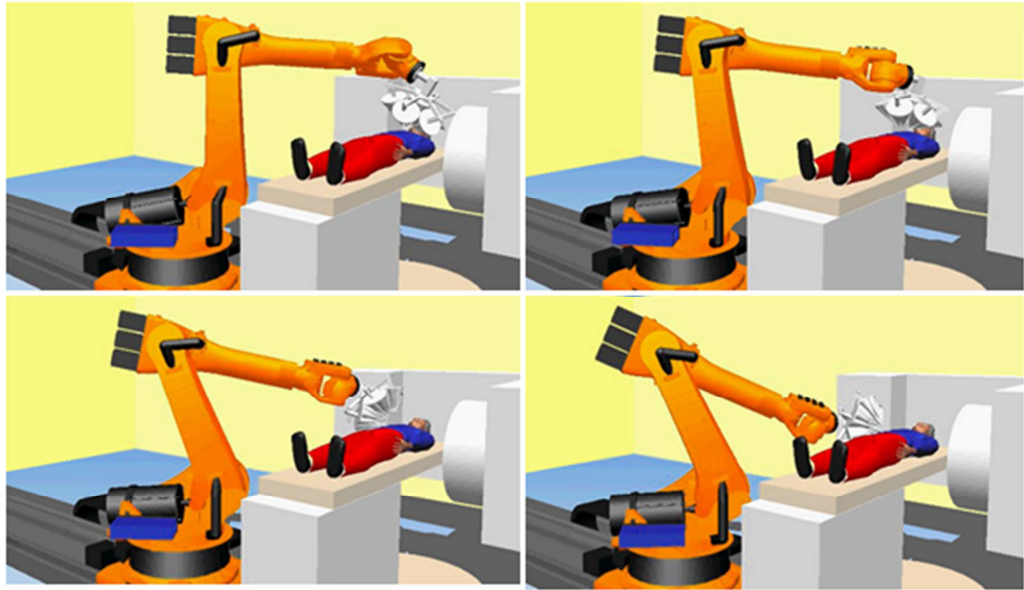
Figure 18: The 49-pinhole detector attached to the robotic arm imaging the patient thorax region. Also shown are a patient table and the LINAC.
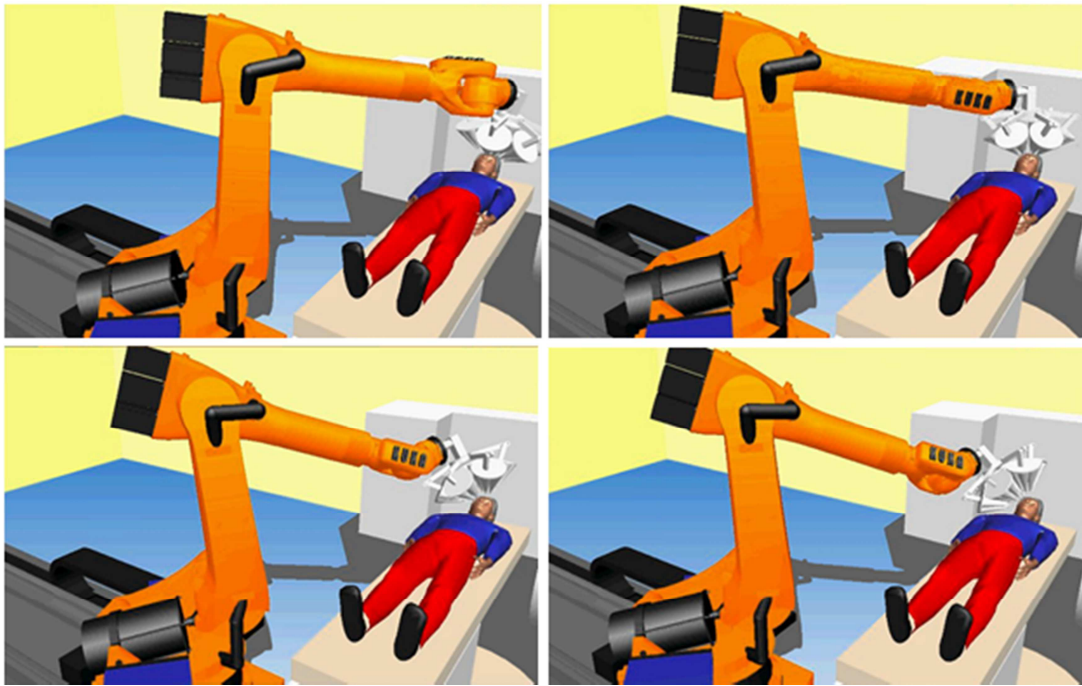
Figure 19: The 49-pinhole detector attached to the robotic arm imaging the brain of patient in position for radiation therapy. Also shown are a patient table and LINAC.

The rail could also be positioned at an angle to the treatment couch, as shown in Figure 20. This configuration could potentially save space for a smaller radiation treatment room.
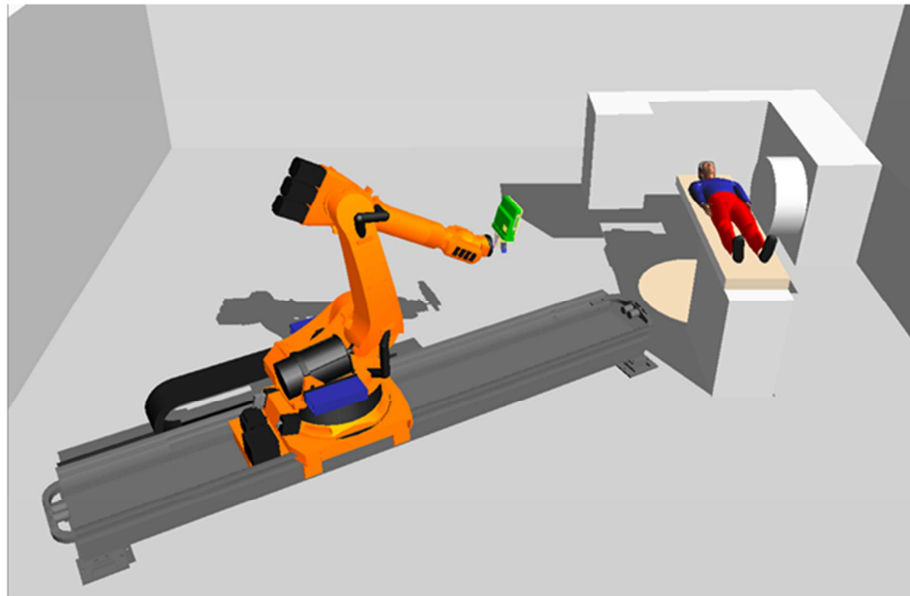
Figure 20: The rail is positioned at an angle to the treatment couch.

3.6.3 Fixed Robotic Arm Base on Floor

We also considered the possibility of having the robotic arm fixed on the floor as

shown in Figure 21. The parallel-hole detector is attached to the robotic arm in a parallel

orientation. In this simulation, the robot barely reached the distal side of the patient.

Therefore, while a 180 degree orbit is achievable, a full 360 degree orbit is not possible.

Different robot positions have been considered, e.g. closer to the LINAC could enable

the imaging on the patient side distal to the robot, however, the robotic arm axes exceed

the mechanical limit to image the proximal patient side. An optimized position could be

determined to provide the maximum imaging range.
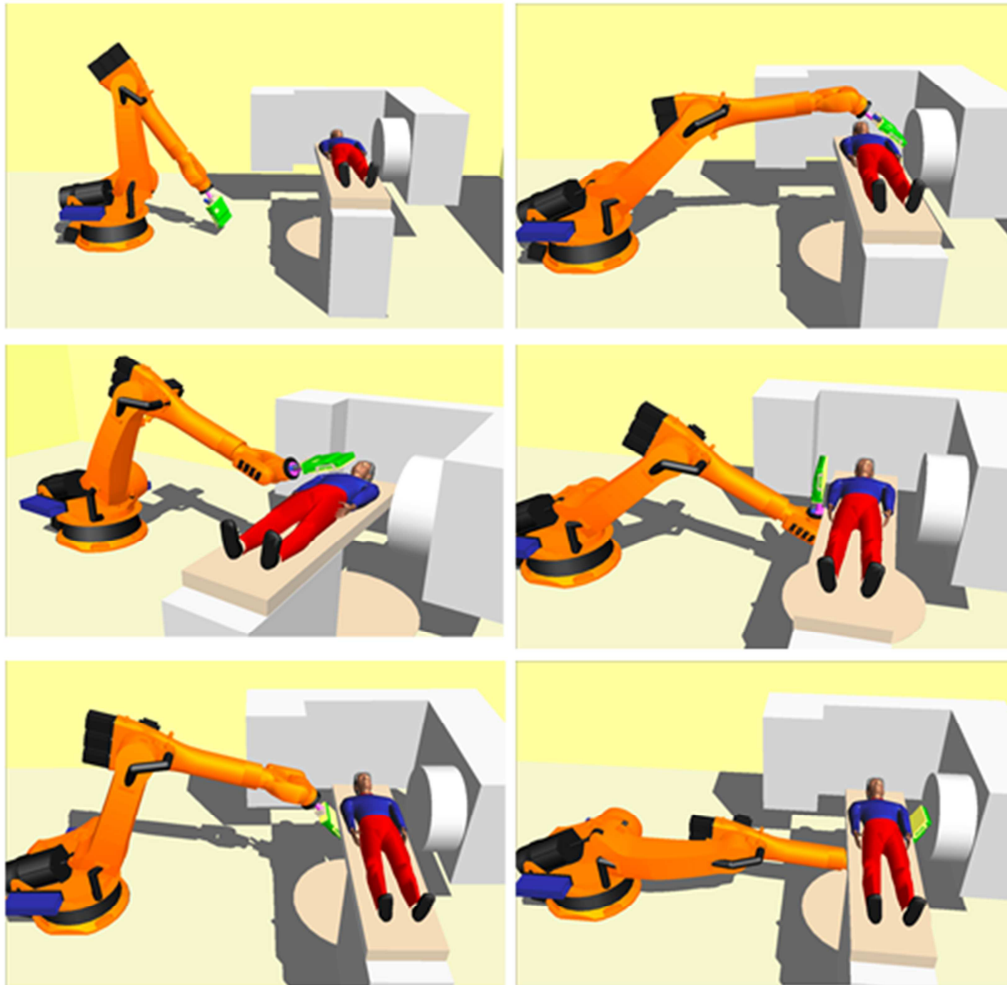
Figure 21: Robotic arm (KR 150-L110) fixed on the floor with parallel-hole detector attached parallel to the robotic arm, imaging the patient thorax region. The robot barely reaches the distal side of the patient. The LINAC gantry is rotated 90 degrees to provide space for robotic SPECT imaging.

3.7 Conclusions

The 49-pinhole SPECT detector was designed with all pinholes focusing on the

same ROI. The peripheral detector pods can be adjusted relative to the central detector

pod. The lead shielding modeled for the multi-pinhole collimation was found to be

34

within the payload capacity of a reasonably sized and priced commercially available robot.

The robotic SPECT system provided flexible and effective imaging trajectories of the patient in position for radiotherapy while avoiding collision. Rail mounted systems enabled a full range of detector positions and orientations to various treatment sites including head and torso, while avoiding collision with LINAC, patient table and patient. Static mounted robot configurations provided good positions and orientations on the proximal side of the patient but have some limitations on the distal side. Parallel hole, pinhole and multi-pinhole collimated systems can be maneuvered with comparable versatilities.

The CAD studies of on-board robotic multi-pinhole system demonstrated the potential to provide real-time functional and molecular information as the patient in position for radiation therapy.

4. SPECT-map Validation

An in-house developed code SPECT-map (By Dr. James Bowsher, Duke University Medical Center) was used in this disseration for simulation imaging studies to generate the SPECT projections and reconstructions of the digital phantom (Chapters 6 and 7). This code was also utilized to reconstruct the actual SPECT images acquired from the robotic SPECT hardware system (Chapter 8). Therefore, the accurate sensitivity and resolution modeling of the code are crucial for correct image reconstruction.

4.1 Sensitivity and Resolution

The parallel-hole collimated detector diagram is shown in Figure 22. The length of the collimator hole is l. The collimator hole diameter is d. The radiao-active object is placed at distance D from the front surface of collimator. The septal thickness of the collimator is t. The sensitivity (S_{par}) and resolution (R_{par}) of the parallel-hole collimated detector are shown in (3) and (4)[47].

$$S_{par} = K^2 \frac{d^2}{\left(l_{eff}\right)^2} \left(\frac{d}{d+t}\right)^2 \tag{3}$$

$$R_{par} = \frac{d(D + l_{eff})}{l_{eff}} \tag{4}$$

where K is a constant for different collimator hole shapes (~ 0.26 for hexagonal holes in a hexagonal array), $l_{eff} = l - \frac{2}{\mu}$ is the effective length of the collimator holes, and μ is the linear attenuation coefficient of the lead collimator.
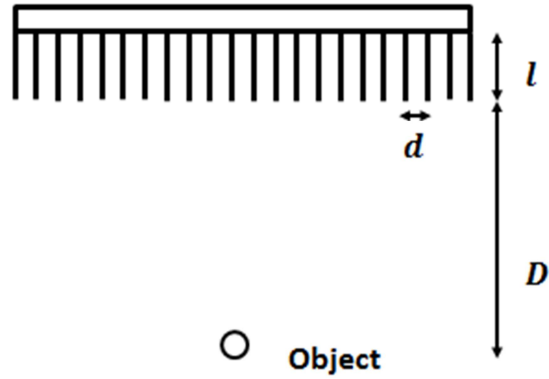
Figure 22: Parallel-hole collimated detector illustration shows collimator hole length *l*, hole diameter *d*, radiao-active object and the distance *D* from the object to the front surface of collimator.

The pinhole collimated detector diagram is shown in Figure 23[48, 49]. The diameter of the pinhole is d. The pinhole openning angle is α. The distance from the photon source to the pinhole is h. The angle between the line segment from the center of the aperture to the photon source and its projection onto the plane of the aperture is θ.

There are two components of the pinhole sentivity: geometric and penetrative. The geometric sensitivity (S_g)

$$S_g = \frac{d^2 \sin^3 \theta}{16h^2} \tag{5}$$

The photons that pass through the pinhole collimator material are considered as penetrative senstivity. The total sensitivity of the pinhole collimator (S_{total}) is the sum of the geometric and penetrative sensitivity[48],

37

$$S_{total} = \frac{d^2 \sin^3 \theta}{16h^2} + \frac{\sin^5 \theta \tan^2 \frac{\alpha}{2}}{8h^2\mu^2} \times (1 - \frac{\cot^2 \theta}{\tan^2 \frac{\alpha}{2}})^{\frac{1}{2}} \times (1 - \frac{\cot^2 \theta}{\tan^2 \frac{\alpha}{2}} + \mu d \csc \theta \cot \frac{\alpha}{2})$$

(6)

The geometric resolution without taking into account the photon penetration with the pinhole collimator is

$$\lambda_g = d(1 + \frac{1}{M})$$

(7)

where $M = \frac{f}{h}$ is the magnification of pinhole collimator and f is focal length of pinhole collimator[49]. To account for the photon penetration, the equivalent diameter (d_e) can be entered in (7)[49]

$$d_e = \sqrt{d \left(d + \frac{2}{\mu} \tan \frac{\alpha}{2} \right) + \frac{2}{\mu^2} \tan^2 \frac{\alpha}{2}}$$

(8)

The system resolution (R_{sys}) is a combination of detector intrinsic resolution R_{int} and the collimator resolution for both parallel-hole and pinhole collimators.

$$R_{sys_{par}} = \sqrt{R_{par}^2 + R_{int}^2}$$

(9)

$$R_{sys_{pin}} = \sqrt{\lambda_g^2 + R_{int}^2}$$

(10)
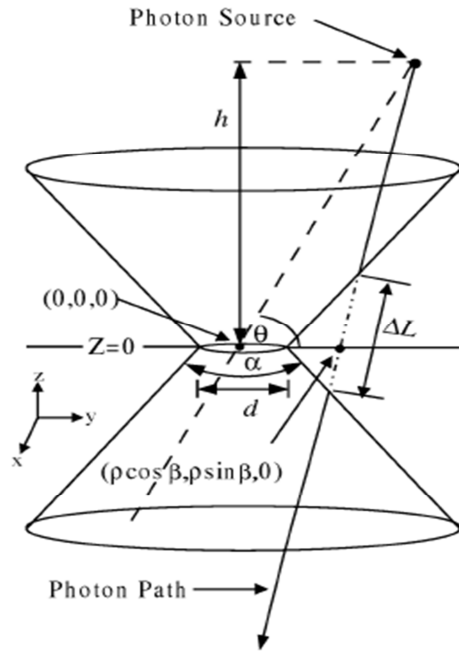
Figure 23: Pinhole collimated detector illustration shows the diameter d of the pinhole collimator, the pinhole openning angle α, the distance from the photon source to the pinhole h, and the angle between the line segment from the center of the aperture to the photon source and its projection onto the plane of the aperture is θ. The figure if from references [48, 49].

4.2 Single Pinhole Collimator Sensitivity Verification of SPECT-Map

A small sphere with activity concentration (A_c) of 3000 μCi/ml and volume (V) of

0.000523 cm³ in the center of the phantom was used as the photon source in this

calculation. The tungsten pinhole collimator was set to be 15 cm distance away from the

photon source ($h = 15\ cm$). The pinhole diameter d was 0.1 cm. The pinhole full opening

angle (α) was 100 degree. The angle θ between the line segment from the center of the

aperture to the photon source and its projection onto the plane of the aperture varied

from 90 degree to 41.76 degree.

The forward projection data of the sphere was generated with the above

parameters for Tc-99m radiotracer and I-131 radiotracer using the in-house developed

SPECT-map code (By Dr. James Bowsher, Duke University Medical Center). The

geometric sensitivity (S_g) and the total sensitivity (S_{total}) can be choosen in SPECT-map,

with the specific attenuation coefficient for Tc-99m of 36.4 cm^{-1} and for I-131 of 4.41 cm^{-1}[150]. The number of detected photons was measured by drawing a ROI around the

projected sphere. The sensitivity of the projection data was calculated as

$$\frac{\# \ of \ photons \ detected}{A_c \ \times V \times 37000 \frac{Bq}{\mu Ci}} \tag{11}$$

The measured sensitivities were normalized to $\theta = 90 \ deg$. The normalized S_g

and S_{total} were plotted versus angle θ for Tc-99m and I-131 as shown in Figure 24(b) and

Figure 25(b), respectively. The sensitivity plot from the literature is shown in Figure

24(a) and Figure 25(a)[48]. The SPECT-map calculated sensitivities were superimposed to

the literature sensitivities. Figure 24(c) and Figure 25(c) show that our simulation results

were consitent with the literature results.
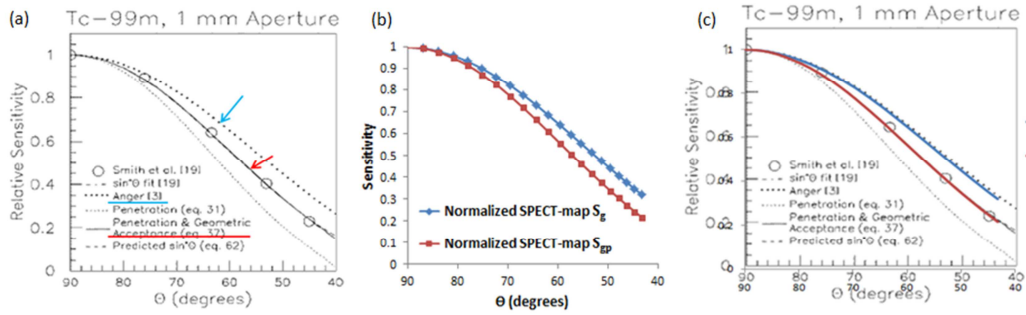
Figure 24: Relative sensitivity versus the angle θ plot for Tc-99m radiotracer. (a) Metzler et. al. plot[48]. The dotted curve (indicated by the blue arrow) is the geometric sensitivity (S_g). The solid curve (indicated by the red arrow) is the geometric and penetration sensitivity (S_{total}). (b) SPECT-map measured S_g and S_{total}. (c) Superimposed sensitivity curves of (a) and (b) indicates that SPECT-map sensitivity calculation is consistent with the literature.
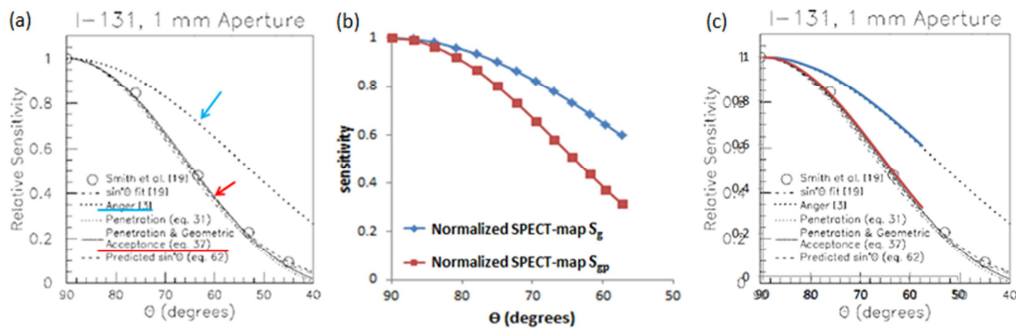
Figure 25: Relative sensitivity versus the angle θ plot for I-131 radiotracer. (a) Metzler et. al. plot[48]. The dotted curve (indicated by the blue arrow) is the geometric sensitivity (S_g). The solid curve (indicated by the red arrow) is the geometric and penetration sensitivity (S_{total}). (b) SPECT-map measured S_g and S_{total}. (c) Superimposed sensitivity curves of (a) and (b) indicates that SPECT-map sensitivity calculation is consistent with the literature.

Besides the relative sensitivity verification shown in Figure 24 and Figure 25, the

sensitivity and resolution were also validated by comparing the measured values to the

hand-calculations using the designed trajectories specifically related to the simulation

imaging study of lung as detailed in Chapter 7, Section 7.3.

4.3 Comparison of Sensitivity and Resolution between 49-Pinhole SPECT System and Parallel-Hole SPECT System

The sensitivity and resolution of the 49-pinhole SPECT system were calculated

and compared to the Digirad parallel-hole SPECT system.

The pinhole focal length (f) was 12 cm. Pinhole diameter was 3 mm or 4 mm.

The radius-of-rotation (ROR) varied from 2 cm to 18 cm. The parallel-hole system

parameters are shown in Table 2. Three different parallel-hole collimators from Digirad

(DIGIRAD Corp., Poway, CA) were used: low energy high resolution (LEHR), low

energy all purpose (LEAP) and cardiac collimator (CARD). The branching ratio of Tc-

99m was 0.879. The detector efficiency was 0.85. The fill factor for parallel-hole detector

was 0.79[51]. The intrinsic resolution of the detector was 0.325 cm.

Figure 26 shows the semi-log plot of sensitivity versus resolution for 49-pinhole

and parallel-hole systems. As the ROR increases from 2 cm to 18 cm, the sensitivity of

the 49-pinhole system decreases while that of the parallel-hole system remains the same.

The LEAP collimator and the 4 mm diameter pinhole have higher sensitivity. The

proximity of the 49-pinhole to the imaging ROI improves the sensitivity. In general, 49-

pinhole system has one to two orders of magnitude more sensitivity than parallel-hole

system depending on the ROR.

The resolution of both systems degraded as the ROR increased. The LEHR

collimator has better resolution at each ROR than the CARD and LEAP collimators. The

3 mm diameter pinhole results in better resolution than the 4 mm diameter pinhole. The

tradeoff between sensitivity and resolution is indicated in Figure 26 – higher resolution

is compromised by lower sensitivity and vice versa.

Table 2. Digirad 2020tc parallel-hole collimator parameters. Three different collimators are studied: low energy high resolution (LEHR), low energy all purpose (LEAP) and cardiac collimator (CARD).

Parameters	Digirad 2020tc parallel-hole SPECT		
	LEHR	LEAP	CARD
Hole diameter d (cm)	0.15	0.15	0.15
Hole length l (cm)	3.2	2.2	2.7
Effective hole length l_{eff}(cm)	3.12	2.12	2.62
Hole thickness (cm)	0.02	0.02	0.02
Collimator hole shape K	0.26	0.26	0.26
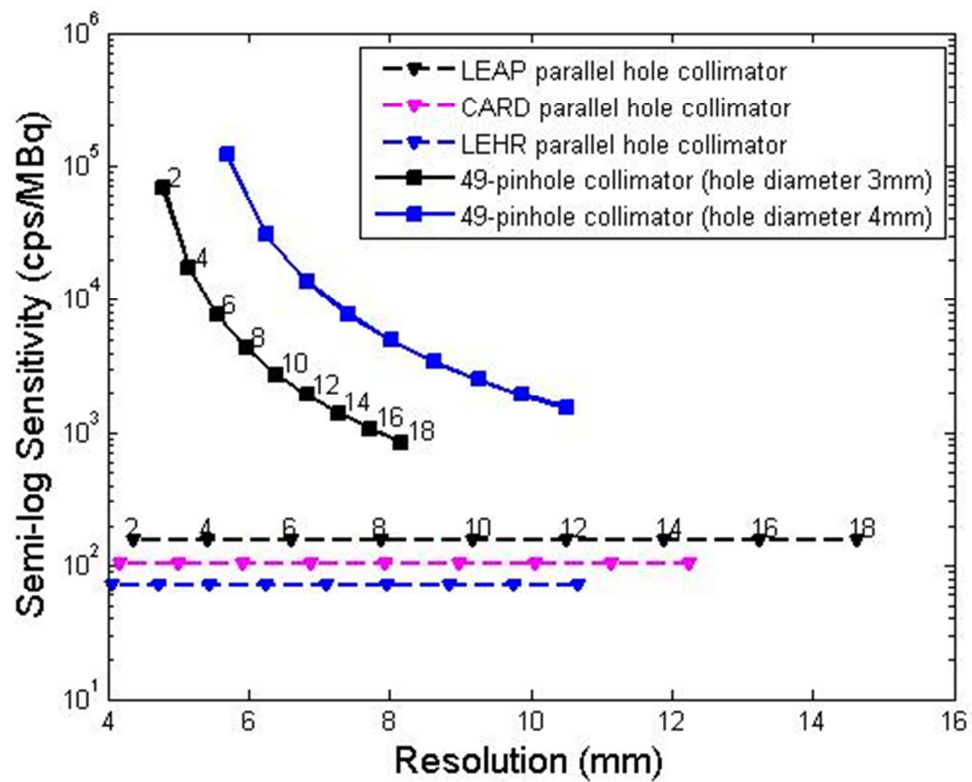
Figure 26: Semi-log sensitivity (cps/MBq) versus resolution (mm) for 49-pinhole systems and parallel-hole systems. The numbers next to the data points are the ROR.

4.4 Conclusion

The in-house developed SPECT-map code has been validated by comparing the

measured sensitivity to the literature. In addition, the calculated sensitivity and

resolution of the 49-pinhole system show better sensitivity and resolution tradeoffs than

the parallel-hole system.

5. Line-Source Method for Aligning On-board and other Pinhole SPECT Systems

5.1 Introduction

For accurate target localization, the coordinate frame of the multi-pinhole SPECT system should be registered to that of the LINAC. Therefore, alignment methods are crucial.

Many alignment methods have been proposed for pinhole imaging and the closely related geometry of cone-beam imaging. While a detailed and thorough review is beyond the scope of this thesis, some previous work is described in order to convey their limitations. Typically, these methods have involved point sources and multiple projection views. Often a known shape has been assumed for the detector trajectory or the alignment method has been constructed to estimate deviations about a known shape. In some cases knowledge of the azimuthal detector angles has been assumed. Alignment calibration methods for cone-beam geometry were developed in[52-55]. One method[52] used an alignment point source to estimate three alignment parameters (distance from focus to center of rotation, focal length, and location of projection of center of rotation) plus the 3-dimensional coordinate of the alignment point source. This method utilized multiple known projection angles over a 360° imaging trajectory. Later, a method[53] suggested that seven parameters are sufficient to calibrate the cone-beam geometry for a

circular motion in which the azimuthal angles are known. Those seven parameters were either intrinsic parameters describing the detector geometry, or extrinsic parameters that change with detector position. The intrinsic parameters can be measured separately from the extrinsic parameters by using a grid of point sources. The extrinsic parameters can then be estimated using a point source. Another method[54] also estimated three extrinsic parameters separately from intrinsic parameters using a grid of 9, 16 and 25 spheres. Although this method estimated the azimuthal angle of the camera, many spheres were used. Another method[55] was proposed that used a different optimization method to estimate six alignment parameters from two point sources and six detector views. Subsequently methods were developed for SPECT pinhole alignment[56-61], often incorporating methods similar to those for cone-beam. Many of these methods utilize multiple pinhole projection views. A second issue is that some previous methods have assumed a specific pinhole trajectory shape, such as a circle[56]. Third, studies[57, 59, 60] have shown that there may be small deviations from the intended pinhole trajectory, and some methods have emphasized estimation of angle-dependent deviations from the assumed trajectory shape[60]. Herein, a method is proposed which makes no assumptions about trajectory shape and which estimates alignment parameters from a single pinhole projection view. This allows determination of the relative orientations of individual pinholes within a multi-pinhole system, which may be important since gravity can cause

these relative orientations to change with orientation of the overall multi-pinhole system.

Finally, point sources can be challenging to produce. For example, if the point source consists of a droplet of radiotracer together with X-ray or MRI contrast agent, it can be challenging to enclose this droplet in a container that is uniformly attenuating in all directions of 3-dimensional space. Consequently, with attenuation greater in some directions, scatter will also be greater, and this can shift the apparent location of the point source. If the point source is generated by more sophisticated processes that can achieve uniform attenuation in all directions, then it may be necessary to use long-lived radionuclides in order to justify the cost of more sophisticated procedures. Long-live radionuclides present increased costs for secure storage and management of regulatory issues. Another approach to generating point sources is to construct a line source that has very short length in the linear direction. Here again though it can be cumbersome to achieve a short length in the linear direction. In contrast, a line source can simply be a straight tube which is capped after a solution of radiotracer and contrast agent is simply injected into the tube with a syringe. The process is fast and simple, so short-lived radionuclides can be used. Therefore, this paper proposes an alignment method that is derived assuming – and therefore accurately models – line sources. In a line-source model, the attenuating medium need be uniform only in the two dimensions perpendicular to the line sources, and this is easily implemented physically. One

47

previous method based on line sources proposed to use the intersection of line source

projections, with each intersection considered a "virtual" point source[62]. The method

proposed in this paper takes a different approach: The full projection of each line source

is incorporated to estimate alignment parameters without relying on the intersections of

lines.

The alignment method proposed here is applicable for both single pinhole and

multi-pinhole SPECT systems. In both cases, alignment can be performed for each

individual pinhole. Therefore, the exact aim of this chapter is to develop and evaluate a

method for estimating the alignment parameters of a single-pinhole SPECT system.

5.2 Materials and Methods

5.2.1 Alignment Model

The alignment method considers a pinhole SPECT detector and a line-source

phantom. Three coordinate frames are defined: a reference room coordinate frame

(XYZ), a detector coordinate frame (uvw), and an intermediate coordinate frame (xyz)

relating XYZ to uvw. For on-board SPECT imaging, the XYZ frame may be that of the

LINAC, with the origin of the XYZ frame corresponding to the typical LINAC isocenter.

Each line source j of the line-source phantom can be represented in the XYZ frame by

the equations:

$$Y = a_j X + b_j = f_j^Y(X)$$

(12)

$$Z = c_j X + d_j = f_j^Z(X).$$

(13)

In on-board SPECT imaging, for example, the coefficients $\{a_j, b_j, c_j, d_j : j = 1 \ldots NumLines\}$ could be determined from a cone-beam CT (CBCT) image of the line-source phantom.

The xyz frame is a rotation of the XYZ frame such that the xyz axes point respectively in the same directions as the uvw axes. The detector rotation angle θ, tilt angle Φ and twist angle Ψ are, respectively, rotations about the initial Z-axis, the rotated X-axis, and the twice rotated Y-axis.

$$\begin{pmatrix} x \\ y \\ z \end{pmatrix} = R_{twist} R_{tilt} R_{rotate} \begin{pmatrix} X \\ Y \\ Z \end{pmatrix} = R \begin{pmatrix} X \\ Y \\ Z \end{pmatrix}$$

(14)

$$R_{rotate} = \begin{pmatrix} \cos\theta & \sin\theta & 0 \\ -\sin\theta & \cos\theta & 0 \\ 0 & 0 & 1 \end{pmatrix}$$

(15)

$$R_{tilt} = \begin{pmatrix} 1 & 0 & 0 \\ 0 & \cos\Phi & \sin\Phi \\ 0 & -\sin\Phi & \cos\Phi \end{pmatrix}$$

(16)

$$R_{twist} = \begin{pmatrix} \cos\Psi & 0 & -\sin\Psi \\ 0 & 1 & 0 \\ \sin\Psi & 0 & \cos\Psi \end{pmatrix}$$

(17)

The origin of the uvw coordinates corresponds to the center of the SPECT detector. The v-axis is perpendicular to detector. Figure 27 and equations (20)-(21) show the translations which relate the xyz and uvw coordinates of a point. The detector shifts

x_{det} and z_{det} are detector translations along the x and z axes, and y_{det} is the detector

radius of rotation.

$$u = x - x_{det} \qquad (18)$$
$$v = y - y_{det} \qquad (19)$$
$$w = z - z_{det} \qquad (20)$$
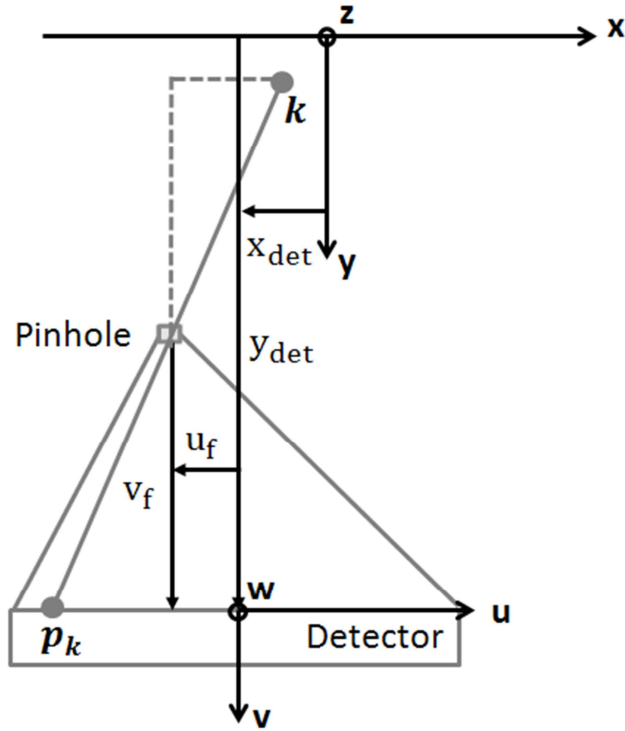
Figure 27: Pinhole projection p_k of a point k. The xyz coordinates are parallel to the uvw coordinates, with the z-axis and w-axis pointing into the paper. The grey dot k represents a point. The grey dot p_k on the detector represents the pinhole projection of this point. The detector translations x_{det} and z_{det} are the detector shifts in the x-axis and z-axis directions from the xyz origin. The pinhole translations u_f and w_f are relative to the detector center, which intercepts the v-axis. The detector radius of rotation y_{det} and pinhole focal length $-v_f$ are along the v-axis direction.

Consider pinhole collimation for the detector (Figure 27), with the pinhole located at (u_f, w_f) relative to the detector centerline (v-axis) and at v_f relative to the detector measurement plane. The pinhole focal length is $-v_f$. The pinhole projection of a point k (x_k, y_k, z_k) is a point p_k $(u_{p_k}, v_{p_k}, w_{p_k})$. This projection can be calculated by similar triangles:

$$\frac{-v_f}{y_k - y_{det} - v_f} = \frac{u_{p_k} - u_f}{x_k - x_{det} - u_f} = \frac{w_{p_k} - w_f}{z_k - z_{det} - w_f} \quad (21)$$

$$v_{p_k} = 0 \quad (22)$$

Solving for u_{p_k} and w_{p_k} gives:

$$u_{p_k} = \frac{-v_f \times (x_k - x_{det} - u_f)}{y_k - y_{det} - v_f} + u_f \quad (23)$$

$$w_{p_k} = \frac{-v_f \times (z_k - z_{det} - w_f)}{y_k - y_{det} - v_f} + w_f \quad (24)$$

The pinhole translations u_f, v_f and w_f are assumed to be known. Consider an isolated radioactive point source k, where (X_k, Y_k, Z_k) could be known by, for example, CBCT imaging. The (x_k, y_k, z_k) of (25)-(26) could then be determined by (16)-(19) given the alignment parameters θ, Φ, and Ψ. The projection (u_{p_k}, w_{p_k}) of k could be observed on the detector. The unknowns in (25)-(26) would therefore be the six alignment parameters (x_{det}, y_{det}, and z_{det}) (explicitly) and (θ, Φ, Ψ) (implicitly). Explicitly means that the three translation parameters are directly expressed in the (25)-(26). Implicitly

means that the three rotation parameters are not directly expressed in (25)-(26). They are instead implied by rotation matrix in (16)-(19) and expressed as x_k, y_k and z_k in (25)-(26).

5.2.2 Estimation of Alignment Parameters

To estimate alignment parameters from line sources, two points (p_{jk}: k =1,2) are selected on each line-source projection (j: $j = 1 \dots NumLines$), where the earlier single-indexing over points k is replaced with double-indexing over line sources j and points k on each line source. The two points are selected to be far apart yet still within the pinhole field of view. Projection coordinates of these points are now denoted $(u_{p_{jk}}, w_{p_{jk}})$.

Compared to point sources, line sources introduce implicit unknown point coordinates (X_{jk}) in (25)-(26). These unknowns need to be estimated in addition to the six alignment parameters (x_{det}, y_{det}, z_{det}, θ, Φ, Ψ). The XYZ coordinates of a point source can be obtained from CBCT, whereas the coordinates of a point on a line source cannot be observed by CBCT. However, CBCT can observe the line source which contains the point. This information is reflected in the coefficients $\{a_j, b_j, c_j, d_j : j = 1 \dots NumLines\}$ which specify that if the X coordinate of a point is known, then so also are the Y and Z coordinates.

The two point sources on each line source provide four independent equations – two instances each of (25) and (26). Thus three line sources provide 12 independent equations and also 12 unknowns, which are the six alignment parameters and the six point coordinates (X_{jk}).

An objective function F is formed as the sum of the squares of the differences

between iteratively estimated point-source projections $(u_{p_{jk}}^{(n)}, w_{p_{jk}}^{(n)})$ and measured

projections $(u_{p_{jk}}^{M}, w_{p_{jk}}^{M})$.

$$F = \sum_{j=1}^{NumLines} \sum_{k=1}^{2} \left(u_{p_{jk}}^{(n)} - u_{p_{jk}}^{M}\right)^2 + \left(w_{p_{jk}}^{(n)} - w_{p_{jk}}^{M}\right)^2 \qquad (25)$$

The alignment parameters and point coordinates (X_{jk}) were then iteratively

estimated by a Levenberg-Marquardt algorithm, which was implemented on a

commercial software package (MATLAB R2011b Optimization Toolbox™, The

MathWorks Inc., Natick, MA, 2000)[63]. The input equations to this optimization algorithm

were (14)-(22) and (25)-(27). Equations (25) and (26) enable the algorithm to calculate the

estimated projections $(u_{p_{jk}}^{(n)}, w_{p_{jk}}^{(n)})$ at iteration n. In turn, the relations of the parameters in

(25) and (26) are provided by (14)-(22). The input also included initial values for the

estimated alignment parameters $(x_{det}, y_{det}, z_{det}, \theta, \Phi, \Psi)$ and point coordinates (X_{jk}).

The measured projections $(u_{p_{jk}}^{M}, w_{p_{jk}}^{M})$ were also given to the algorithm. The $(u_{p_{jk}}^{M}, w_{p_{jk}}^{M})$

are any two points selected from a line-source projection, where the angle and offset of

the line-source projection are determined using the Radon transform, as described in

5.2.3.

5.2.3 Angles and Offsets of Line-Source Projections

The coordinates of the measured projection $(u_{p_{jk}}^M, w_{p_{jk}}^M)$ can be obtained by using

the Radon transform to detect the ridge of the line-source projection. The Radon

transform converts the line-source projections into angles (α) and offsets (ρ) that

parameterize line-source projections. Figure 3 demonstrates a case with a single line

source. The grey line segment in Figure 28(a) shows a single pinhole projection of a line

source. The offset (ρ) is the perpendicular distance from the center of the projection

image to the line-source projection. The angle (α) is between the horizontal-axis and the

offset-axis. Figure 28(b) shows the Radon transform of this line-source projection. The

(α_0, ρ_0) corresponding to the maximum pixel value of the Radon transform represents

the ridge of the line-source projection, as shown by the red line in Figure 28(a).

Coordinates $(u_{p_{jk}}^M, w_{p_{jk}}^M)$ of points on this red line can be calculated via:

$$\rho_0 - u_{p_{jk}}^M \cos \alpha_0 - v_{p_{jk}}^M \sin \alpha_0 = 0. \qquad (26)$$
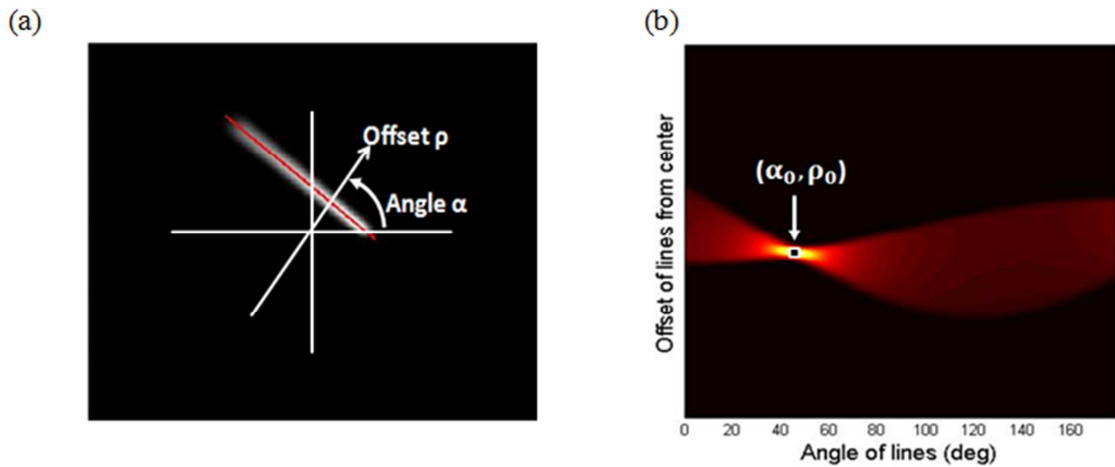
Figure 28: (a) The grey line segment is a single pinhole projection of a line source. The red line is the estimated ridge of the line-source projection and is computed using (28), where (α_0, ρ_0) corresponds to the maximum pixel value determined from the Radon transform of the line-source projection. The offset (ρ) is the perpendicular distance from the center of the projection image to the ridge of the line-source projection. The angle (α) is between the horizontal-axis and the offset-axis. (b) Radon transform of line-source projection in (a), where (α_0, ρ_0) is the angle and offset corresponding to the maximum pixel value of the Radon transform and is used to draw the red line in (a).

5.2.4 Evaluation of Alignment Model

To evaluate the proposed alignment approach, a series of computer simulations were performed. Figure 29(a) shows the computer simulated 3D phantom with dimensions of 256x256x256 and voxel width of 0.05 cm. The phantom includes five line sources. Table 1 shows the geometries of the five line sources used in this paper. Each line was simulated to have 7.4 MBq of Tc-99m and with a diameter of 1.4 mm. A noise-free 2D projection of these line sources was computer simulated on a 256x256 grid with 0.1 cm-wide pixels. The simulation modeled sensitivity[64] using effective pinhole diameter for a tungsten pinhole with 2mm pinhole diameter, a 100° full pinhole opening

55

angle, 18cm pinhole-to-image distance (focal length), detector intrinsic resolutions of 1.5 mm, 2.5 mm and 3.5 mm, a Tc-99m branching ratio of 0.879, a gamma camera efficiency of 0.86, and a 10 sec acquisition time. This 10 sec acquisition time was only used for the simulation. In the actual measurement, 13 min and 1 min were used for acquiring projection image. Pinhole resolution was modeled by tracing ray distribution through the pinhole. Pinhole septal penetration was simulated. Photon scatter was not simulated. Noisy projections, shown in Figure 29(b), were generated by pseudo random sampling from corresponding Poisson distributions. The random Poisson noise was used to generate different noisy projections (noisy realizations) which were used to perform statistical analysis.

(a)   (b)
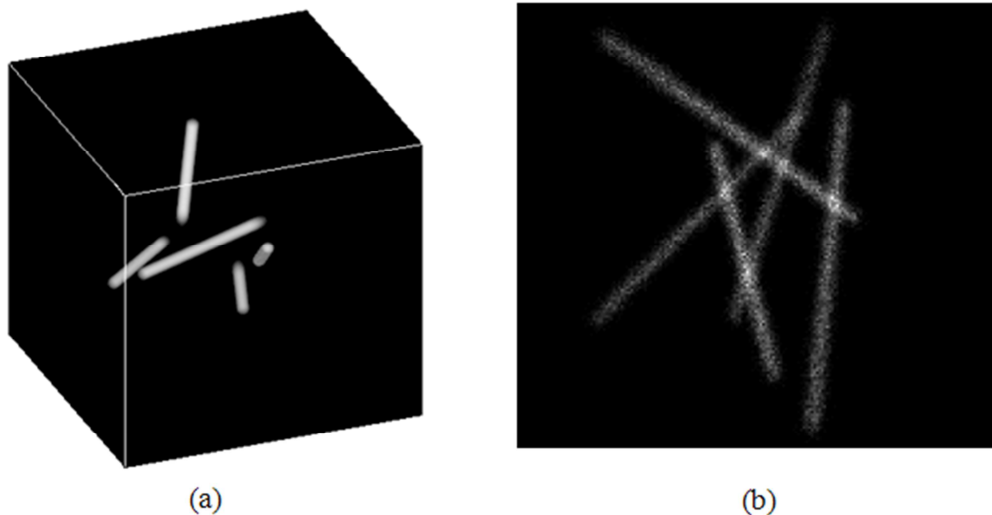
Figure 29: (a) Computer simulated line-source phantom with five line sources. (b) Projection image of the line-source phantom with pseudo random sampling from corresponding Poisson distributions.

Table 3. Simulated line source geometry used in this paper as shown in Figure 29(a), specified using the coefficients (a,b,c,d) of Eqns. (14)-(15).

Line	a	b	c	d	X	Y	Z
1	2.00	3.075	1.00	2.00			
2	-2.85	-5.14	3.15	6.31			
3	-0.96	1.14	0.96	-0.89	X_j	$Y_j = a_j X_j + b_j$	$Z_j = c_j X_j + d_j$
4	3.50	-7.31	-3.00	5.70		$j = 1,2 \dots 5$	
5	1.00	-1.50	-6.38	2.53			

Table 4. Four experiments designed to evaluate the proposed alignment procedure.

Study	Parameters Estimated		Number of Line Sources	Method for Line Projection Positions
	Detector Translation	Detector Rotation		
A	$x_{det}, z_{det}, y_{det}$	θ, Φ, Ψ	3	True angle & offset
B	$x_{det}, z_{det}, y_{det}$	θ, Φ, Ψ	3	Radon Transform
C	$x_{det}, z_{det}, y_{det}$	θ, Φ, Ψ	4	Radon Transform
D	$x_{det}, z_{det}, y_{det}$	θ, Φ, Ψ	5	Radon Transform

Study A as specified in Table 4 was conducted to evaluate the estimation of six

alignment parameters from 3 line sources when true values of angles (α) and offsets (ρ)

were given. In the other studies, these true values were replaced with angles and offsets

estimated by Radon transform, which are subject to error, and the accuracy with which

the Radon transform determined angles (α) and offsets (ρ) was evaluated as $|\alpha_{Radon} -$

$\alpha_{True}|$ and $|\rho_{Radon} - \rho_{True}|$.

Studies B, C and D were conducted with three, four and five line sources as

detailed in Table 4. These studies evaluated the error in estimation of six alignment

parameters when line-source-projection angles (α) and offsets (ρ) are determined from

Radon transform. The estimation error was calculated as the absolute error between estimated and true values of alignment parameters, $|Parameters_{Estimated} - Parameters_{True}|$. For each study, 400 noisy realizations were generated. Two-tailed Wilcoxon rank sum tests with 5% significance level were performed to calculate the p-values for study B, C and D. These tests have the null hypothesis that distribution of errors from 4 line sources are equal to that of 3 line sources; distribution of errors from 5 line sources are equal to that of 3 line sources and distribution of errors from 5 line sources equal to that of 4 line sources.

The simulations involving three different detector intrinsic resolutions, 1.5 mm, 2.5 mm and 3.5 mm, were used to investigate the effects of blur on estimation of alignment parameters. For each detector intrinsic resolution, 400 noisy realizations were generated. Two-tailed Wilcoxon rank sum tests with 5% significance level were performed to calculate the p-values for study B, C and D. These tests have the null hypothesis that distribution of errors from 1.5 mm are equal to that of 3.5 mm, distribution of errors from 2.5 mm are equal to that of 3.5 mm and distribution of errors from 1.5 mm are equal to that of 2.5 mm.

The influence of activity concentration was investigated with three difference concentrations of 1.85 MBq, 7.40 MBq and 14.80 MBq per line. For each activity concentration, 400 noisy realizations were generated. Two-tailed Wilcoxon rank sum tests with 5% significance level were performed to calculate the p-values for study B, C

and D. These tests have the null hypothesis that distributions of errors from 1.85 MBq per line are equal to 7.40 MBq per line, distributions of errors from 1.85 MBq per line are equal to 14.80 MBq per line and distributions of errors from 7.40 MBq per line are equal to 14.80 MBq per line.

To examine the effects of acquisition geometry on alignment parameter estimation, four tests were conducted as detailed in Table 5. For statistical analysis, an ensemble of 100 noisy projection images was generated for each acquisition geometry. The non-parametric Kruskal-Wallis test was used to compare the medians of the estimation errors from four different acquisition geometries. This test has the null hypothesis that all samples are drawn from the same distribution with p-value of 5% significance level. For p-value less than 5%, this test rejects the null hypothesis and suggests that at least one sample median is significantly different from the others[65].

To further evaluate the effects of blur and noise on estimation accuracy, noise-free line-source projections were simulated with 0 mm detector intrinsic resolution and perfect pinhole spatial resolution. These noise-free, unblurred line-source projections were used to estimate alignment parameters for each acquisition geometry. The errors in estimating each alignment parameter were compared to those for noisy projections and 3.5 mm detector intrinsic resolution.

Seven parameters (x_{det}, z_{det}, y_{det}, Φ, Ψ, u_f and v_f) are also estimated using five lines with activity concentration of 14.80 MBq per line and 3.5 mm intrinsic detector

resolution. An ensemble of 400 noise realizations was used to generate the box-and-whisker plot.

Table 5. Four different acquisition geometries. The top first row of each acquisition geometry is the true values of alignment parameters. The true values are those used to compute the 2D line-source projections. The start points are the initial values in the iterative parameter estimation.

Acquisition Geometry		Unknown Alignment Parameters						Pinhole Position		
		x_{det} (mm)	z_{det} (mm)	y_{det} (mm)	θ (deg)	Φ (deg)	Ψ (deg)	u_f (mm)	w_f (mm)	$-v_f$ (mm)
1	True Value	30	20	300	30	10	5	-20	-30	180
	Start Point	10	0	280	28	8	2			
2	True Value	20	40	300	10	5	60	-10	-30	180
	Start Point	0	10	280	0	0	53			
3	True Value	30	40	300	72	47	12	-10	-10	180
	Start Point	10	10	280	70	44	9			
4	True Value	10	20	320	10	160	5	-20	-10	180
	Start Point	0	0	290	6	155	0			

5.2.5 Experimental evaluation of alignment method

The alignment method was also evaluated using a physical line-source phantom and a robotic SPECT system with a single 2-mm-diameter pinhole collimator attached (Figure 30). The robotic SPECT system consists of a Digirad 2020tc detector (Digirad Corporation Poway, CA) attached to a KUKA KR150-L110 robot (KUKA Robotics Corporation, Shelby Township, MI).

60
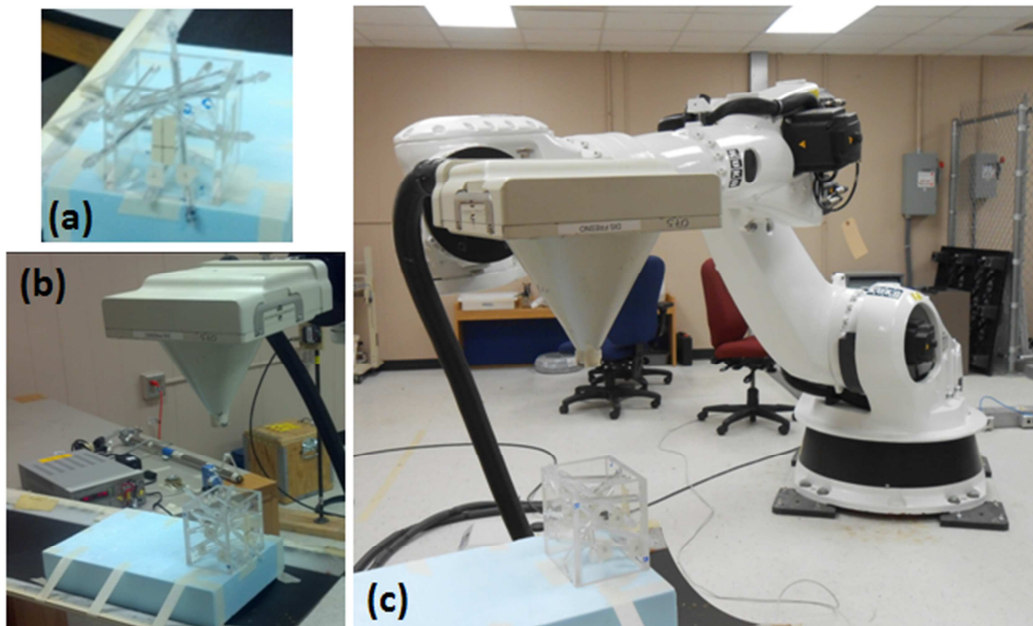
Figure 30: (a) Line-source phantom with Tc-99m injected in five lines. (b) Single pinhole collimated SPECT detector with line-source phantom. (c) SPECT detector attached to robotic arm imaging line-source phantom.

The Digirad 2020tc consists of 64x64 3.25-mm-wide pixels with CsI(TI) scintillator. The imaging area is 20.8 x 20.8 cm². In order to measure pinhole focal length, two parallel line sources were positioned 10 cm apart and scanned at 5 pinhole-to-line-source distances. The measured focal length was 174.6 mm. By scanning one of these line sources, pinhole shifts relative to the detector were measured to be u_f = 1.6 mm and v_f = 7.3 mm.

The line-source phantom consists of 4 acrylic sides and 11 acrylic tubes with 3/16" inner diameter. For this experiment, Tygon tubes with 1/16" inner diameter were inserted in 5 of the 11 acrylic tubes. A CT image of the line-source phantom was

acquired. For each of the 5 lines, the coefficients (a, b, c, d) as shown in (1)-(2) were determined in the CT (XYZ) coordinate frame from the CT image. These coefficients are shown in Table 6. The robot system includes tool and base coordinate frames along with techniques for registering these frames[66]. The ($u_T v_T w_T$) axes of the tool coordinate frame were calibrated to be parallel to the detector (*uvw*) coordinates, with their origin along the pinhole symmetry axis and in the plane of the phantom-side surface of the pinhole insert. The (XYZ) axes of the robot base coordinate frame were registered to the CT (XYZ) axes, using the orientation of the line-source phantom as an indication of the CT (XYZ) axes. Since there is no CT scanner in the room with the robotic SPECT system, the above procedure was performed so that the robot base coordinate frame would serve the role of the CT coordinate frame. If this experiment had been performed on a commercial SPECT-CT system, true alignment parameters for the pinhole-collimated SPECT system would presumably have been obtained from detector position and angle read-outs on the SPECT-CT system. Here, by calibrating the robot tool coordinate frame with the pinhole-collimated SPECT detector, true alignment parameters can similarly be given by the robot system. These true alignment parameters were then compared with those estimated using the alignment method and line-source phantom developed herein.

Table 6. Physical line source geometry determined in the CT (XYZ) coordinate frame from the CT image, specified using the coefficients (a, b, c, d) of Eqns. (1)-(2).

Line	a	b	c	d	X	Y	Z
1	2.60	-2.05	-2.43	1.68			
2	-2.19	3.13	7.03	0.74			
3	-0.60	-2.06	1.77	6.47	X_j	$Y_j = a_j X_j + b_j$	$Z_j = c_j X_j + d_j$
4	-0.26	-3.09	0.34	0.23		$j = 1,2\dots5$	
5	-0.17	1.02	-0.30	0.87			

SPECT projections were acquired at 3 different detector locations, as indicated in Table 7. The start point of each parameter was varied to investigate the convergence of (27). At each detector location, acquisitions were obtained with 13 minute and 1 minute scan times. The 5 tubes of the line-source phantom were filled a Tc-99m activity concentration that was 0.725 MBq/cm at the time of acquisition for geometry 2, which averages to about 10.73 MBq per line. Geometries 1 and 3 were acquired 47 minutes before and 147 minutes after geometry 2, respectively.

Table 7. Three acquisition geometries for scanner-acquired projections of the physical line-source phantom. The top first row for each acquisition geometry is the true value as given by the robot tool coordinate frame. The second row gives initial values in the iterative parameter estimation.

Acquisition Geometry		x_{det} (mm)	z_{det} (mm)	y_{det} (mm)	θ (deg)	Φ (deg)	Ψ (deg)
				Unknown Alignment Parameters			
1	True Value	-1.7	-7.3	378.9	180	0	0
	Start Point	20	10	350	174	3	4
2	True Value	-1.6	-7.4	385.7	225.0	-0	0
	Start Point	20	10	420	220	4	3
3	True Value	-1.85	-7.3	400.4	180	-60	-0.1
	Start Point	30	20	450	175	-55	3

5.3 Results

Study A shows perfect results in estimating six alignment parameters with three line-source projections using theoretical angles (α) and offsets (ρ). The average error in estimating line angle (α) and offset (ρ) from Radon transform of three line sources are 0.34° and 0.27 mm, respectively.

Figure 31 shows box-and-whisker plots of alignment parameter error across an ensemble of 400 noisy realizations for studies B, C and D with 3, 4 and 5 line sources, respectively. The box-and-whisker plot is implemented as follows: the length of the box represents the interquartile range (IQR), the bottom end of the box is the 25% quartile (Q1), the horizontal line inside the box is the median quartile (Q2), the top end of the box is the 75% quartile (Q3), the whiskers are on the last data point within 1.5IQR from the end of the box. If there are no data points between the end of the box and 1.5IQR, the whisker is placed at the end of the box. The square boxes outside the whiskers are outliers which are the data points outside the 1.5IQR from either end of the box. Table 8 shows the Q1, Q2 and Q3 values, the highest outlier value and the percent of outliers for each study, along with p-values from two-tailed Wilcoxon rank sum tests with 5% significance level. Parameters estimation errors for Study C (4 line sources) and Study D (5 line sources) both differ from those of Study B (3 line sources) at statistically significant levels, with less error when using 4 or 5 line sources as compared to 3. In comparing Study C and Study D, there were statistically significant less errors in

estimating z_{det} and Ψ from 5 line sources. There were no statistically significant less errors in estimating x_{det}, y_{det}, θ and Φ using 5 line sources than 4 line sources.
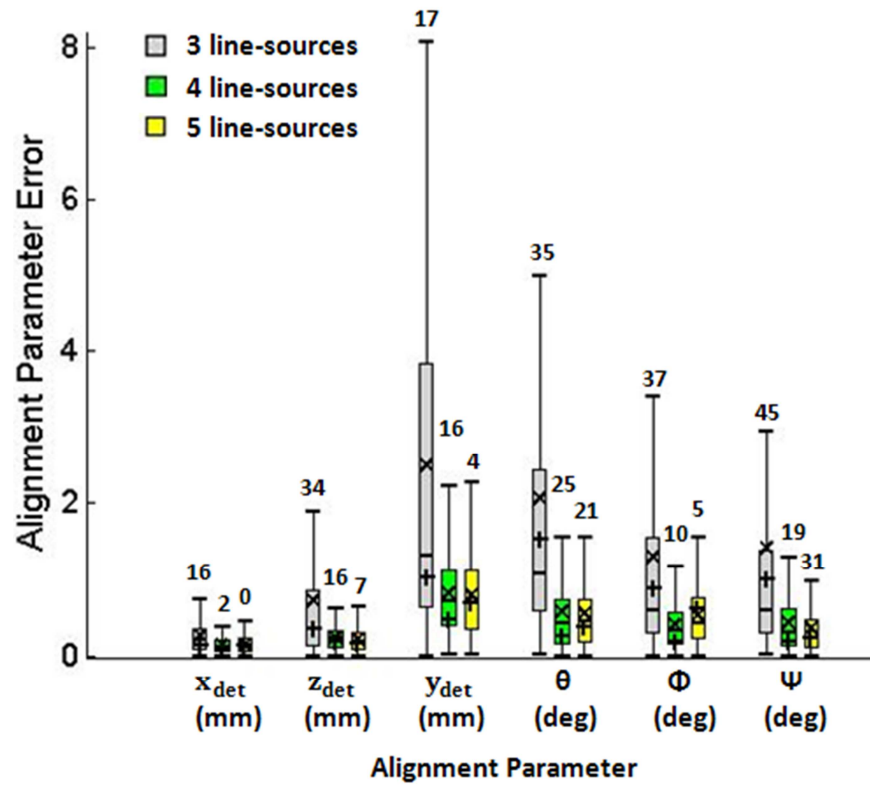
Figure 31: Errors in estimating six alignment parameters for Study B using 3 line sources, Study C using 4 line sources and Study D using 5 line sources (from left to right). Each distribution is obtained from 400 noisy realizations. The number above each whisker is the number of outliers. The mean of each distribution is represented by an "x". Errors in parameter estimation from noise-free projections are represented by a "+".

Table 8. The 25% quartile (Q1), the median quartile (Q2), and the 75% quartile (Q3) values of the estimated alignment parameters of Study B, C and D. The highest outlier values and the percent of outliers of each estimated alignment parameters of Study B, C and D. P-values are from two-tailed Wilcoxon rank sum test with 5% significance level. Numbers in bold are p<0.05.

		x_{det} (mm)	z_{det} (mm)	y_{det} (mm)	θ (deg)	Φ (deg)	Ψ (deg)
Study B (3 line sources)	Q1	0.10	0.14	0.64	0.59	0.29	0.30
	Q2	0.20	0.36	1.30	1.07	0.60	0.59
	Q3	0.37	0.85	3.84	2.43	1.56	1.39
	Highest outlier	1.55	6.06	17.55	16.40	12.91	13.38
	Percent of outliers (%)	4.00	8.50	4.25	8.75	9.25	11.25
Study C (4 line sources)	Q1	0.07	0.12	0.40	0.17	0.16	0.14
	Q2	0.12	0.22	0.71	0.42	0.32	0.30
	Q3	0.20	0.32	1.13	0.74	0.57	0.61
	Highest outlier	0.57	1.05	2.87	3.37	1.75	2.71
	Percent of outliers (%)	0.50	4.00	4.00	6.25	2.50	4.75
Study D (5 line sources)	Q1	0.06	0.08	0.36	0.18	0.23	0.11
	Q2	0.13	0.18	0.70	0.45	0.43	0.24
	Q3	0.22	0.31	1.13	0.74	0.76	0.48
	Highest outlier	0	0.88	3.01	2.24	1.777	1.86
	Percent of outliers (%)	0	1.75	1.00	5.25	1.25	7.75
P-values	Study C vs. Study B	**< 0.001**	**< 0.001**	**< 0.001**	**< 0.001**	**< 0.001**	**< 0.001**
	Study D vs. Study B	**< 0.001**	**< 0.001**	**< 0.001**	**< 0.001**	**< 0.001**	**< 0.001**
	Study D vs. Study C	0.207	**0.006**	0.667	0.907	**< 0.001**	**0.008**

Table 9 shows the Q1, Q2 and Q3 values, the highest outlier value and the percent of outliers of alignment parameter errors across an ensemble of 400 noisy realizations using 5 line sources with three different detector intrinsic resolutions of 1.5 mm, 2.5 mm and 3.5 mm. P-values from two-tailed Wilcoxon rank sum tests with 5% significance level were also shown in Table 7 for differences in estimating alignment parameters given detector intrinsic resolutions of 1.5 mm, 2.5 mm and 3.5 mm. For 1.5 mm versus 3.5 mm detector intrinsic resolution, statistical significant differences were found: detector intrinsic resolution of 1.5 mm has less error for all six alignment

parameters x_{det}, y_{det}, z_{det}, θ, Φ and Ψ. For 2.5 mm versus 3.5 mm detector intrinsic

resolution, statistically significant differences were found: detector intrinsic resolution of

2.5 mm had less error for z_{det}, y_{det} and Φ. For 1.5 mm versus 2.5 mm detector intrinsic

resolution, statistically significant difference was found: detector intrinsic resolution of

1.5 mm had less error for x_{det} and Φ.

Table 9. The 25% quartile (Q1), the median quartile (Q2), and the 75% quartile (Q3) values of the estimated alignment parameters of intrinsic detector resolution of 1.5 mm, 2.5 mm and 3.5 mm. The highest outlier values and the percent of outliers of each estimated alignment parameters. The p-values are from a two-tailed Wilcoxon rank sum test with 5% significance level. Numbers in bold are p<0.05.

		x_{det} (mm)	z_{det} (mm)	y_{det} (mm)	θ (deg)	Φ (deg)	Ψ (deg)
	Q1	0.04	0.06	0.29	0.18	0.16	0.09
	Q2	0.11	0.14	0.57	0.41	0.36	0.23
1.5 mm	Q3	0.21	0.25	0.90	0.63	0.60	0.43
	Highest outlier	0.47	0.72	2.40	2.20	1.61	1.69
	Percent of outliers (%)	0	2.5	1.5	5.25	1	5.25
	Q1	0.05	0.06	0.33	0.15	0.19	0.10
	Q2	0.13	0.15	0.62	0.45	0.38	0.21
2.5 mm	Q3	0.24	0.25	1.00	0.67	0.64	0.43
	Highest outlier	0.24	0.84	3.12	2.61	1.87	2.13
	Percent of outliers (%)	0	2.75	2	4.25	2	6
	Q1	0.06	0.08	0.36	0.18	0.23	0.11
	Q2	0.13	0.18	0.70	0.45	0.43	0.24
3.5 mm	Q3	0.22	0.31	1.13	0.74	0.76	0.48
	Highest outlier	0.22	0.88	3.01	2.24	1.77	1.86
	Percent of outliers (%)	0	1.75	1	5.25	1.25	7.75
	1.5 mm vs. 3.5 mm	**0.033**	**<0.001**	**<0.001**	0.073	**<0.001**	0.088
P-values	2.5 mm vs. 3.5 mm	0.845	**0.001**	0.061	0.315	**0.015**	0.111
	1.5 mm vs. 2.5 mm	**0.019**	0.855	0.111	0.378	0.068	0.883

Figure 32 shows the box-and-whisker plots of alignment parameter errors across

an ensemble of 400 noisy realizations using 5 line sources with 3.5 mm detector intrinsic

resolution for line-source with activity concentration of 1.85 MBq, 7.40 MBq and 14.80 MBq per line. Table 10 shows the Q1, Q2 and Q3 values, the highest outlier value and the percent of outliers, along with p-values from two-tailed Wilcoxon rank sum tests with 5% significance level for differences in estimating alignment parameters given activity concentration of 1.85 MBq, 7.40 MBq and 14.80 MBq per line. For 7.40 MBq versus 14.80 MBq activity concentration, statistical significant differences were found: activity concentration of 14.8 MBq per line has less error for all six alignment parameters x_{det}, y_{det}, z_{det}, θ, Φ and Ψ. For 1.85 MBq versus 14.80 MBq activity concentration, statistically significant differences were found: activity concentration of 14.80 MBq per line had less error for y_{det}, z_{det}, θ, Φ and Ψ. For 1.85 MBq versus 7.40 MBq activity concentration, no statistically significant difference was found.
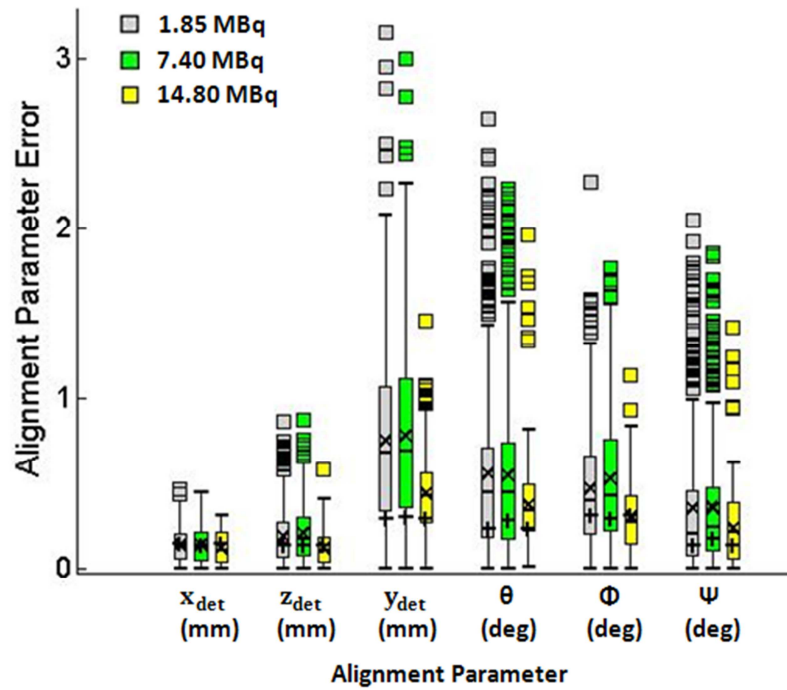
Figure 32: Box-and-whisker plots of alignment parameter error with different activity concentration of 1.85 MBq, 7.4 MBq and 14.8 MBq per line (from left to right). Each distribution is obtained from 400 noisy realizations. The mean of each distribution is represented by an "x". Errors in parameter estimation from noise-free projections are represented by a "+".

69

Table 10: The 25% quartile (Q1), the median quartile (Q2), and the 75% quartile (Q3) values of the estimated alignment parameters of 5 line sources with 1.85 MBq, 7.40 MBq and 14.80 MBq per line with 3.5 mm intrinsic resolution. The highest outlier values and the percent of outliers of each estimated alignment parameters. P-values are from two-tailed Wilcoxon rank sum test with 5% significance level. Numbers in bold are p<0.05.

		x_{det} (mm)	z_{det} (mm)	y_{det} (mm)	θ (deg)	Φ (deg)	Ψ (deg)
	Q1	0.06	0.07	0.35	0.19	0.21	0.08
	Q2	0.13	0.15	0.68	0.45	0.40	0.21
1.85 MBq	Q3	0.21	0.28	1.07	0.71	0.66	0.46
	Highest outlier	0.47	0.87	3.16	2.64	2.28	2.05
	Percent of outliers (%)	0.5	4	1.75	8.75	2	9
	Q1	0.06	0.08	0.36	0.18	0.23	0.11
	Q2	0.13	0.18	0.70	0.45	0.43	0.24
7.40 MBq	Q3	0.22	0.31	1.13	0.74	0.76	0.48
	Highest outlier	0.22	0.88	3.01	2.24	1.77	1.86
	Percent of outliers (%)	0	1.75	1	5.25	1.25	7.75
	Q1	0.05	0.04	0.27	0.23	0.15	0.06
	Q2	0.11	0.11	0.43	0.35	0.27	0.22
14.80 MBq	Q3	0.22	0.19	0.56	0.50	0.43	0.39
	Highest outlier	0.22	0.58	1.46	1.97	1.14	1.43
	Percent of outliers (%)	0	0.25	3.5	1.75	0.5	1.75
p-values	7.40 MBq vs. 14.80 MBq	**0.027**	**< 0.001**	**< 0.001**	**< 0.001**	**< 0.001**	**< 0.001**
	1.85 MBq vs. 14.80 MBq	0.128	**< 0.001**	**< 0.001**	**< 0.001**	**< 0.001**	**0.009**
	1.85 MBq vs. 7.40 MBq	0.566	0.112	0.424	0.763	0.065	0.133

The p-values from non-parametric Kruskal-Wallis test for each alignment parameters x_{det}, z_{det}, y_{det}, θ, Φ and Ψ from the four different acquisition geometries (Table 5) using 5 line sources with 3.5 mm detector intrinsic resolution are less than 0.001. For every alignment parameter, the median errors for at least one of the acquisition geometries were statistically significant different from the others. In addition, the errors in alignment parameters estimated from noise-free and unblurred 5

line-source projections were smaller than the median error of the noisy projections with 3.5 mm detector intrinsic resolution.

Figure 33 shows the box-and-whisker plots of error of 7 alignment parameters using 5 line sources with 3.5 mm detector intrinsic resolution across an ensemble of 400 noisy realizations. Errors of alignment parameters y_{det} and v_f were relative larger than other 5 parameters.
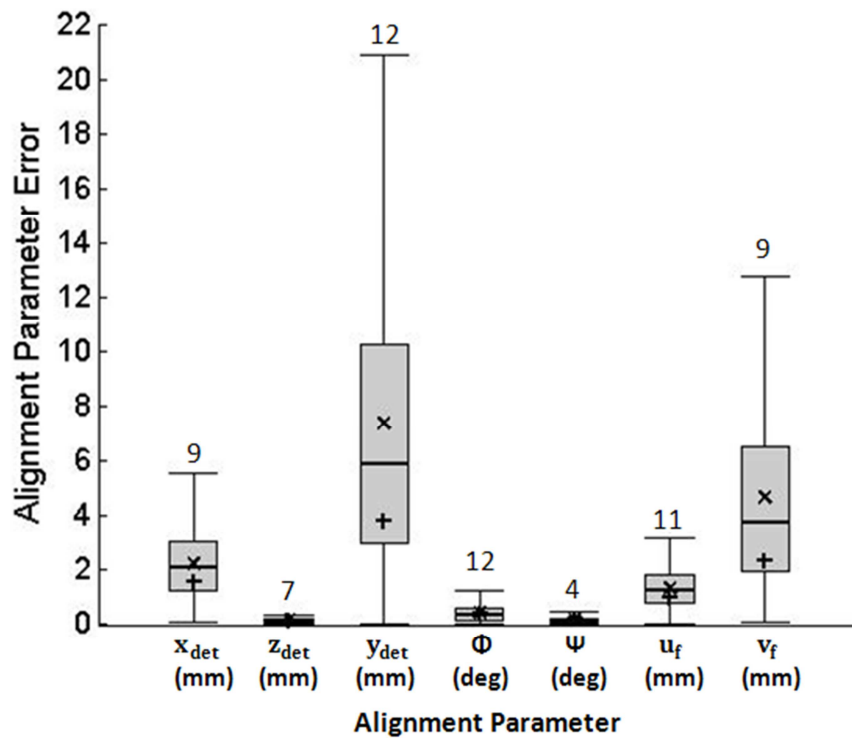
Figure 33: Box-and-whisker plots of alignment parameter error for seven parameters with activity concentration of 14.80 MBq per line and 3.5 mm intrinsic resolution. The number above each whisker is the number of outliers. Each distribution is obtained from 400 noisy realizations. The mean of each distribution is represented by an "x". Errors in parameter estimation from noise-free projections are represented by a "+".

Table 11 shows the error in the six alignment parameters estimated from five line sources using the robotic pinhole SPECT system and physical line-source phantom. Errors estimated from the image with 13 minute scan time are similar to those for 1 minute scan time.

The estimated parameters converge to the same results with the variation of translation over a range of 300 mm and the rotations over a range of 20 degree.

Table 11. The error in alignment parameters estimated from five line-source projections with physical line-source phantom using robotic pinhole SPECT system.

Acquisition Geometry	Scan time (minute)	x_{det} (mm)	z_{det} (mm)	y_{det} (mm)	θ (deg)	Φ (deg)	Ψ (deg)
1	13	-2.28	2.81	-0.53	0.19	-0.68	0.82
	1	-2.35	2.81	-0.20	0.49	-0.57	0.97
2	13	0.57	1.94	-0.18	0.74	0.29	1.89
	1	0.63	2.01	-1.89	0.91	0.49	1.93
3	13	-0.35	2.74	-1.66	-0.46	-0.34	0.77
	1	-0.37	2.75	-1.91	-0.45	-0.17	0.68

5.4 Discussion

Herein a method is proposed for estimating SPECT pinhole alignment parameters using line sources and a single pinhole projection.

In the proposed method, each line-source introduces four generally-independent equations but also two unknowns. Thus, for example, 3 line-sources and 6 unknown alignment parameters results in 12 equations and 12 unknowns. To investigate convergence and uniqueness of the optimization (27), different initial values of the

alignment parameters were considered. Initial values varied by ±300 mm for translation parameters and ±20° for angle parameters. The optimization results were the same for different initial values.

The alignment method can be thought of as involving two components. First, the Radon transform is used to determine the central line of each line-source projection, characterized by angle (α) and offset (ϱ). Second, alignment parameters are estimated based on the angles (α) and offsets (ϱ). Studies A and B considered 3 line sources and 6 unknown alignment parameters. It was found that if true values were used for angles (α) and offsets (ϱ), then alignment parameters were estimated without error. This suggests that errors in estimated alignment parameters are associated with errors in determining angles (α) and offsets (ϱ). Studies C and D showed that alignment errors can be reduced statistically significantly by using more line sources as compared to Study B. Compared to four line sources, five line sources resulted in only a minor reduction of estimation errors. Therefore, four line sources may be preferred because fewer line sources results in less complicated configurations and less radiation dose to personnel.

Sources of error in Radon transform determinations of α and ϱ include rounding errors, finite line-source width, SPECT detector blur, and Poisson noise. The Radon transform routine used in this paper reports line integrals in steps of 1 mm and 0.25° (Figure 28). Selection of the maximum pixel in Figure 28 amounts to a rounding to the

nearest step. For noise-free and unblurred line-source projections, average errors in α and ϱ were 0.20° and 0.24 mm. Since noise and blur are absent, these errors may largely reflect round-off.

In addition, the line-source in 3D space has a diameter of 1.4 mm. This finite volume of the line-source also could affect Radon transform accuracy. The errors in alignment parameters estimated from noise-free and unblurred projection data show the combined effects of round-off and finite line-source width on the alignment parameters $(x_{det}, y_{det}, z_{det}, \theta, \Phi$ and $\Psi)$, since other sources of error (Poisson noise and detector blur) are absent.

Estimation accuracy was studied with different intrinsic detector resolutions of 1.5 mm, 2.5 mm and 3.5 mm. The 1.5 mm detector intrinsic resolution projections yielded statistically significant lower error in estimated alignment parameters than that of 2.5 mm and 3.5 mm intrinsic resolution. A typical intrinsic spatial resolution for sodium iodide detectors is 3.5 mm. For detectors with better intrinsic resolution, such as cadmium zinc telluride (CZT) detectors which can achieve intrinsic resolutions of 1.4 mm[67], estimation accuracy may be improved.

Estimation accuracy was studied with different activity concentration of 1.85 MBq, 7.40 MBq and 14.80 MBq per line. The 14.80 MBq per line activity concentration projections yielded statistically significant lower error in estimated alignment parameters than that of 1.85 MBq and 7.40 MBq.

The Poisson noise effects were studied with noise-free projections. The alignment

errors from noise free projections were generally less than that of noisy projections. The

plus signs in Figure 31,Figure 32 and Figure 33 show the combined effects of round-off,

finite line-source width and detector blur with the absent of noise. These errors are

generally lower than the mean noisy-data errors which are shown as the "x" sign.

Estimation accuracy is also affected by acquisition geometry. The length and the

relative orientation of line-source projections vary with acquisition geometries, and

therefore can affect estimation accuracy. Certain acquisition geometries can cause two

line projections that are superimposed or a line projection appeared as a point. These

projections would reduce estimation accuracy. For example, if a line projects

approximately to a point, the condition number is poor. If a line projects to a point, then

alignment parameters may not be possible to be estimated.

There could be other factors that affect estimation accuracy, such as the length of

line-source and the size of detector and its field of view. Longer line-source projections

might improve the Radon transform in determining line angles, and therefore the

estimation accuracy.

For the computer-simulation studies involving 5 line sources, median errors

were less than 0.5° for angles, 0.7 mm for the detector-to-center-of-rotation distance y_{det}

less than 0.2 mm for the detector shifts x_{det} and z_{det}. A rotation of 0.5° corresponds to a

0.35 mm shift over the radius of an 80-mm-diameter region of interest that might be

scanned by the robotic multi-pinhole system described in the Introduction. This shift and the less-than 0.2 mm detector shifts are much less than the typical translation tolerances of 1 mm or 2 mm for radiation therapy. The distance y_{det} is perpendicular to the planes in which a given pinhole provides localization, and the effect of error in y_{det} may be on the distance scale in reconstructed images. For a 15° pinhole half-opening angle and y_{det} = 300 mm, a 0.7 mm change in y_{det} would change the pinhole field-of-view radius by about 0.2 mm out 80 mm, which is 0.25% effect. The errors reported here are for one pose of a single pinhole, whereas imaging with the robotic SPECT system described in the Introduction would typically involve 10 or more stops with 49 differently-posed pinholes at each stop. Alignment calibration errors may vary with pinhole pose such that when averaged over 500 or more different poses, the errors have little effect on localization and scale. In addition to localization and scale, alignment errors may also affect the quality of reconstructed images, as investigated in previous paper[55-57, 68].

In alignment tests with the physical phantom and robotic SPECT system, angles θ and Φ were in all cases estimated to within 1° of the values given by the CT scan and its registration to the robot base and tool coordinate frames. For angle Ψ, radius of rotation y_{det}, and detector translations x_{det} and z_{det}, errors were within 2°, 2 mm, and 3 mm, respectively. These maximum errors are moderately worse than those obtained in the comparable simulation studies. In simulation studies, true parameter values are

known exactly, whereas in physical studies the gold standard values (here taken from the registered CT scan) can also include error, and this may partly account for the moderately greater alignment errors observed in the physical alignment tests.

The estimation of seven alignment parameters shown in Figure 33 could be used to compare the present line-source method with the method[56] which uses three point sources. The seven parameters (x_{det}, z_{det}, y_{det}, Φ, Ψ, u_f and v_f) estimated for Figure 33 here span a comparable parameter space to that considered by method[13]. However, multiple projection views are used in reference[13], whereas only one projection view is used here.

For onboard SPECT imaging in radiation therapy, alignment calibration would be done with the line-source phantom on the table – without the patient on the table – either before or after treatment. Once a trajectory is established, many robots can reproduce that trajectory with excellent precision. For example, the robot utilized in the alignment study here provides reproducibility to within a few tenths of a mm. Hence, the calibration – obtained during one execution of a trajectory – will be valid for the patient-imaging execution of the trajectory. For a multi-pinhole system, the relative alignment of individual pinholes may vary slightly with the angle of the overall system because the relative effects of gravity may vary. The proposed alignment method, as developed and evaluated here, utilizes a single pinhole projection and line sources. Consequently, it could be utilized to determine the relative alignment of individual

pinholes at each different angle of the overall system, and therefore it may beneficial to perform the alignment procedure at each stop of the imaging trajectory is to be used for the patient.

The calibration procedure would begin with the SPECT system retracted away from the radiation therapy gantry and table. The line-source phantom – on the table – would be scanned by CBCT to determine its alignment in the CBCT and LINAC coordinate frames. The CBCT detector and x-ray tube would then be retracted, and the robot would maneuver the multi-pinhole SPECT system about the phantom for calibration. Finally, the robot would retract the SPECT system away from the LINAC and patient table, the line-source phantom would be removed, and the table would be available for patient positioning followed by CBCT and SPECT imaging of the patient and radiation therapy.

Currently cone-beam CT imaging is widely employed onboard radiation therapy machines, in order to image patients as they are in position for radiation therapy. Studies have shown that radiation therapy treatment planning based on functional and molecular information about the tumor and surrounding tissue has potential to enhance the benefit of radiation therapy[1]. SPECT is a candidate for providing functional and molecular information, including onboard radiation therapy machines. For this, high quality and fast SPECT imaging is essential. A multi-pinhole SPECT system could provide the sensitivity and resolution needed for high-quality and fast imaging of

regions of interest. The alignment method developed in this paper could enable

registration of the SPECT coordinate frame with that of the cone-beam CT and LINAC,

and it has potential to improve SPECT image reconstruction by measuring angle-

dependent changes in relative pose among the multiple pinholes.

5.5 Conclusions

Estimation of alignment parameters can be achieved by using one pinhole

projection of line sources. Alignment errors are largely associated with limited accuracy

of the Radon transform in determining angles (α) and offsets (ϱ) of line-source

projections. This alignment method may be important for multi-pinhole SPECT, where

relative pinhole alignment can vary during rotation. For pinhole and multi-pinhole

SPECT imaging on-board radiation therapy machines, the method could provide

alignment of SPECT coordinates with those of CBCT and the LINAC.

6. Breast Imaging with a Robotic Multi-pinhole SPECT System

6.1 Introduction

Breast cancer is the most frequently diagnosed cancer, and the leading cause of cancer death, in women worldwide[69]. Radiation therapy is an effective and integral component of treatment for breast cancer[70, 71]. Irradiation of the whole-breast after breast conserving surgery is the current standard of care to control local recurrence[72-74]. To reduce the dose to normal tissue and shorten the treatment time, accelerated partial breast irradiation (PBI) has been developed, and studies have suggested comparable efficacy to whole breast irradiation[75-80]. However, there are major concerns with post-operative PBI using external beam radiation therapy, including poor cosmetic results and fibrosis[74, 81-84]. These suboptimal clinical outcomes are highly associated with the still relatively large volumes irradiated in post-operative PBI[75, 85, 86].

To reduce the treatment volume, *preoperative* radiation therapy has recently been investigated[74, 75, 87]. It has been shown that preoperative PBI reduces dose to ipsilateral breast tissue compared to postoperative PBI[75], and in several studies treatments volumes

were observed to be smaller with pre-operative radiation therapy as compared to postoperative radiation therapy[74, 75, 88].

With preoperative PBI providing treatment volumes much smaller than whole breast irradiation[74, 75, 88], target localization is important for effective radiation therapy. Also with preoperative PBI, the tumor is still present during radiation therapy and may be visible in nuclear medicine imaging, including Single Photon Emission Computed Tomography (SPECT). Tc-99m sestamibi and Tc-99m tetrofosmin have been used for over a decade in SPECT breast imaging[4-6, 89]. More recently, SPECT radiotracers targeting HER2 and estrogen receptor (ER) have been investigated for breast cancer imaging[89].

PBI can be performed with the patient in prone position and supine position. The growing interest in prone positioning of patients stems from multiple potential advantages, including more favorable breast shape for large breasted women and less breast motion[90-92]. Prone positioning in combine with PBI can potentially reduce dose to normal lung and cardiac tissue, which can help minimize the risk for late morbidities, as compared to supine-position irradiation[93-96]. For preoperative PBI, patients have been mostly treated in prone position[97]. Particularly given the deformability of a prone-dependent breast, onboard imaging, potentially SPECT, could be highly beneficial in localizing the radiation therapy treatment volume.

SPECT methods have been proposed specifically for imaging the breast in the prone position, including systems with parallel hole[98-102], rotating slant hole[103], and

pinhole or multi-pinhole collimation[104, 105]. Positron Emission Tomography (PET) has also been developed for prone breast imaging, for example the Mammi-PEM (Oncovision, Valencia, Spain)[106]. Relative to these methods, the 49-pinhole SPECT system[27] proposed here is intended to image many anatomical locations, in various patient orientations, not just the breast in the prone position or cardiac imaging. Also, these earlier prone-breast SPECT systems did not enable imaging with the patient in position at a radiation therapy machine. In the present system a robot is considered for this task[27]. Finally, these specialized breast imaging systems have not been investigated in conjunction patient tables used for prone breast radiation therapy.

The system considered here concentrates detector surface area and many (49) pinholes on a moderately sized ROI, potentially providing the sensitivity needed for fast (4-minute) imaging immediately prior to radiation therapy treatment. ROI SPECT systems have also been developed for cardiac imaging[17, 20, 107, 108]. Many of these cardiac systems use multi-pinhole configurations, and multi-pinhole SPECT systems have also been designed for small animal imaging[21-23]. Specifically, D-SPECT detector with 9 parallel-hole collimator in a curved configuration was developed for cardiac imaging with 4 or 2 minutes scan time[109]. Discovery NM 530c[20], a 19-pinhole cardiac SPECT system, was developed by GE Healthcare (Waukesha, WI). It has been proposed that some of these systems may be able to image cites other than the myocardium, including the breast.

In this study, the clinical feasibility of on-board SPECT imaging using a robotic

multi-pinhole system is investigated via phantom simulation for breast cancer patients

treated with radiotherapy in the prone position. Given that imaging performance of the

49-pinhole system depends in part on proximity of the pinholes to the ROI, the effect of

different thickness prone breast boards is investigated. Reconstructed 49-pinhole and

conventional parallel-hole SPECT images were evaluated by visual inspection, profiles,

noise-versus-bias curves, and hot sphere localization studies.

6.2 Methods and Materials

6.2.1 Phantom

Two female 3-D extended Cardiac-Torso (XCAT) phantoms[110] in prone position

were generated with a pre-determined distribution of attenuation coefficients and

radioactivity concentration, as shown in Figure 34(a) and (b), respectively. These

phantoms were simulated on a 256x256x256 matrix with voxel size of 0.2 cm. Nine hot

spheres each with 10 mm diameter were added in the left breast of the activity phantom,

as shown in Figure 34(b). These nine spheres were positioned spanning the entire breast,

to investigate the imaging feasibility of different lesion locations. The Tc-99m tracer

activity concentration in the hot sphere was 2 μCi/ml. The activity concentration ratio of

heart, hot sphere and background were 12:6:1, as shown in Figure 34(b).
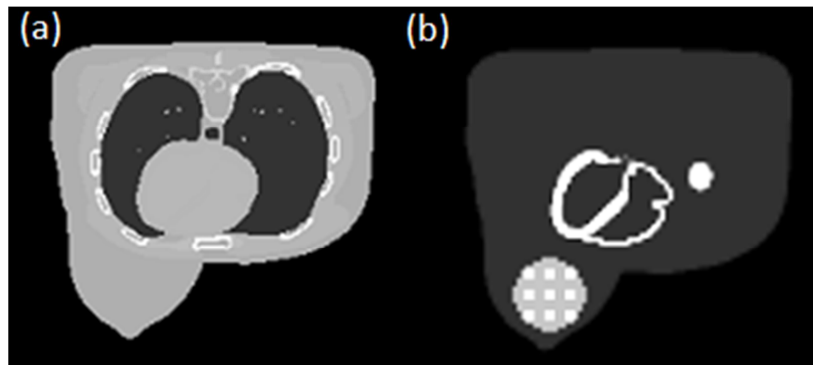
Figure 34: Female XCAT (a) attenuation phantom. (b) Activity phantom with a 7 cm-diameter sphere shown in grey defined as the ROI to encompass nine tumors.

Two prone breast boards were simulated: the CDR (thicker board) prone breast patient positioning (CDR Systems INC., Alberta, Canada) and the Varian kVue™ (thinner board) Access 360™ insert couch top (Varian Medical Systems, Inc., Palo Alto, CA), as shown in Figure 35. The thickness of these two prone breast boards is 24 cm and 7 cm, respectively. The LINAC treatment table was also simulated and added to the attenuation phantom. The table has a linear coefficient of 0.250 cm^{-1} at 140 keV, which corresponds to a predominately carbon-based material with physical density of 1.8 g/cm^3.[111] The table has a length of 53 cm and a thickness of 8 cm. The treatment table was simulated with a hollow core and an effective thickness of 0.8 cm. A reference simulation with no treatment table was also performed to determine the best achievable images.
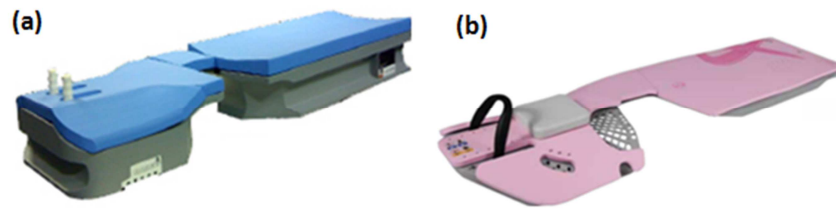
Figure 35: (a) CDR (thicker board) prone breast patient positioning board (CDR Systems INC., Alberta, Canada). (b) Varian kVue™ (thinner board) Access 360™ insert couch top prone breast board (Varian Medical Systems, Inc., Palo Alto, CA).

6.2.2 Multi-Pinhole System, Imaging Trajectories and Image Reconstruction

The simulated 49-pinhole SPECT system involves a central pod and six peripheral pods of seven pinholes each[27]. All pinholes were positioned to cover the same target volume. The detector for each pinhole has an active detector diameter of 7 cm and 3 mm inactive outer rim. The pixel width of the detector is 3 mm. The simulation modeled a tungsten pinhole with 4 mm pinhole diameter. Pinhole septal penetration was simulated.

Four different pinhole focal lengths of 15 cm, 18 cm, 21 cm and 24 cm were used for the thinner and thicker prone board to evaluate the effects of focal length on sensitivity of reconstructed image. The corresponding full pinhole opening angles are 26.3 degree, 22.0 degree, 18.9 degree and 16.6 degree, respectively. For the reference no table case, pinhole focal lengths of 9 cm, 12 cm, 15 cm and 18 cm were used.

A low energy medium resolution parallel-hole collimated detector with a surface area of 21.2x21.2 cm^2 was also computer-simulated as a reference. The hexagonal collimator hole has a length of 27 mm, diameter of 1.5 mm, and septal thickness of 0.2 mm.

For 49-pinhole and parallel-hole systems, photon non-uniform attenuation in the patient was simulated, but photon scatter was not. Spatially varying collimator resolution was simulated for both detector systems.

To simulate the imaging trajectories, a 0.8 cm support region and a 1.2 cm exclusion region were added to the attenuation phantom with the treatment table and the prone breast board. The detector was outside the exclusion region to avoid collision with the patient, the prone breast board and the table. The target region is an 8.24 cm-diameter sphere which encompasses all nine hot spheres, shown as the bright circle in Figure 1(b).

The trajectory of the 49-pinhole detector involves 12 detector stops with 49 views per stop. The central pinhole spans 158 degree. The central plane was enclosed in the convex hull of the pinhole trajectories. The trajectory of the parallel-hole collimated detector involves 60 detector stops over 180 degree. Figure 36 shows detector positions for the 49-pinhole and parallel-hole SPECT systems, for thicker and thinner prone breast boards.

The radius-of-rotations (RORs) for these trajectories were varied to avoid the collision of phantom and table, while keeping the 8.24 cm-diameter target region in the field-of-view (FOV) of the detector.

SPECT projection data were computer simulated for 49-pinhole and parallel-hole trajectories with 4-minute scans. Noisy Poisson-distributed projection data were drawn from these simulated projections. SPECT images were reconstructed by OSEM with 4 subsets and up to 10 iterations. The reconstructions modeled non-uniform attenuation in the phantom, but they did not model collimator spatial resolution.
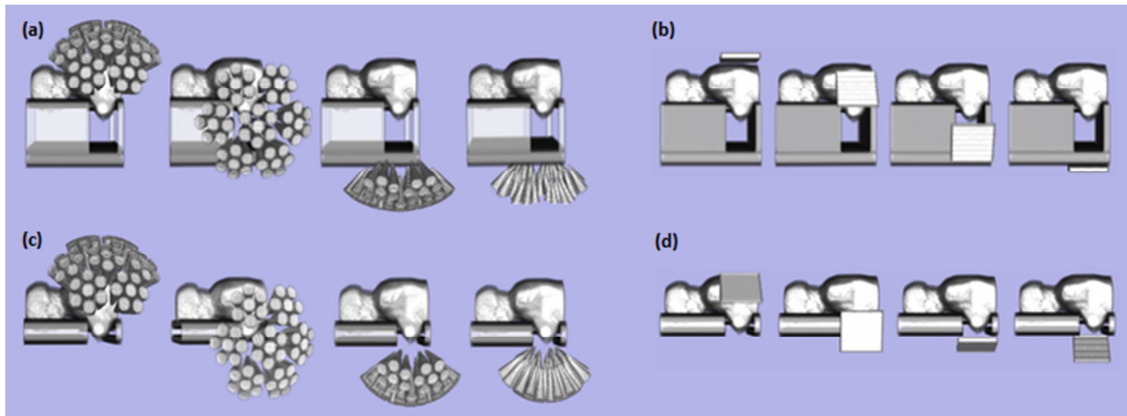
Figure 36: Trajectory of (a) 49-pinhole SPECT with thicker table, (b) parallel-hole SPECT with thicker table, (c) 49-pinhole SPECT with thinner table, (d) parallel-hole SPECT with thinner table. The 8.24 cm-diameter target region (bright sphere in the breast) is a common volume for the 49-pinhole trajectory and for the parallel-hole trajectory. Four of the twelve 49-pinhole detector stops and four of the 60 parallel-hole detector stops are shown here.

6.2.3 Image Analysis

The radius-of-rotation (ROR) for no-table case and two detector systems and two prone breast boards were plotted with projection angles, compared to the no-table reference case. The root-mean-square-error (RMSE) was calculated using equation

$$RMSE = \sqrt{MSE} = \sqrt{\sum_{i=1}^{i=No.of\ ROI\ voxels} \frac{(True_i - Estimated_i)^2}{No.of\ ROI\ voxels}} \qquad (27)$$

as a function of iterations for no-table case and two prone breast boards. The reconstructed phantom from 49-pinhole and from parallel-hole trajectories for each prone breast board were evaluated by visual inspection and profiles through the lesion. Twenty-five noisy Poisson-distributed projection data was generated as an ensemble, and used to generated 25 reconstructed images for two detector systems with no table and two prone boards. The bias and noise of the 25 ensembles were calculated as

$$Bias = \sqrt{\sum_{i=1}^{nvox} b_i^2} \qquad (28)$$

$$Noise = \sqrt{\sum_{i=1}^{nvox} \sigma_i^2} \qquad (29)$$

where $b_i = \mu_i{}^{avg} - \mu_i{}^{Phantom}$ and $\sigma_i = \sqrt{\frac{1}{25}\sum_{j=1}^{25}(\mu_i{}^j - \mu_i{}^{avg})^2}$. The $\mu_i{}^{Phantom}$ is the activity value at voxel i. The average activity value at voxel i is $\mu_i{}^{avg} = \frac{1}{25}\sum_{j=1}^{25}\mu_i{}^j$, where $\mu_i{}^j$ is the estimated activity at voxel i in the jth noisy realization of the image ensemble.

88

The hot sphere localization errors using 49-pinhole and parallel-hole SPECT

systems were investigated with 25 noisy realizations for no-table case and both prone

breast boards. The localization routine was based on a cross-correlation numerical

observer to detect the hot sphere position on the reconstructed image[112]. For each lesion,

the searching sphere of 2.4 cm diameter encompassed one and only one hot sphere. A

numerical observer searched the hot sphere centroid on the reconstructed image. The

localization errors were calculated as the Euclidean distance between a true hot sphere

centroid and a measured hot sphere centroid. The box-and-whisker plot was used to

study the localization errors from 49-pinhole and parallel-hole SPECT systems. The box-

and-whisker plot is implemented as follows: the length of the box represents the

interquartile range (IQR), the bottom end of the box is the 25% quartile (Q1), the

horizontal line inside the box is the median quartile (Q2), the top end of the box is the

75% quartile (Q3), the whiskers are on the last data point within 1.5IQR from the end of

the box. If there are no data points between the end of the box and 1.5IQR, the whisker is

placed at the end of the box. The square boxes outside the whiskers are outliers which

are the data points outside the 1.5IQR from either end of the box.

P-values from two-tailed Wilcoxon rank sum tests with 5% significance level

were calculated. The null hypotheses are that the underlying population distributions

are identical[113], and particularly for this study are: (i) localization errors of thinner board

from 49-pinhole detector have the same distributions as that of the parallel-hole system;

(ii) localization errors of thicker board from 49-pinhole detector have the same

distributions as that of the parallel-hole system; (iii) localization errors of 49-pinhole

detector using thinner board have the same distributions as that of the thicker board; (iv)

localization errors of parallel-hole detector using thinner board have the same

distributions as that of the thicker board.

6.3 Results

Figure 37 shows ROR versus detector angle of the 49-pinhole system with

different pinhole focal lengths for no-table case and two prone breast boards. The RORs

for no table are the smallest, and that of the thinner board are smaller than that of the
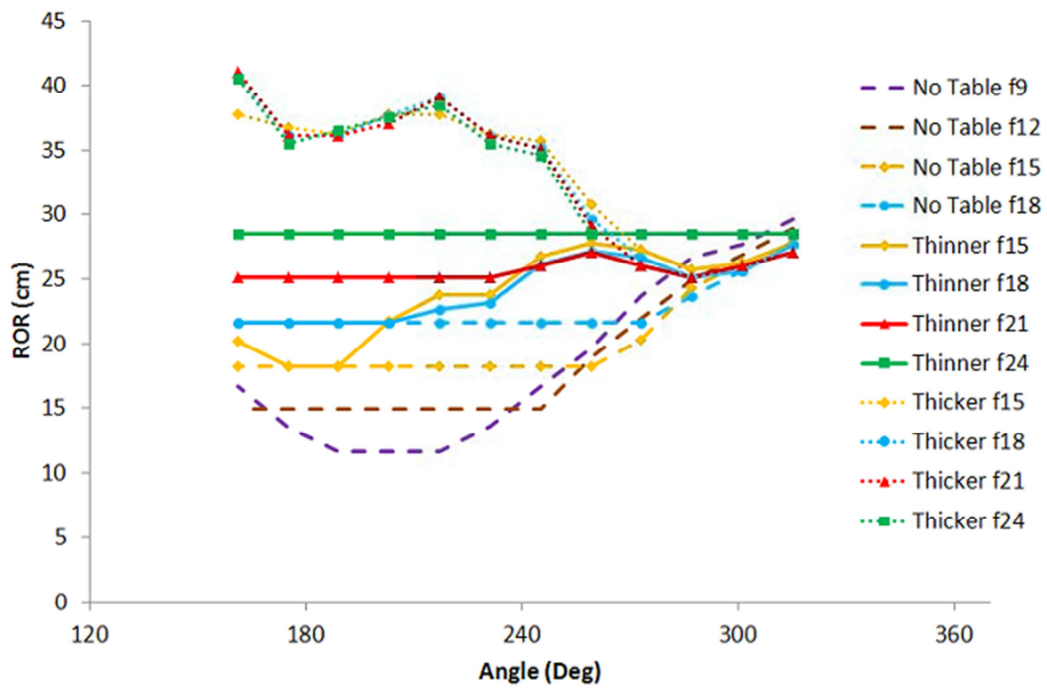
thicker board.

Figure 37: ROR versus angle of the 49-pinhole system with different pinhole focal lengths of 9, 12, 15 (diamond), 18 (circle), 21 (triangle) and 24 cm (square) for no table (dash line), thinner board (solid line) and thicker board (dotted line).

Figure 38 shows RMSE versus number of iterations of 49-pinhole detector with different pinhole focal lengths for no-table case and two prone boards. For each plot, the smallest RMSE among 10 iterations was recorded and plotted in Figure 39 for 49-pinhole system without table and with thinner board and thicker board. The pinhole focal length which results in the smallest RMSE for no table, thinner board and thicker board case is 12 cm, 18 cm and 21 cm, respectively.
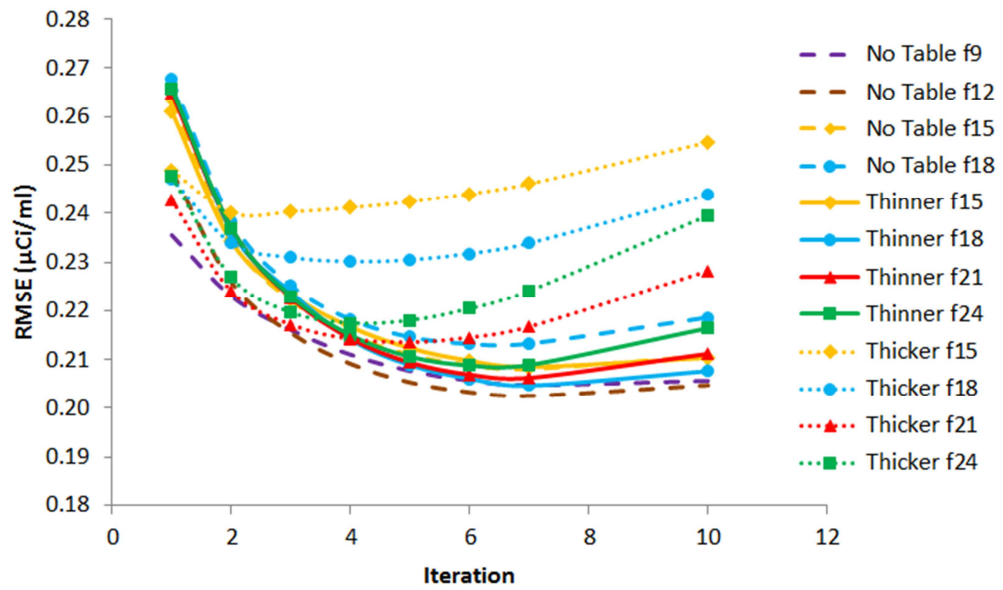
Figure 38: RMSE versus number of iterations of the 49-pinhole system with different pinhole focal lengths of 9, 12, 15 (diamond), 18 (circle), 21 (triangle) and 24 cm (square) for no table (dash line), thinner board (solid line) and thicker board (dotted line).
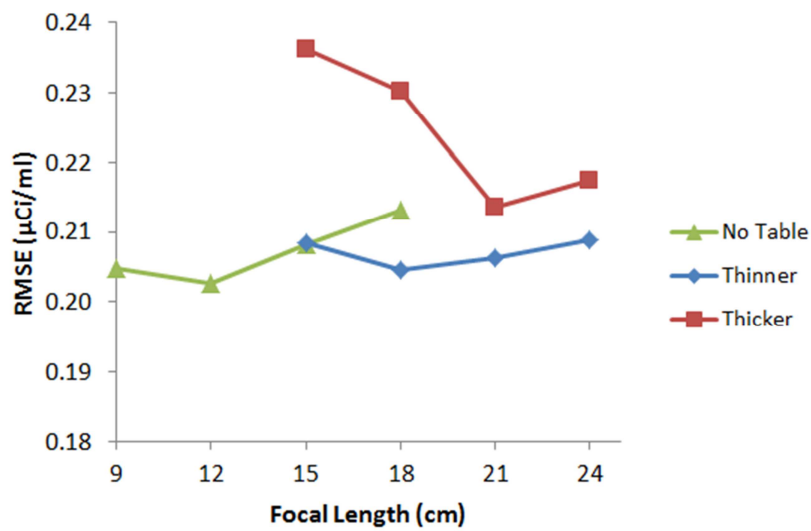
Figure 39: Smallest RMSE among 10 iterations versus pinhole focal length for no table case, thinner board and thicker board.

Figure 40 shows transverse views and profiles for images reconstructed from 49-pinhole and parallel-hole collimated SPECT with a 4-minute scan for no-table case and two prone breast boards. In the reconstructed images from the 49-pinhole SPECT system, all nine hot spheres are visible with no table and thinner board, and seven of nine hot spheres are visible with the thicker board. However, the hot spheres are not visible in the reconstructed images from the parallel-hole SPECT with and without prone boards.
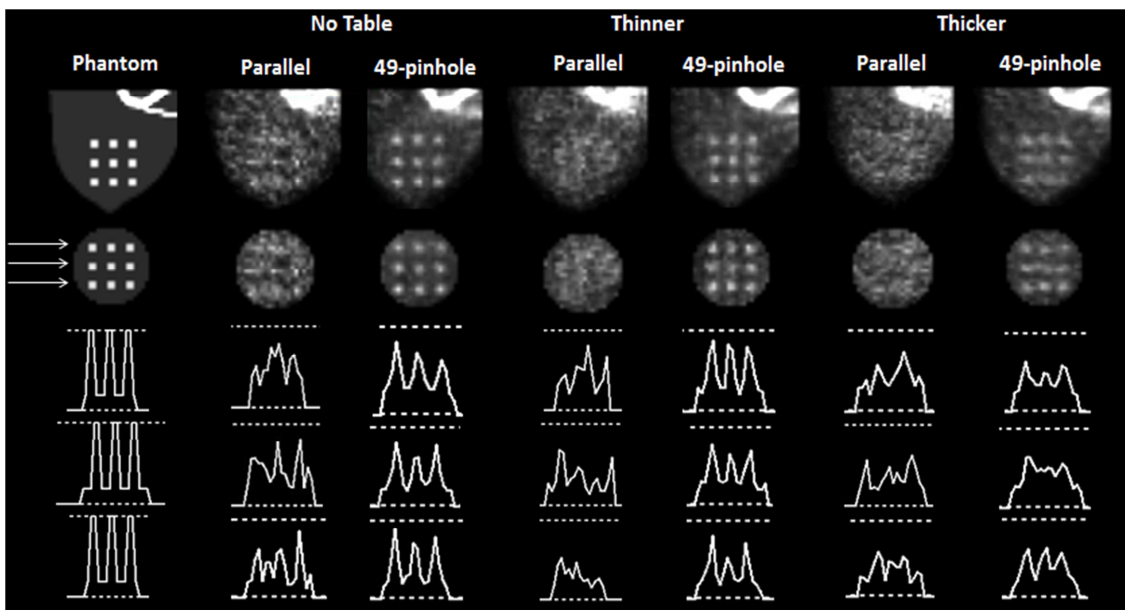
Figure 40: Images and profiles for the XCAT phantom slice with nine hot spheres in the breast (left column). Parallel-hole and 49-pinhole reconstructed image with no treatment table (second and third columns), thinner prone breast board (fourth and fifth columns) and thicker prone breast board (right two columns). The pinhole focal length is 12 cm, 18 cm and 21 cm for 49-pinhole system for no-table case, thinner and thicker board. The 8.24 cm-diameter ROI of the reconstructed image is shown as the second row. The plotted reconstructed images are at iteration number 10 and 4 of 49-pinhole system and parallel-hole system. Profiles are through the upper, middle, and lower rows of hot spheres, respectively, as indicated by the white arrows.

The ROR versus detector angles of 49-pinhole and parallel-hole system for no table, thinner board and thicker board was plotted in Figure 41. The RORs for no table case are smaller for both detector systems compared to that of using prone breast boards. Both detector systems have smaller RORs for the thinner board than the thicker board. For the same board, the 49-pinhole system has somewhat larger RORs than the parallel-hole system. The RORs for no table case are smaller for both detector systems compared to that of using prone breast boards.

Figure 42 shows the plot of noise versus bias of the 49-pinhole and parallel-hole system for no table, thinner and thicker board, across an ensemble of 25. The bias of the reconstructed image from no table and thinner board are smaller than that of the thicker table at a given noise. Increasing iteration number, the bias decreases and the noise increases. The noise and bias of the 49-pinhole system is generally less than that of the parallel-hole system at the same iteration number. The bias of the parallel-hole system is similar with different iteration number while the noise increases sharply with increasing iterations.
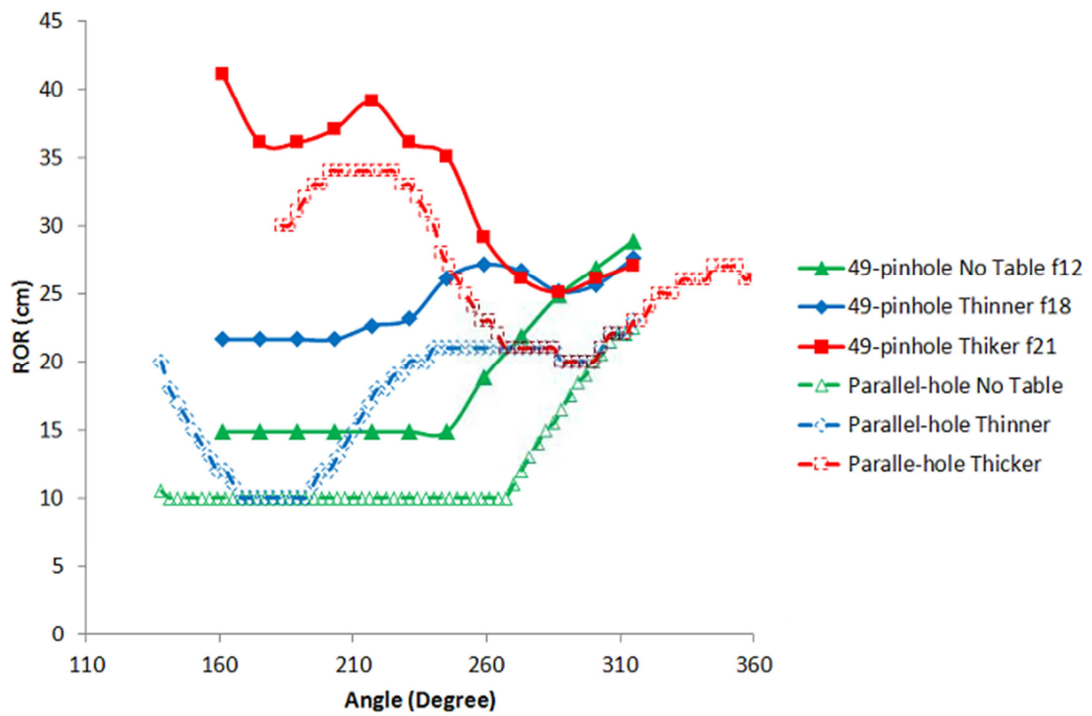
Figure 41: Plots of ROR versus angle of 49-pinhole system (solid line) and parallel-hole system (dashed line) for no table case with pinhole focal length of 12 cm (triangles), thinner prone board with pinhole focal length of 18 cm (diamonds) and thicker prone board with pinhole focal length of 21 cm (squares).
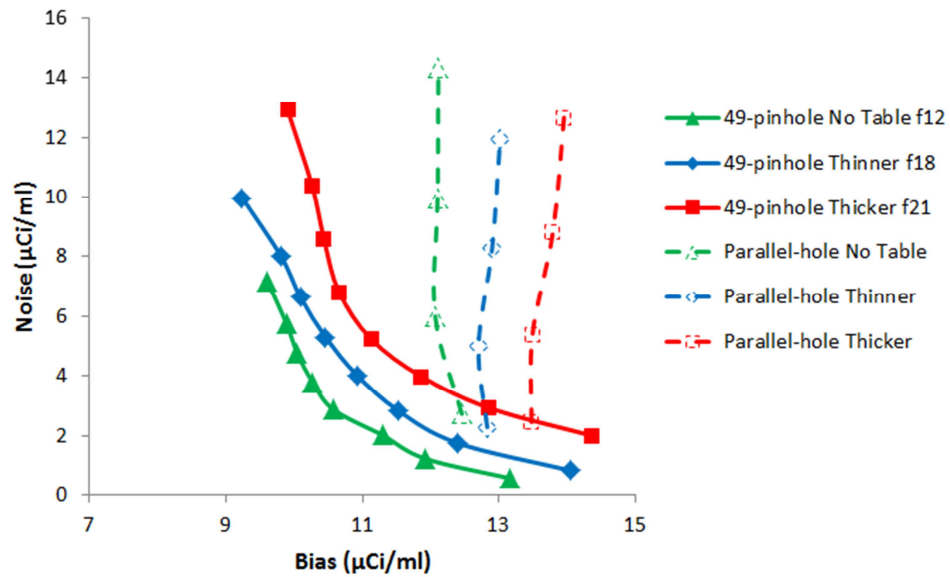
Figure 42: Plots of noise versus bias of 49-pinhole system (solid line) and parallel-hole system (dashed line) for no table case with pinhole focal length of 12 cm (triangles), thinner prone board with pinhole focal length of 18 cm (diamonds) and thicker prone board with pinhole focal length of 21 cm (squares). The iteration number increases from right to left from 1 to 7 and 10 for 49-pinhole system. The iteration number increases from bottom to top from 1 to 4 for parallel-hole system.

Figure 43 shows estimates of hot sphere position overlaid on the activity

phantom for no-table case, the thinner board and the thicker board for 49-pinhole (a, c

and e) and parallel-hole (b, d, f) detector system, respectively. There are 25 markers for

each hot sphere representing noisy ensembles. Localization is more accurate using the

49-pinhole than that of the parallel-hole systems. In addition, the no-table case has the

best localization accuracy than that of with the prone board for both systems. For the 49-

pinhole system, the thinner board has better localization accuracy than the thicker

board. However, for the parallel-hole, localization accuracy was not improved with the

thinner board. Figure 43 also indicates that the localization error depends on the hot

sphere location. For instance, for the superficial hot spheres which are located close to the lower left corner, the estimated markers are more tightly distributed at the true hot sphere location. In contrast, for the deeper hot spheres which are located at the upper right corner, the estimated markers are distributed more diffusely at the true hot sphere location.
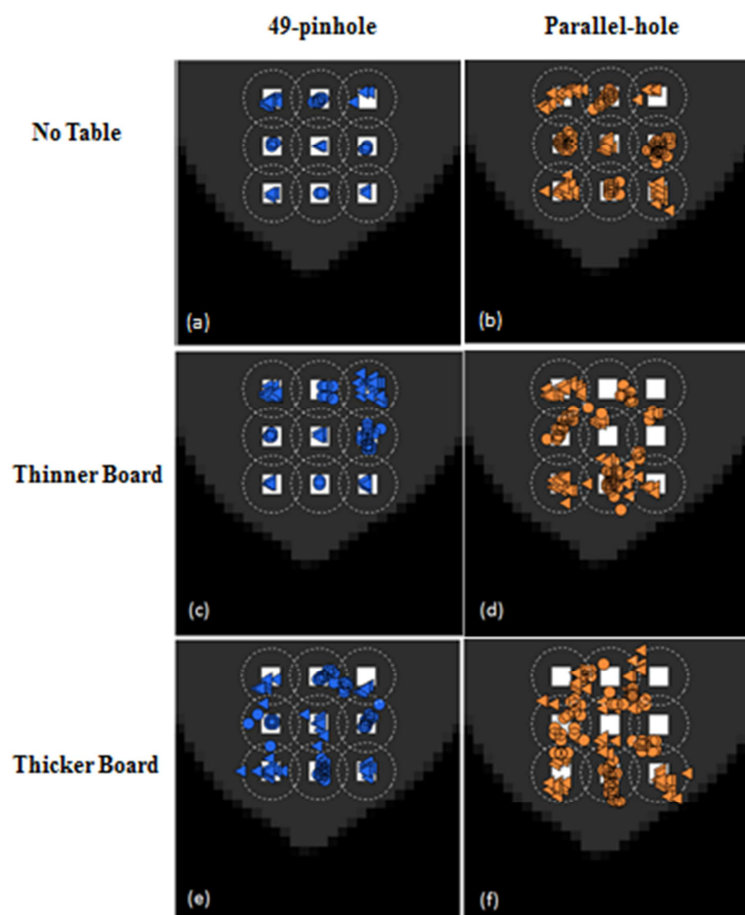
Figure 43: Estimated hot sphere positions from 25 image ensembles are plotted on the activity phantom. (a, c and e) No table, thinner board and thicker board using 49-pinhole system. (b, d and f) No table, thinner board and thicker board using parallel-hole system. The bright spots are true hot sphere positions, and the search

region boundaries are indicated by dotted white lines. Correct localizations are centered exactly in these circles.

Figure 44 shows the box-and-whisker plot of each hot sphere for the 49-pinhole and parallel-hole SPECT systems, for no table cases and two prone boards. For the no-table case, the median localization error of 6 hot spheres are within 2 mm for 49-pinhole system, while the median error of 5 hot spheres are within 4 mm for parallel-hole system. Using the 49-pinhole SPECT system with the thinner board, five of nine hot spheres (1, 2, 3, 5 and 6) were localized with the entire whisker within 3 mm, and with the thicker board, five of nine hot spheres (1-5) were localized with the median error within 4 mm. Using the parallel-hole SPECT system with the thinner board, two of the hot spheres (2 and 3) were localized with median error less than 3 mm, and with the thicker board, all nine hot spheres were localized with the median error greater than 4 mm.

P-values from two-tailed Wilcoxon rank sum tests with 5% significance level are shown in Table 11. Localization errors from the 49-pinhole system are statistically significantly less than those of the parallel-hole system using both thinner and thicker boards for all 9 hot spheres. For the 49-pinhole SPECT system, localization errors using the thinner board are statistically significantly less than those using the thicker board for 8 of 9 hot spheres. However, for the parallel-hole detector, only three hot spheres have statistically significantly lower errors in hot sphere localization using the thinner board versus the thicker board.

98
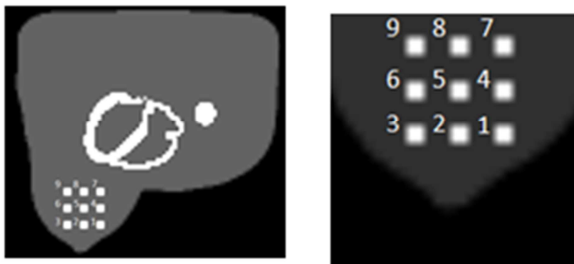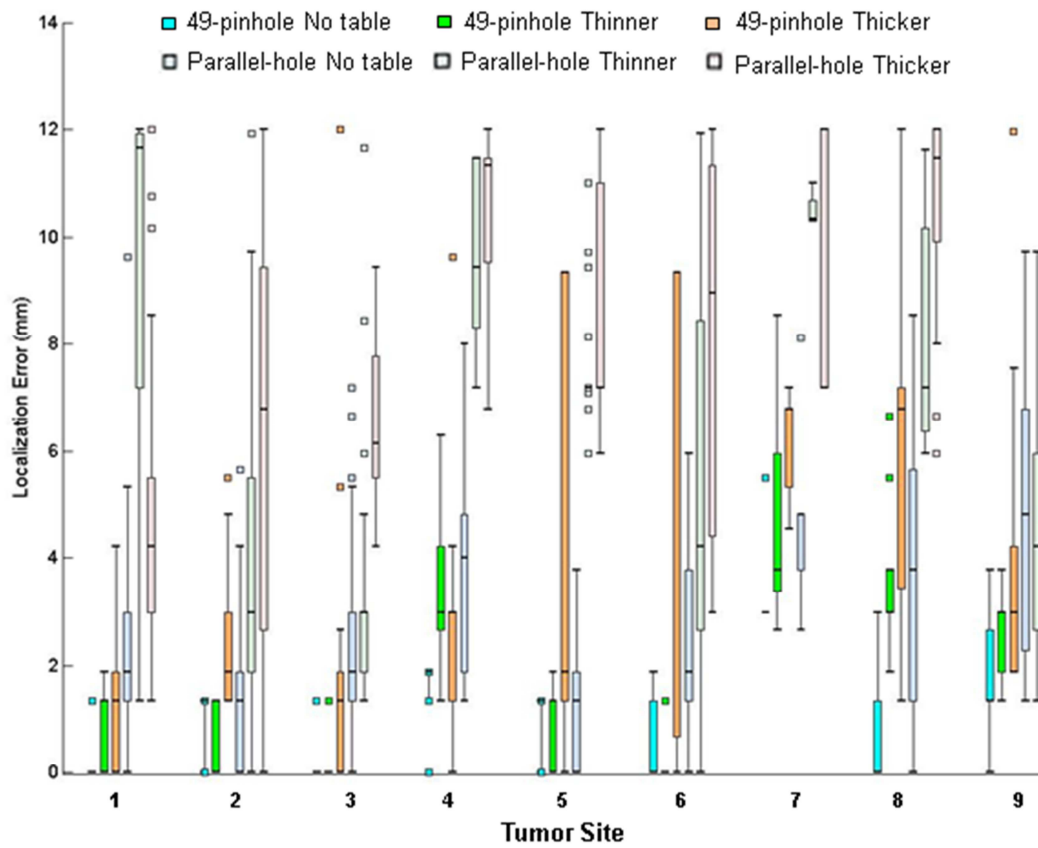
Figure 44: Box-and-whisker plots of hot-sphere localization errors. Hot sphere locations, specified by number along the horizontal axis, are indicated by the figures on the right. For each hot sphere, from left to right is 49-pinhole system with no table, thinner board and thicker board, and parallel-hole system with no table, thinner board and thicker board, respectively.

Table 12: P-values from two-tailed Wilcoxon rank sum test with 5% significance level. Numbers in bold are p<0.05.

Hot sphere Site	49-pinhole vs. Parallel-hole		Thinner vs. Thicker	
	Thinner	**Thicker**	**49-pinhole**	**Parallel-hole**
1	< 0.001	< 0.001	0.003	0.043
2	< 0.001	< 0.001	< 0.001	0.102
3	< 0.001	< 0.001	< 0.001	< 0.001
4	< 0.001	< 0.001	0.246	0.071
5	< 0.001	< 0.001	< 0.001	0.023
6	< 0.001	0.009	< 0.001	0.016
7	< 0.001	< 0.001	< 0.001	0.039
8	< 0.001	< 0.001	< 0.001	< 0.001
9	< 0.001	< 0.001	< 0.001	0.083

6.4 Discussion

Cone-beam CT imaging is a widely employed on-board radiation therapy machine, in order to image patients as they are in position for radiation therapy. Studies have shown that radiation therapy treatment planning based on functional and molecular information about the hot sphere and surrounding tissue has potential to enhance the benefit of radiation therapy[1], but currently there is no established method for functional and molecular imaging on-board therapy machines. SPECT has the potential to accomplish such imaging. Robotic multi-pinhole SPECT has been proposed[27, 43, 114]. Multiple pinholes could provide the photon-detection sensitivity needed for clinically acceptable scan times. The robot could enable imaging as the patient is in position for radiation therapy, and then retract the SPECT system away to provide clearance for radiation therapy.

The multi-pinhole robotic SPECT system is designed to image moderately sized ROIs. This is a good match for radiation therapy, where the approximate hot sphere target location is known by conventional methods such as skin marks. A key question is whether the system can image ROIs over the broad range of anatomical sites treated in radiation therapy. In Bowsher *et. al.*[27], the 49-pinhole system was evaluated for imaging the breast region of a supine patient. Radiation therapy of the breast may be performed with patients supine or prone, and these involve different ROI imaging geometries. With the patient prone, the breast is extended farther from the torso, which may facilitate SPECT detector proximity, but a breast board is involved, which hampers detector proximity. These factors are investigated here.

The work here is also relevant to SPECT breast imaging for diagnostic and treatment planning purposes. SPECT imaging of a pendulous breast, with the patient prone, has been an area of extensive investigation[98-105]. The present paper advances that effort.

The pinhole focal length affects the image quality. A larger focal length could be benefit for thicker board and a smaller focal length is preferred for closer proximity of the system to the target.

Herein, the 49-pinhole system is considered as the ROI SPECT imaging system, while the reference parallel-hole detector is considered as the broad cross-section imaging system. In addition, the parallel-hole detector is the most widely used detector

in clinics. As compared to a reference parallel-hole-collimated detector, the 49-pinhole system provided much better ROI image quality and hot-spot localization. Localization errors are statistically significantly less for the 49-pinhole system compared to the parallel-hole detector for both the thinner and thicker prone breast boards. The 49-pinhole system has more detector surface area than the parallel-hole collimated detector, and in contrast to the parallel-hole collimated detector, all of the detector surface area in the 49-pinhole system is concentrated on the ROI. Presumably these factors underlie the superior ROI-imaging performance of the 49-pinhole system.

Imaging capability, measured by localization and bias-versus-noise, were evaluated as a function of table thickness. Especially the no table case is used to study the limiting factors in improving image qualities. Without prone board and treatment table, hot sphere localization is more accurate and the noise and bias is smaller for both systems. In radiation application, prone boards are generally used for patient positioning. For thinner prone breast board, both 49-pinhole and parallel-hole systems have more accurate hot sphere localization and smaller noise and bias than the thicker board, as shown in Figure 42-Figure 44. The localization errors are statistically significantly less for 49-pinhole system, but not less error for parallel-hole system (Table 11, 49-pinhole thinner vs. 49-pinhole thicker and Parallel-hole thinner vs. Parallel-hole thicker).

102

The localization error depends on hot sphere location. For hot spheres that are located close to the outer breast region which is towards the anterior left lateral corner of the breast, for example hot sphere sites 1, 2, 3, 5, 6 and 9, localization errors are smaller than for hot spheres located away from the surface (Figure 44). For 49-pinhole system, the trajectory starts at the posterior-left-lateral portion of the phantom and rotates around the left breast, where the prone breast board opens, and then to the anterior-right of the breast (Figure 36(a) and (c)). The trajectory of parallel-hole detector covers the left lateral portion of the phantom (Figure 36(b) and (d)). These trajectories result in a better resolution and sensitivity of hot spheres that are in the anterior and left (lateral) portions of the breast.

In addition, the effects of intrafraction motion on image quality during the 4 minutes of SPECT imaging need to be considered. One study showed that the mean respiratory motion of the breast was 1.3 mm during the prone breast treatment time of 10 to 15 minutes[115]. The 1.3 mm motion is relatively small compared to 20 mm to 40 mm of respiratory lung motion range as studied in Chapter 7. The average localization error for the 20 mm tumor with 40 mm diaphragm motion is 0.5 mm. Therefore the effect of the 1.3 mm motion of the prone breast on localization accuracy may be comparable motion of the prone breast on the localization accuracy may be comparable to the localization uncertainties of 49-pinhole SPECT imaging.

6.5 Conclusions

This paper indicates that on-board robotic multi-pinhole imaging with 4 minutes scan time could provide visualization and localization of 10-mm-diameter hot spots throughout a pendulous breast. To optimize the reconstructed image quality, pinhole focal length is smaller for thinner board which allows closer proximity of the detector to the target, and focal length is larger for thicker board. Close proximity between the breast and the detector system, which is influenced by factors including breast-board design, is the key to image quality and localization accuracy. This robotic multi-pinhole system shows potential for on-board functional and molecular imaging.

7. Noise Reduction of Respiratory-gated Imaging Using Region-of-interest (ROI) Robotic Multi-Pinhole SPECT System

7.1 Introduction

Lung cancer is one of the most frequently diagnosed cancers and one of the leading cause of cancer death in both males and females, with 226,160 estimated new cases and 160,340 estimated deaths in US in 2012[116].

Single photon emission computed tomography (SPECT) has been established for nonsmall cell lung cancer (NSCLS) and SCLC staging[117]. For example, the Tc-99m labeled radiotracers sestamibi and tetrofosmin, and thallium-201, have been used widely in lung imaging[118-126]. Recently, radio labeled monoclonal antibodies labeled tracers have been also investigated for lung tumor nuclear medicine imaging[127, 128].

One of the challenges to image tumor is respiratory motion. Respiratory motion degrades SPECT image quality in the thorax and abdomen[3, 129-131], and causes registration error between SPECT and CT images for radiation therapy[132-135]. For transmission imaging modalities, different techniques, such as respiratory gating, breath hold and tumor tracking[136], have been developed to generate 4D images to reduce the motion

artifacts[136]. For emission imaging modalities, such as positron emission tomography (PET) and SPECT, breath hold can be challenging because the general imaging time is about 20 minutes. Therefore, respiratory-gated techniques could be an alternative to reduce tumor motion blur[2]. Respiratory-gated methods have been used for myocardial SPECT imaging[9, 137-140] and pulmonary perfusion and ventilation SPECT imaging[141-144]. For tumor imaging, respiratory-gating has been widely used for PET[2, 145]. Recently, this technique has been adapted to detect pulmonary malignant tumors using SPECT[146].

However, although the gating technique reduces motion blur by imaging within a portion of the respiratory cycle, the detected number of photons in each gate decreases which may result in a noisier image. Furthermore, the respiratory-gated technique is generally performed using a broad cross-section SPECT system with parallel-hole collimation. The broad cross-section method images a large portion of the thorax, which requires long imaging times varying from 12 min to 29 min[146] and results in noisy images. To address these concerns, a region-of-interest (ROI) SPECT imaging system with 49-pinhole collimation[27, 147], as shown schematically in Figure 45, has been developed. This system concentrates SPECT imaging capability on a ROI which contains the moving tumor. This imaging technique provides higher sensitivity to the ROI, which can reduce the imaging time to 4 minutes and alleviate the noise effects.
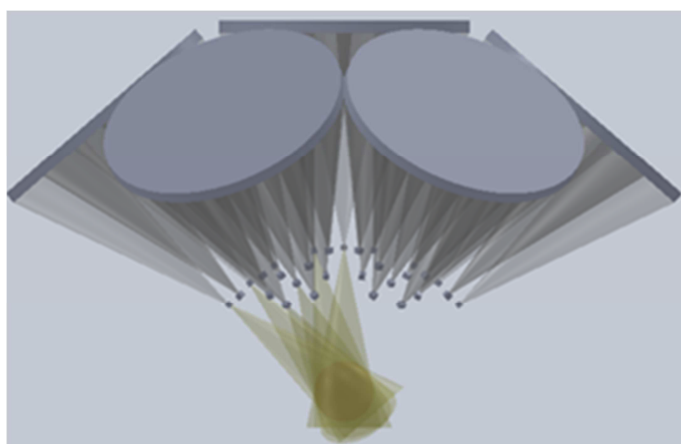
Figure 45: ROI SPECT imaging system with 49-pinhole collimator. All 49 pinholes focus on the same ROI (target region) as represented by the sphere.

Another motivation for developing this ROI SPECT imaging system is on-board imaging. In radiation therapy, on-board image guidance such as cone-beam CT (CBCT) and two-dimensional kV/MV imaging is essential for target localization. These imaging tools enable high dose to be delivered precisely to the target with less injury of surrounding normal tissues in order to maximize tumor local control and to minimize normal tissue complication. These imaging techniques provide predominantly anatomical information for treatment planning and target localization. Recently, studies have shown that functional and molecular properties could more strongly differentiate tumors from nearby healthy tissues and may be more directly related to necessary dose, such that functional and molecular imaging has potential to enhance the benefit of radiation therapy[1]. SPECT has been well known for its functional and molecular information, however, the lack of anatomical information is a limitation of SPECT imaging. SPECT/CT fusion has been employed for functional anatomical imaging of

lung cancer[133, 148, 149]. However, these applications are currently only used for diagnosis and treatment assessment. There is no SPECT system that has been implemented for on-board imaging.

Therefore, the proposed ROI SPECT imaging system can be attached to a robotic arm which maneuvers the detector to accomplish on-board functional and molecular imaging[27, 114]. This ROI imaging region could be, in this case, the radiation therapy target. The ROI imaging improves the SPECT sensitivity of the target region, therefore enabling a scan time of 4 minutes for the on-board imaging capability. The robotic arm images the patient in position for radiation therapy, and then retracts the SPECT system away to provide clearance for radiation therapy.

The purpose of this study is to investigate the feasibility of on-board respiratory-gated ROI SPECT imaging of lung tumor using a multi-pinhole system through a phantom simulation. The effectiveness of respiratory-gated ROI imaging to reduce the noise was studied as compared to the broad cross-section imaging. Reconstructed respiratory-gated images from ROI imaging system and broad cross-section imaging system were evaluated by visual inspection, profiles, and noise versus bias. Tumor localization was evaluated with a forced-choice numerical observer.

7.2 Materials and Method

7.2.1 Phantoms and Respiratory-gating

The 4-D extended Cardiac-Torso (XCAT) phantom[110] was used to simulate the

respiratory gating scenario. For each of two motion models, thirty phantom sets were

generated in one respiratory cycle of 5 sec (Figure 46). Each set included two phantoms:

an attenuation phantom and an activity phantom. For each of the two motion models,

one of the thirty activity phantoms is shown in Figure 47. For the two motion models,

respectively, a 10 mm or a 20 mm diameter tumor was added in the right lung with the

same respiratory motion pattern as the diaphragm. The two motion models involved

diaphragm motion of 2 cm and 4 cm in the superior-inferior direction for the 10 mm and

the 20 mm tumor, respectively. For both motion models, the anterior-posterior

diaphragm motion was 1.2 cm.

These 30 phantom sets were divided into 6 gates of 5 sets each and then summed

within each gate (Figure 46), thus simulating motion blur within each gate. Therefore,

each gate has one blurred activity phantom and one blurred attenuation phantom. The

phantoms were simulated on a 256x256x256 matrix with a voxel size of 0.2 cm. The Tc-

99m tracer activity concentration in the tumor, heart and lung/background were 1.5

μCi/ml, 5 μCi/ml and 0.25 μCi/ml, respectively.
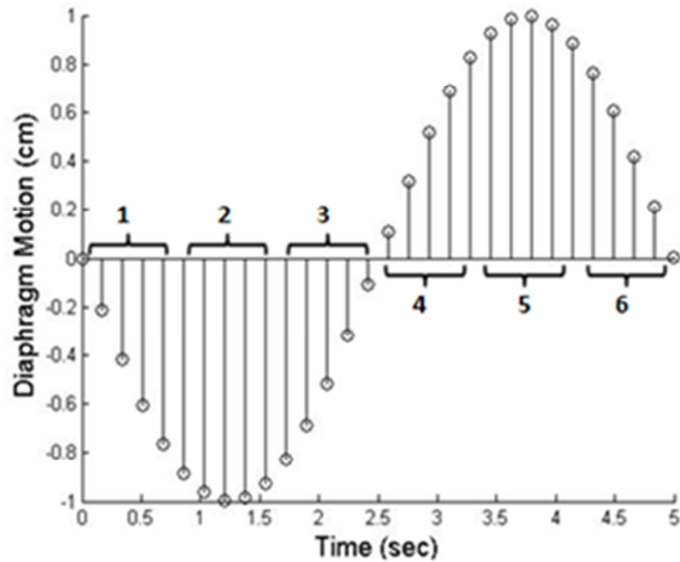
Figure 46: Respiratory cycle of 5 sec and diaphragm motion of 2 cm in superior-inferior direction. Thirty 3D phantom sets were generated equally distributed within one respiratory cycle. These 30 phantom sets were divided to 6 groups and summed to simulate 6 respiratory gates.
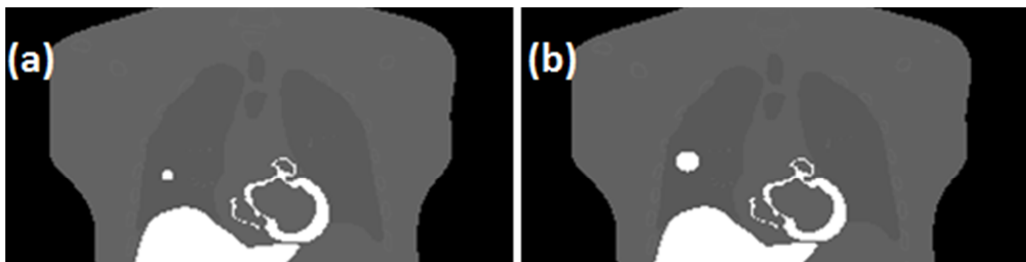
Figure 47: One of the 30 activity phantoms for (a) 10 mm diameter tumor with 2 cm diaphragm motion in superior-inferior direction and (b) 20 mm diameter tumor with 4 cm diaphragm motion in superior-inferior direction.

7.2.2 SPECT Imaging Systems

The ROI SPECT imaging system has 49 pinholes[27] and involves a central detector pod and six peripheral detector pods, as shown in the large circles in Figure 48. Each detector pod has seven pinholes, each corresponding to an individual detector of 7 cm diameter. The pods and their pinholes are configured such that variation of a single angle, that between the central and peripheral pods, is sufficient to maintain the ROI fully within the FOV of all pinholes at and beyond a minimum pinhole-to-ROI distance27. The ROI is shown in Figure 49 and is a sphere 8.2-cm in diameter. Each tungsten pinhole was modeled with a 4 mm diameter, a 26.3-degree full opening angle and a 15 cm focal length. Pinhole septal penetration was simulated for modeling the sensitivity and resolution. The detector was modeled as pixelated with a 3 mm pixel pitch.
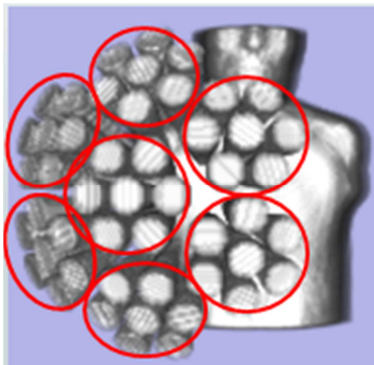
Figure 48: ROI imaging system with 49 pinholes. The system has one central detector pod and six peripheral pods, indicated by the large circles. Each pod has seven detectors. Each individual detector is 7 cm diameter large and corresponds to one pinhole.
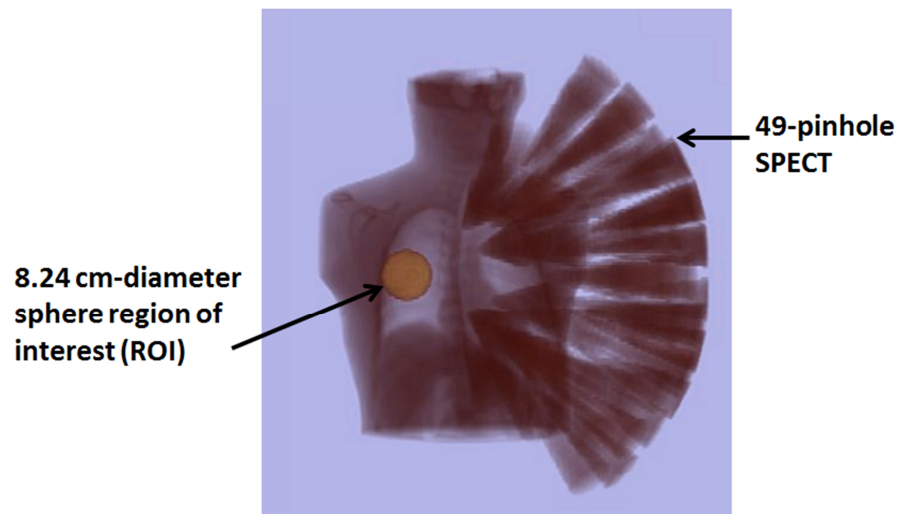
Figure 49: An 8.2-cm-diameter ROI was set to encompass the tumor and its motion range. All 49 pinholes fully view this target region.

Reference broad cross-section imaging systems were simulated as pixelated detectors with parallel-hole collimation. Detector pixel pitch was 3 mm, and detector surface area was 21.2x21.2 cm². The hexagonal collimator holes had a length of 27 mm and a flat-to-flat diameter of 1.5 mm, with a spetal thickness of 0.2 mm. A dual-head parallel-hole collimator was simulated by doubling the efficiency of the single-head parallel-hole collimator.

7.2.3 Imaging Trajectories

To determine the imaging trajectories, an exclusion region was formed as a 2.0-cm dilation of the attenuation phantom and the table. At each stop, detectors were positioned as close to the ROI as possible without entering exclusion region, except that

for the 49-pinhole system, it was also required that the pinholes be no closer to the ROI

than the minimum distance at which the ROI is fully viewed by all pinholes [27].

The trajectory of the ROI imaging system involved 12 detector stops with 49

views per stop. The central pinhole spanned 158 deg. The central plane of the ROI was

enclosed in the convex hull given by the trajectories of pinholes near the central plane.

The trajectory of the broad cross-section imaging system involved 60 detector stops over

180 deg. Figure 50 shows detector positions for the 49-pinhole ROI SPECT system and

the broad cross-section (single-headed parallel-hole) SPECT system. The trajectories

were same for all respiratory gates.
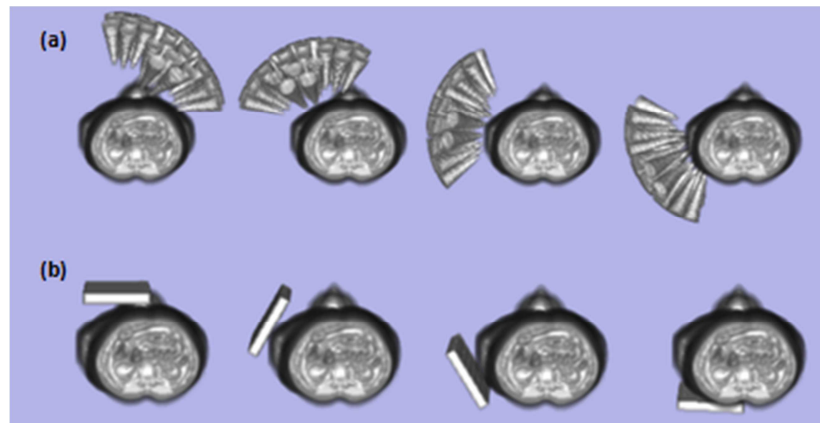
Figure 50: Trajectory of (a) ROI imaging system with 49 pinholes and (b) broad cross-section imaging system with a single-headed parallel-hole detector. Four of the twelve 49-pinhole detector stops and four of the 60 parallel-hole detector stops are shown here.

7.2.4 Projection Data, Image Reconstruction and Analysis

For each of the two motion models, ROI 49-pinhole and broad cross-section parallel-hole projection data were analytically simulated for each gate. The simulations included non-uniform attenuation in the patient and spatially varying collimator spatial resolution. The simulations did not include scatter in the patient. Image acquisition times for both the ROI and the broad cross-section systems were 4 minutes, i.e. 40 seconds per gate. For each gate of each motion model, an ensemble of 25 noisy projection data sets was generated by drawing from Poisson distributions with means given by the analytic simulations. Ensembles of 25 SPECT images were reconstructed, for each gate of each motion model, at each iteration of 4-subset OSEM, up to 3 iterations for parallel-hole imaging and 6 iterations for pinhole imaging.

Reconstructed images from the ROI and the broad cross-section imaging systems were evaluated by visual inspection and by profiles through the lesions in each respiratory gate. For each gate of both motion models, and as a function of OSEM iteration number, bias and noise were calculated from the 25 noisy images as

$$Bias = \sqrt{\sum_{i=1}^{nvox} b_i^2} \tag{30}$$

$$Noise = \sqrt{\sum_{i=1}^{nvox} \sigma_i^2} \tag{31}$$

114

where $b_i = \mu_i{}^{avg} - \mu_i{}^{Phantom}$ and $\sigma_i = \sqrt{\frac{1}{25}\sum_{j=1}^{25}(\mu_i{}^j - \mu_i{}^{avg})^2}$. The $\mu_i{}^{Phantom}$ is the true

activity value at voxel i. The average activity value at voxel i is $\mu_i{}^{avg} = \frac{1}{25}\sum_{j=1}^{25}\mu_i{}^j$,

where $\mu_i{}^j$ is the estimated activity at voxel i in the jth noisy realization of the image

ensemble.

Tumor localization was also investigated with the 25-image ensembles, using a

forced-choice cross-correlation numerical observer[112]. For each lesion, a spherical search

region of 4 cm diameter encompassed the tumor, over which the numerical observer

searched the tumor centroid. Localization errors were calculated as the Euclidean

distance between true and estimated tumor centroids, and these errors were

summarized with a box-and-whisker plot. The box-and-whisker plot was implemented

as follows: the length of the box represents the interquartile range (IQR), the bottom end

of the box is the 25% percentile, the horizontal line inside the box is the median , the top

end of the box is the 75% percentile, the whiskers are on the last data point within

1.5IQR from the end of the box. If there are no data points between the end of the box

and 1.5IQR, the whisker is placed at the end of the box. The square boxes outside the

whiskers are outliers which are the data points outside the 1.5IQR from either end of the

box.

P-values from two-tailed Wilcoxon rank sum tests with 5% significance level

were calculated. The null hypotheses were that the underlying population distributions

are identical[113]. Specifically, the hypotheses were: Localization errors from the ROI

imaging system have the same distributions as those of the broad cross-section dual-head parallel-hole imaging system for (i) the 10 mm tumor and (ii) the 20 mm tumor. Localization errors from the 10 mm diameter tumor have the same distributions as those of the 20 mm diameter tumor for (iii) the ROI imaging system; (iv) the broad cross-section imaging system.

7.3 Sensitivity and Resolution Validation

In addition to the validation of SPECT-map in Chapter 4, the sensitivity and resolution were also validated by comparing the measured values to the theoretical prediction using the designed trajectories of the ROI and broad cross-section imaging systems for respiratory lung imaging.

A small point source of 0.448 cm^3 with activity concentration of $1 \frac{\mu Ci}{ml}$ was generated at the center of a 256x256x256 grid with 0.2 cm voxel size. The attenuation phantom was set to zero. For ROI imaging system, the pinhole radius-of-rotation was 19 cm with pinhole diameter of 4 mm. The efficiency of the detector was set to $\frac{1}{6}$. The forward projection was generated with acquisition time of 20 sec to a projection grid of 0.3 cm pixel width. The projected image was analyzed with software SPECTER (By Dr. Timothy Turkington, Duke University Medical Center) using ROI analysis and the measured count was 1.33.

The theoretical sensitivity for single pinhole collimator with 4 mm pinhole is given by

$$\frac{d^2}{16h^2} \times A_c \times V \times 37000\frac{Bq}{\mu Ci} \times Branching\ ratio$$

$$\times Acquisition\ time \times Detector\ efficiency$$

$$= \frac{0.4^2}{16 \times 19^2} \times 1 \times 0.448 \times 37000\frac{Bq}{\mu Ci} \times 0.89$$

$$\times 20 \times 0.17 = 1.38$$

(32)

The error between measured sensitivity from SPECT-map and that of calculated sensitivity is

$$\frac{1.38 - 1.33}{1.38} \times 100\% = 3.6\%$$

(33)

For hexagonal broad cross-section parallel-hole collimator with a K factor of 0.26, the distance between the holes was 0.122 cm and the effective length of the hole was 2.54 cm, and the septal thickness was 0.02 cm. The acquisition time was 4 sec. The measured sensitivity from SPECT-map was 1.12.

The theoretical sensitivity for parallel-hole collimator can be calculated as followed

$$K^2 \times \frac{d^2}{l_{eff}^2} \times \left(\frac{d}{d+t}\right)^2 \times A_c \times V \times 37000 \frac{Bq}{\mu Ci} \times Branching\ ratio$$

$$\times\ Acquisition\ time\ \times Detector\ efficiency$$

$$= 0.26^2 \times \frac{0.122^2}{2.54^2} \times \left(\frac{0.122}{0.122+0.02}\right)^2 \times 1$$

$$\times\ 0.448 \times 37000 \frac{Bq}{\mu Ci} \times 0.89 \times 4 \times 0.17 = 1.15 \tag{34}$$

The error between measured sensitivity from SPECT-map and calculated value is

$$\frac{1.15 - 1.12}{1.15} \times 100\% = 2.6\% \tag{35}$$

To validate the resolution, a 0.2 cm radius sphere with activity of $1\frac{\mu Ci}{ml}$ was

generated at the center of a 256x256x256 grid with 0.2 cm voxel size. The same

parameters of the pinhole collimator for the sensitivity test were used. The forward

projection data was generated to a grid of 0.1 cm pixel width. The measured full width

at half maximum (FWHM) of the projection structure was 0.64cm measured from

SPECTER. The theoretical resolution could be found by

$$\sqrt{d^2\left(1+\frac{1}{M}\right)^2 + R_i^2} = \sqrt{0.4^2\left(1+\frac{1}{15/19}\right)^2 + 0.1^2} = 0.91 \tag{36}$$

The error between measured resolution from SPECT-map and that of the

theoretical calculation is

$$\frac{0.91 - 0.64}{0.91} \times 100\% = 29.7\% \tag{37}$$

7.4 Results

Figure 51 shows transverse views and profiles for images of the 10 mm diameter tumor with 2 cm diaphragm motion and for the 20 mm diameter tumor with 4 cm diaphragm motion in every respiratory gate, using the ROI SPECT system and the broad cross-section single-head and dual-head parallel-hole SPECT systems, all with 4-minute scan times. In the reconstructed images for the ROI SPECT system, the 10 mm diameter tumors are visible in four of the six gates (1, 3, 5 and 6) and the 20 mm diameter tumors are visible in every gate. However, the 10 mm diameter tumors with 2 cm motion are not visible in the reconstructed images from the two broad cross-section SPECT systems. For the 20 mm diameter tumor with 4 cm motion, the tumors are nearly visible for dual-head parallel-hole SPECT imaging, but not for the single-head parallel-hole system. Profiles through the tumors show not only better tumor contrast recovery with the 49-pinhole ROI system, but also less noise compared to broad cross-section imaging system.

(a)

(b)
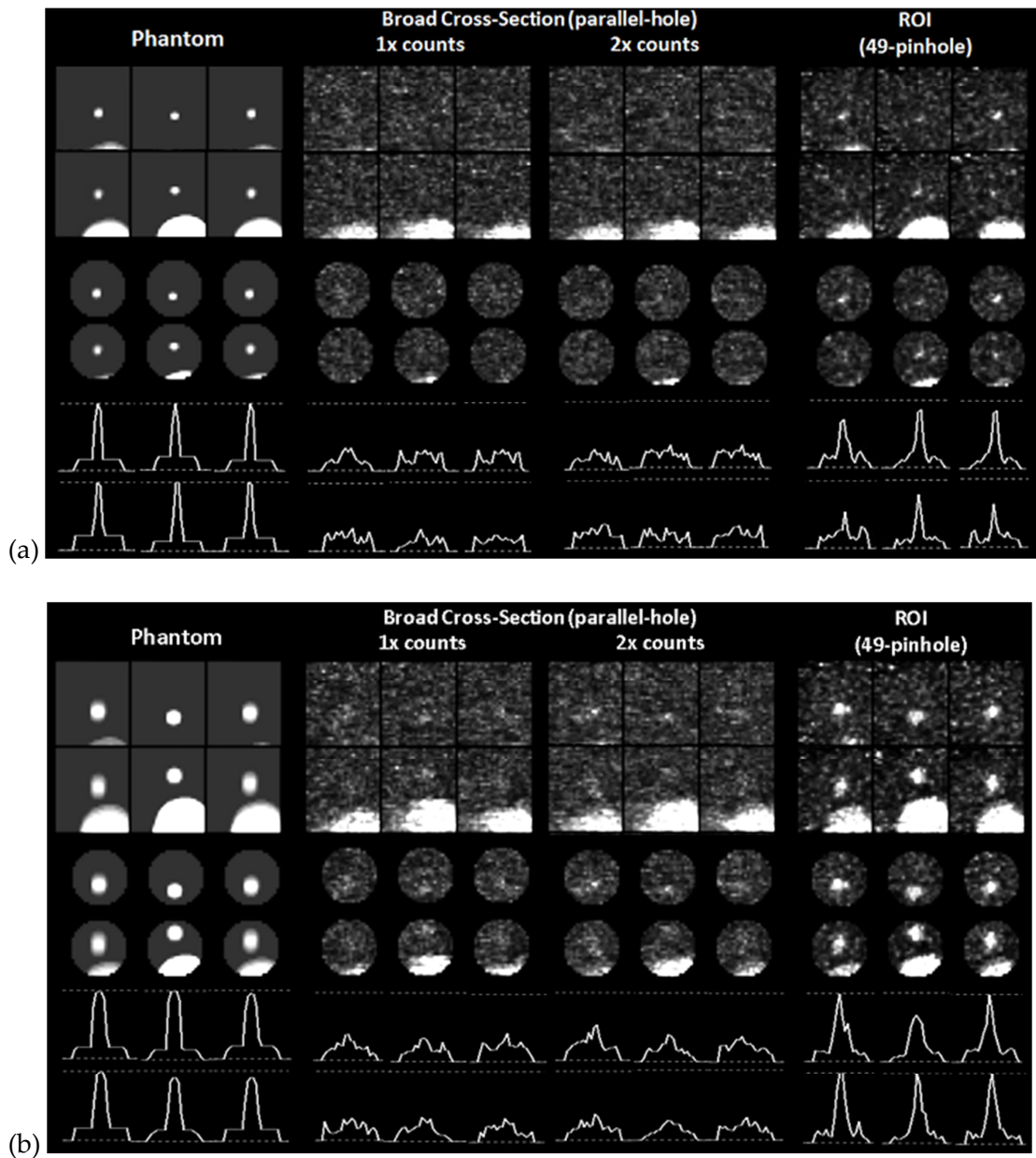
Figure 51: Images and profiles for the XCAT phantom (left panel) with (a) 10 mm diameter tumor with 2 cm diaphragm motion and (b) 20 mm diameter tumor with 4 cm diaphragm motion. Shown in rows 1 and 2 are reconstructed images in all 6 respiratory gates for broad cross-section imaging (middle two panels) and ROI imaging (right panel). The third and fourth rows show only the portion of the image that is within the 8.24-cm-diameter ROI that was the common volume of the 49-

pinhole trajectory. The profiles in rows 5-6 are through the tumor in each respiratory gate.

Figure 52 shows the plot of noise versus bias for the 49-pinhole ROI system and the dual-head and single-head parallel-hole systems, for the 10 mm diameter tumor with 2 cm diaphragm motion and the 20 mm diameter tumor with 4 cm diaphragm motion. At a given noise, the 49-pinhole ROI system shows lower bias than the broad cross-section, parallel-hole systems. Bias decreases and the noise increases with increasing iteration number. The noise and bias of the ROI system are generally less than that of the broad cross-section systems at the same iteration number. The bias of the dual-head parallel-hole system is smaller than that of the single-head parallel-hole system at a given noise. The noise and bias at each respiratory gate are somewhat different.
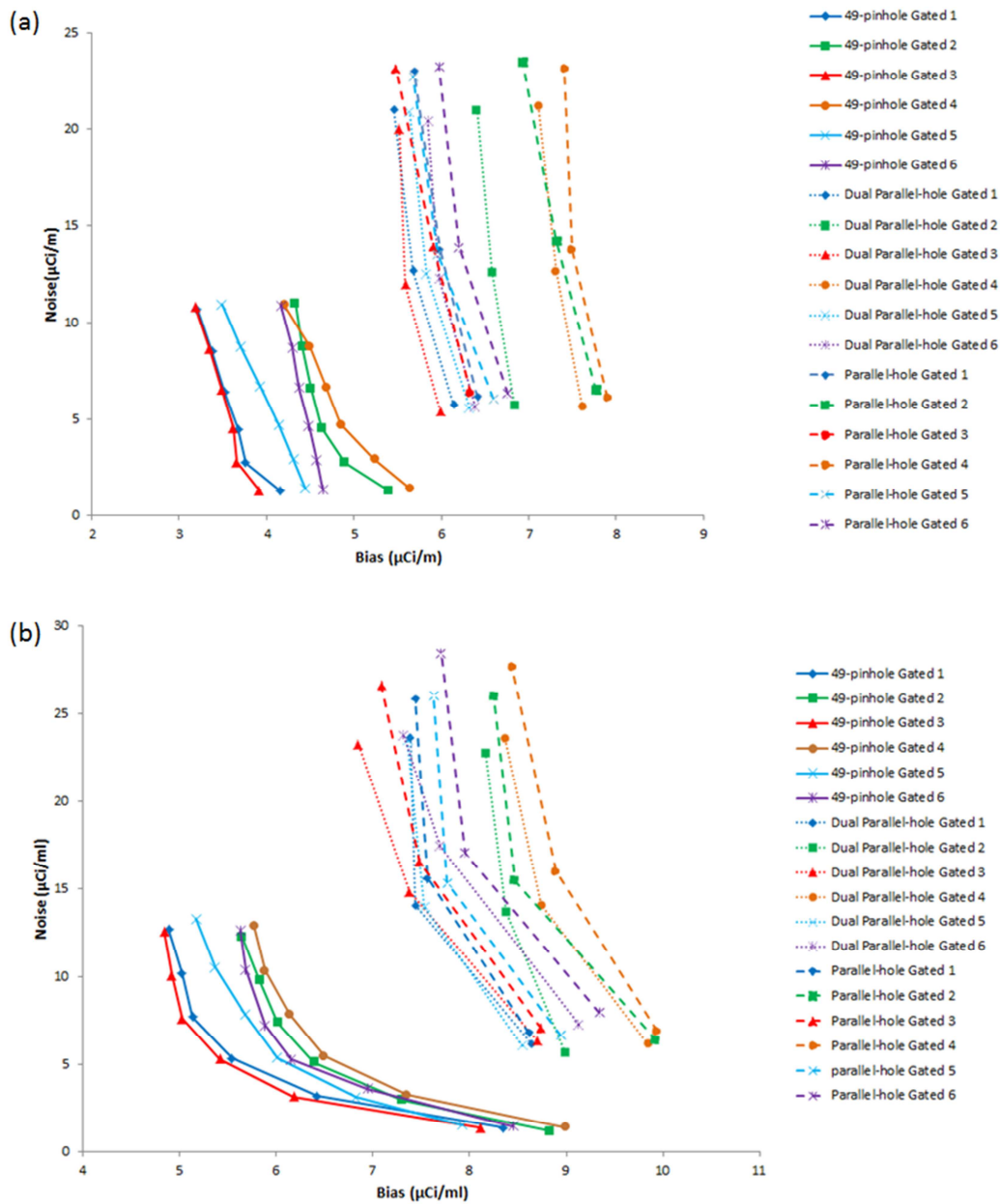
Figure 52: Plots of noise versus bias for the 49-pinhole ROI system (solid line), and the dual-head parallel-hole system (dotted line), and single-head parallel-hole system (dashed line), at each of 6 gates, for (a) 10 mm diameter tumor with 2 cm diaphragm motion and (b) 20 mm diameter tumor with 4 cm diaphragm motion. The iteration number increases from lower right to upper left: from 1 to 6 iterations for the 49-pinhole system and from 1 to 3 iterations for dual-head and single-head parallel-hole systems.

Figure 53 shows tumor positions, as estimated in the localization study, overlaid on the activity phantom. for 49-pinhole ROI imaging and broad cross-section parallel-hole imaging, for the 10 mm diameter tumor with 2 cm motion and the 20 mm diameter tumor with 4 cm motion. There are 25 markers for each tumor, representing the 25-image noisy ensembles. Localization is more accurate using the 49-pinhole ROI imaging than the broad cross-section parallel-hole imaging, evidenced in that for ROI imaging the estimated markers are more tightly distributed about the true tumor positions.
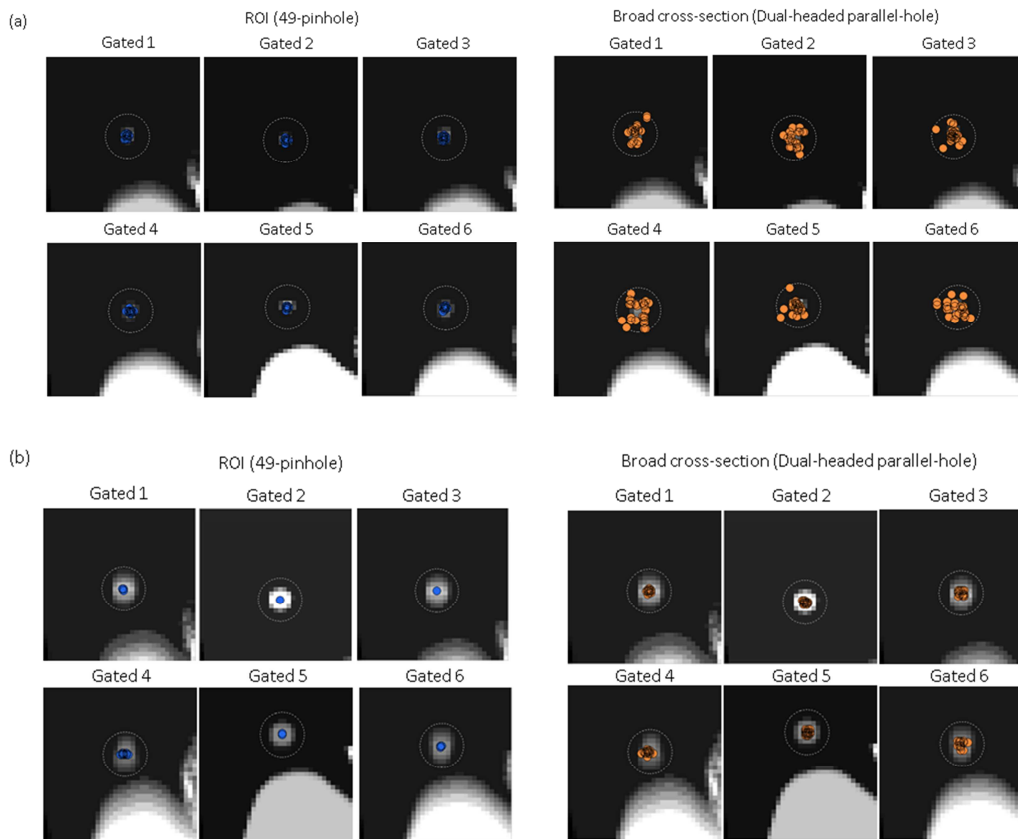
Figure 53: Tumor positions estimated from 25-image ensembles are plotted on the activity phantom for ROI and the broad cross-section dual parallel-hole imaging systems. (a) 10 mm diameter tumor with 2 cm diaphragm motion. (b) 20 mm diameter tumor with 4 cm diaphragm motion. The bright spots are true tumor positions, and the search-region boundaries are indicated by dotted white lines. Correct localizations are centered exactly in these circles.

Tumor localization errors were calculated across an ensemble of 25 noisy realizations. Figure 54 shows the box-and-whisker plot of tumor localization errors in each respirotary gate, for the ROI and broad cross-section systems, for 10 mm diameter and 20 mm diameter tumors. The 10 mm diameter tumor has an average median error of 1.6 mm and 6.6 mm over 6 gates using the ROI imaging and the broad cross-sction

imaging system, respectively. The 20 mm diameter tumor has an average median error of 0.5 mm and 2.3 mm over 6 gates using the ROI imaging and broad cross-sction imaging systems, respectively.

P-values from two-tailed Wilcoxon rank sum tests with 5% significance level are shown in Table 13. Localization errors for the ROI system were statistically significantly less than those for the broad cross-section system, for both the 10 mm tumor with 2 cm motion and the 20 mm tumor with 4 cm motion. For the comparison between 10 mm diameter and 20 mm diameter tumors, both the ROI imaging and broad cross-section imaging showed statistically significantly less error for the 20 mm tumor than 10 mm tumor.
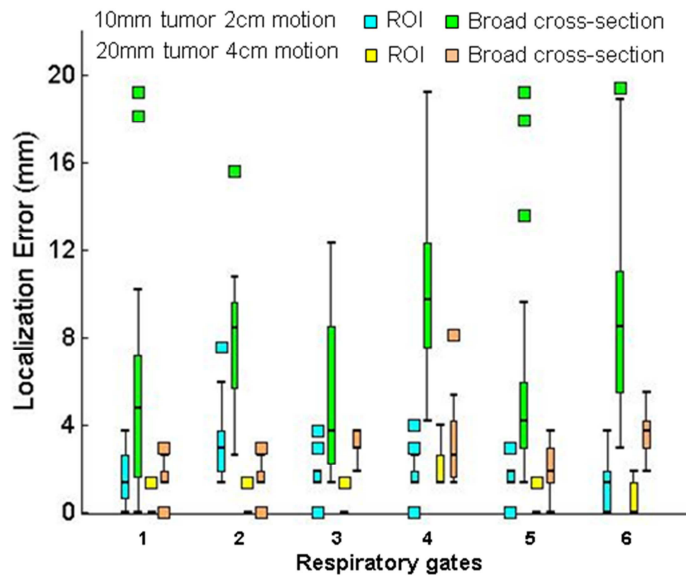
Figure 54: Box-and-whisker plots of tumor localization errors in each respiratory gate, for ROI and broad cross-section imaging systems, for the 10 mm diameter tumor with 2 cm diaphragm motion and the 20 mm diameter tumor with 4 cm diaphragm motion.

Table 13. P-values from two-tailed Wilcoxon rank sum test with 5% significance level. Numbers in bold are p<0.05.

Respiratory Gate	ROI vs. Broad cross-section (Dual-head)		20 mm diameter tumor vs. 10 mm diameter tumor	
	10 mm diameter tumor 2 cm motion	20 mm diameter tumor, 4 cm motion	ROI	Broad cross-section (Dual-head)
1	< 0.001	< 0.001	< 0.001	< 0.001
2	< 0.001	< 0.001	0.001	< 0.001
3	< 0.001	< 0.001	< 0.001	0.152
4	< 0.001	0.004	0.085	< 0.001
5	< 0.001	< 0.001	< 0.001	< 0.001
6	< 0.001	< 0.001	0.678	< 0.001

7.5 Discussion

Currently, the planning CT procedure for radiation therapy has been developed to incorporate respiratory motion information, so as to accurately delineate a target region. 4D CBCT has also been investigated for on-board 4D imaging capability. To complement the anatomical information provided by 4D-CT and 4D-CBCT, and to enhance the treatment planning based on functional and molecular information, respiratory-gated SPECT imaging is investigated here. Specifically, a ROI SPECT system with a 49-pinhole collimator was proposed to enhance respiratory-gated lung imaging by reducing the noise and improving the resolution-versus-sensitivity tradeoffs, as compared to conventional broad cross-section imaging techniques. This proposed system could also provide functional and molecular imaging on-board radiation therapy machines. Currently there is little or no technology for on-board molecular and functional imaging. This novel 49-pinhole collimator design could provide respiratory-

gated SPECT imaging in as little as 4 minutes, which is much faster than conventional clinical broad cross-section SPECT imaging, which typically requires h greater than 20-minute scan times.

In this study, the ROI for the 49-pinhole SPECT system was a sphere 8.24 cm in diameter. The purpose of using the ROI methods is to improve imaging sensitivity and resolution. However, one possible challenge is that the ROI may not fully contain the tumor over its full range of motion. Therefore, a smaller tumor of 10 mm diameter with smaller diaphragm motion of 2 cm in superior-inferior direction and a larger tumor of 20 mm diameter with larger diaphragm motion of 4 cm in superior-inferior direction were investigated. The 2 cm and 4 cm motion ranges were chosen based on the previous research which suggests that the range of the diaphragm motion is from as little as 0.4 cm to as much as 3.8 cm[150, 151]. As has been shown in Figure 51, the ROI fully covers the tumor at each respiratory gate, even for 4 cm diaphragm motion. The bias-versus-noise and localization studies provide quantitative confirmation that the 20 mm tumor with 4 cm motion can be imaged by ROI methods.

As indicated in the introduction, one of the major challenges of respiratory-gated imaging using broad cross-section SPECT systems is image and/or long imaging time. We hypothesized that the ROI imaging technique could reduce the noise and/or provide shorter imaging times. As shown in Figure 52 , with 4-minute scan times, images from the proposed ROI system have much less noise than those from the broad cross-section

imaging system. The bias of the ROI system is smaller than the broad cross-section system at a given noise level. In addition, the localization studies demonstrated the statistically significant improvement of tumor position estimation with ROI imaging system.

The profiles through the tumor are different between different respiratory gates. This could be because of noise fluctuations. In addition, the tumor motion is less than the diaphragm motion which was 2 cm or 4 cm.

Furthermore, the ROI detector proposed in this study has been investigated for other anatomical sites, such as supine breast[27], prone position breast imaging[152] and prostate imaging[153]. The respiratory gated ROI imaging technique investigated in this paper could also have the potential application in other sites and beyond radiation therapy, for example liver tumor imaging and myocardial imaging.

7.6 Conclusions

The proposed ROI SPECT system with 49-pinhole collimator shows noise reduction and accurate tumor localization accuracy for respiratory-gated lung tumor imaging with a 4 minutes scan time. The ROI of the 49-pinhole system can effectively cover a reasonable sized tumor and up to 4 cm diaphragm motion. This ROI imaging system with a robotic arm has the potential application for other respiratory-gated imaging besides lung tumors.

8. Hardware Robotic SPECT System

8.1 Laboratory Room Design

To implement a robotic SPECT system, a laboratory has been developed including the Kuka KR 150-L110 robotic and Digirad 2020tc detector parallel-hole and single pinhole collimators.

The laboratory room was designed by considering the physical constraints and requirements of the robotic arm, the treatment table, a safety fence and the operator console. Several criteria were considered: (a) the movement of the robotic arm must be able to reach around the treatment table and be able to perform imaging trajectories for different anatomical sites, (b) the robotic arm must not collide with the walls, and (c) the fence should be positioned to protect operator.

The robot is positioned at about the center of the room as shown in Figure 55. The distances from the center of the robot to the walls are $12'9\frac{7}{8}''$ to the back wall, $14'6\frac{3}{8}''$ to the left wall, $11'11\frac{1}{16}''$ to the right wall and $15'8\frac{1}{4}''$ to the front wall. The robot is rotated 68.4 degree from the vertical center line of the room, facing the upper left corner of the room where the imaging table is placed. The fence is placed in the room at the

129

lower right corner to protect the operator as shown in Figure 55. The fence is placed in an arc shape 11.35′ from the center of the robot, such that the robot equipped with the parallel-hole detector does not collide with the operator if it is deployed backward, as shown in Figure 55(b). A 1.7′ clearance between the end of the detector and the fence is reserved here to achieve this collision requirement.
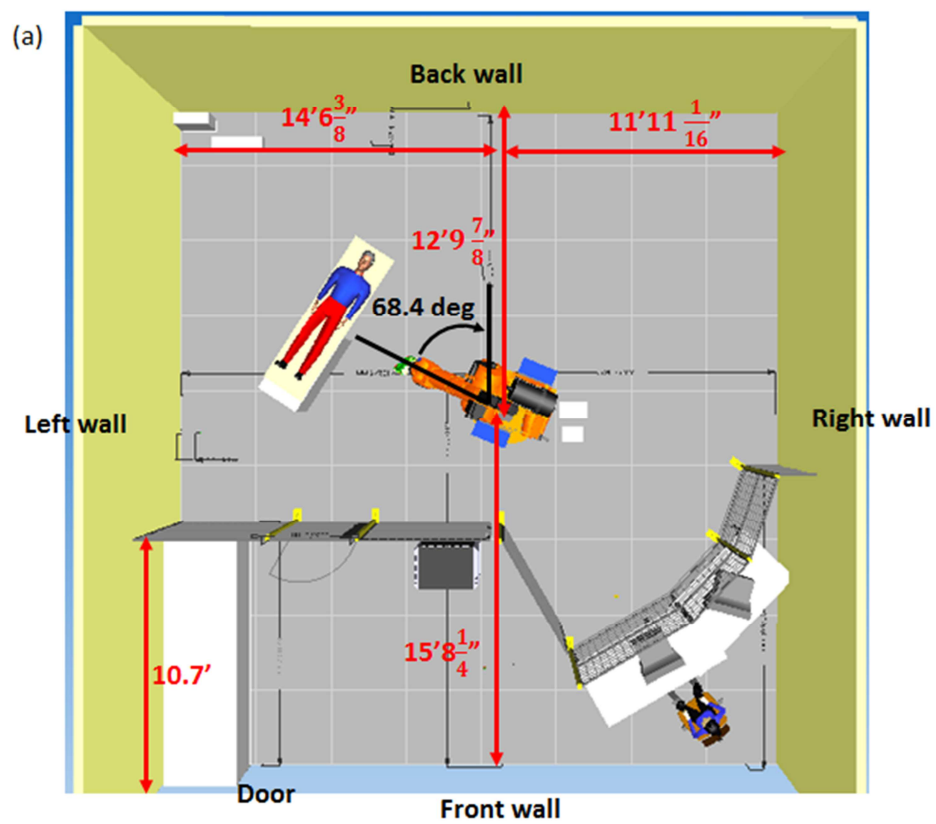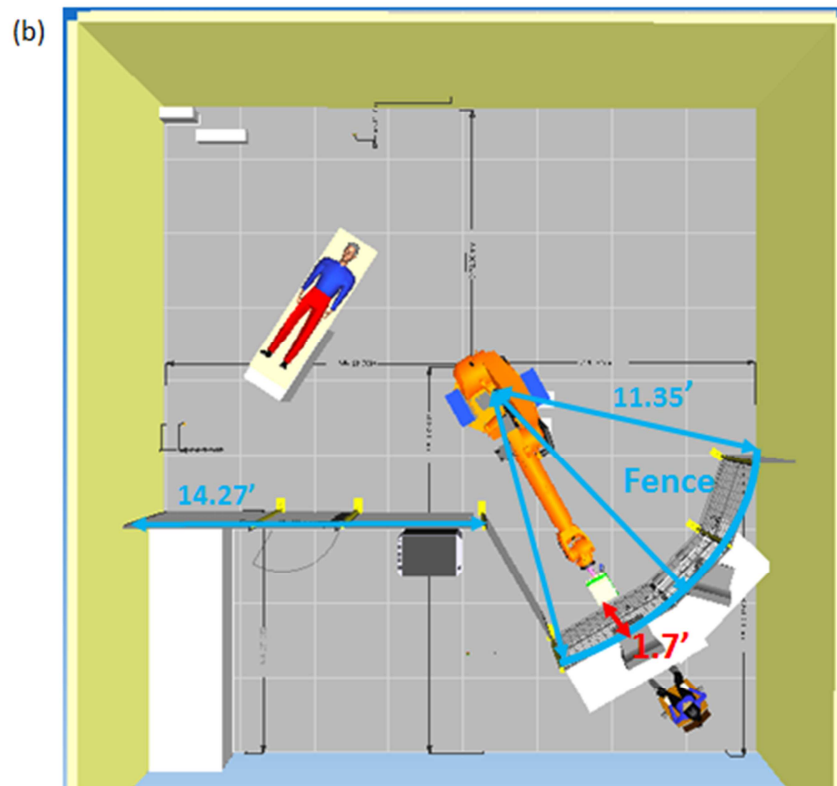
Figure 55: Laboratory room design of the robotic SPECT system. (a) The robotic arm is positioned at about the center of the room: $12'9\frac{7}{8}''$ to the back wall, $14'6\frac{3}{8}''$ to the left wall, $11'11\frac{1}{16}''$ to the right wall and $15'8\frac{1}{4}''$ to the front wall. The robot is rotated 68.4 degree from the center vertical line of the room, and is perpendicular to the imaging table positioned at the upper left corner. (b) The fence is placed with the dimensions shown in the figure. The right part of the fence is in an arc shape to ensure no collision is possible when the robotic arm is deployed backward.

The home position of the robot is indicated as the black line (the center line of the robot) in Figure 56 and two software rotation limits are set as a safety precaution. Hardware limit 1 is set to 60 degree, clockwise from the home position to prevent collisions and to protect operators, as shown in Figure 56(a). At this position, when the

131

arm is deployed forward maximum, there is 1.6' distance clearance to the back wall.

Hardware limit 2 is set at -35 degree counterclockwise from home position of the robot

such that the robot does not rotate further to the fence as shown in Figure 56(b). The

clearance distance at this position is 2' to the left wall when the arm is deployed forward

maximum. The distance to the right wall at this position is 2.3' when the arm is

deployed to the maximum extent backward as shown in Figure 56(c).

(b)

Left wall

0deg

-35deg

2'
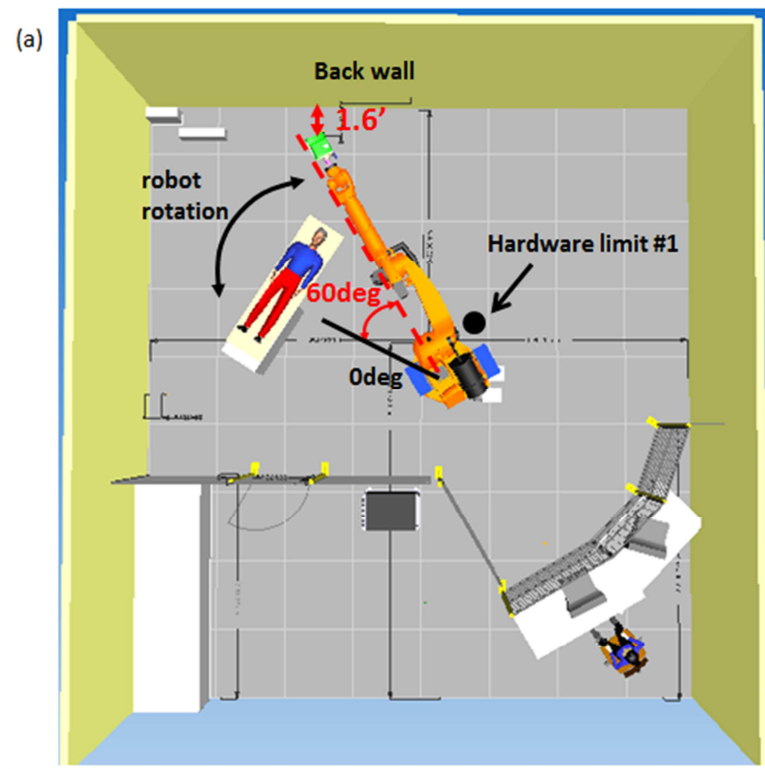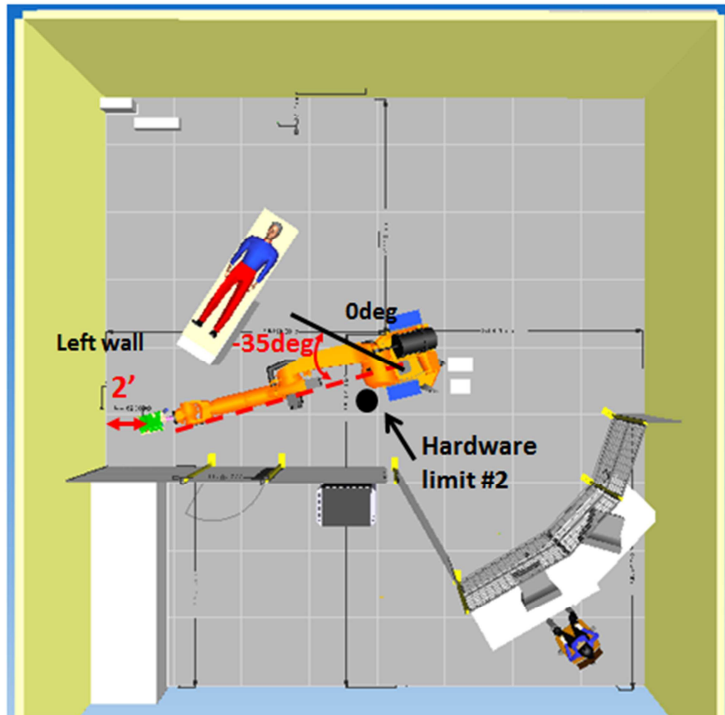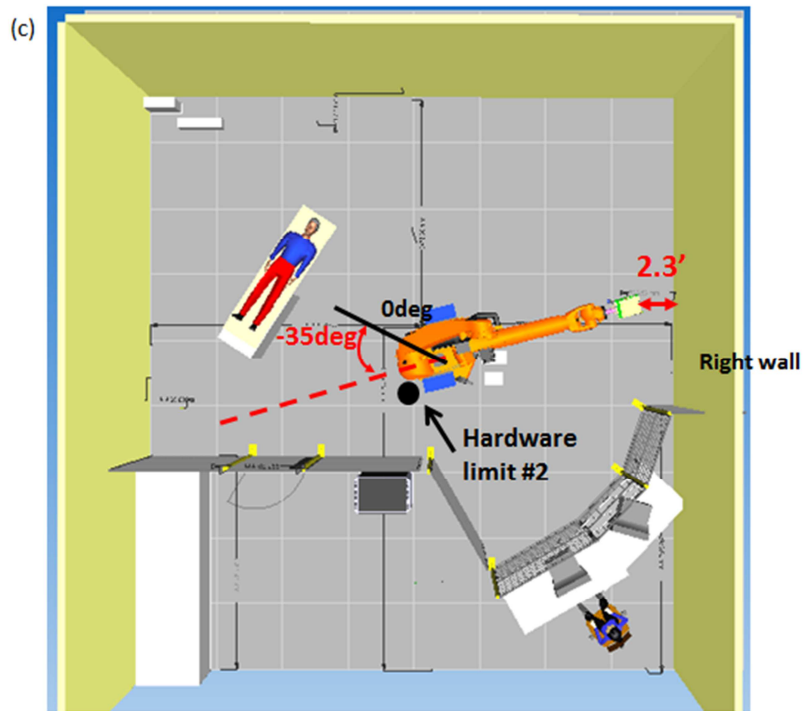
Hardware limit #2

Figure 56: Rotation limits of the robotic arm. The black line indicates the home position of the robotic arm. (a) Hardware limit 1 is set at 60 degree clockwise from the home position. (b) Hardware limit 2 is set at -35 degree counter clockwise from the home position. The robotic arm is deployed forward. (c) Robot is at hardware limit 2 and the arm is deployed backward.
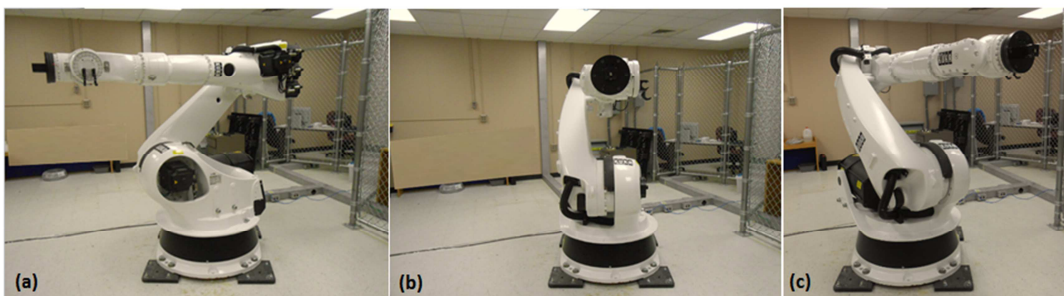
Figure 57: (a) Robot at hardware limit 1 rotates 60 degree from (b) the home position of the robot. (c) Robot at hardware limit 2 rotates -35 degree from the home position.

134

The fence was designed to follow guidelines in the American National Standard for Industrial Robots and Robot Systems — Safety Requirements[154], as shown Figure 58. The fence height needs to be greater than 0.9 m. The distance from top of the fence to the ceiling needs to be less than 1.5 m and the distance from bottom of the fence to the floor needs to be less than 0.3 m. The ceiling of the lab is 2.7 m. The fence opening hole size needs to have a side length between 32 mm to 49 mm. An interlock gate is needed such that when the gate is open, the robot cannot be operated in auto mode.
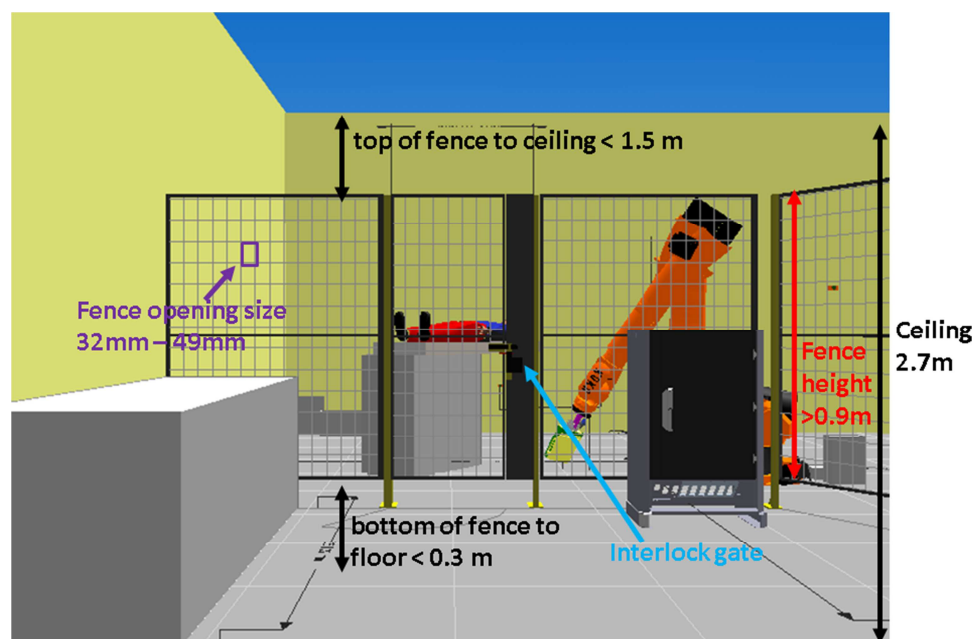
Figure 58: Fence design for the robotic SPECT imaging laboratory following the American National Standard for Industrial Robots and Robot Systems — Safety Requirements. The room ceiling height is 2.7 m. The fence height needs to be greater than 0.9 m. The distance from top of the fence to the ceiling needs to be less than 1.5 m and the distance from bottom of the fence to the floor needs to be smaller than 0.3 m. The fence opening hole size needs to have a side length between 32 mm to 49 mm.

The robotic SPECT imaging lab is shown in Figure 59. The Kuka KR 150-L110 robot is mounted on the floor. The robot controller is outside the fence and next to an interlock gate to allow access inside of the fence with the teach pendant.

Figure 59: Robotic SPECT imaging lab. The robot is mounted on the floor. The robot controller is shown in the right corner of the image. The fence is installed with an interlocked gate.

8.2 Robotic SPECT Detector Operating Procedures

8.2.1 Digirad Detector

Two detectors are used in the lab, a dummy detector housing for testing the imaging trajectories and a real detector for acquiring SPECT projections, as shown in

Figure 60(a), (b) and (c). The real detector has a black conduit attached to it which contains the data line, two water hoses for the chiller and two plastic tubes for air dryer.

The connection of detector to its accessories is shown in Figure 61(a). The air dryer is controlled by a humidity indicator, as shown in Figure 61(b) and (c). The air dryer is used to control the humidity of the detector and should be left on all the time. The humidity indicator should be in blue color for two of the three sectors (the 10% and 15% sectors) (Figure 61(c)). When the indicator turns to red color, one must change the desiccation beans inside the dryer to ensure proper humidity control. The Agilent power supply (Figure 61(b)) is used to provide power to the detector. It should be set to 7.6 V and 5 A for detector operation. The detector needs to be cooled whenever the power supply in on. A water chiller is used to cool the detector to its operation temperature of 8 °C. Figure 61(d) shows the chiller.
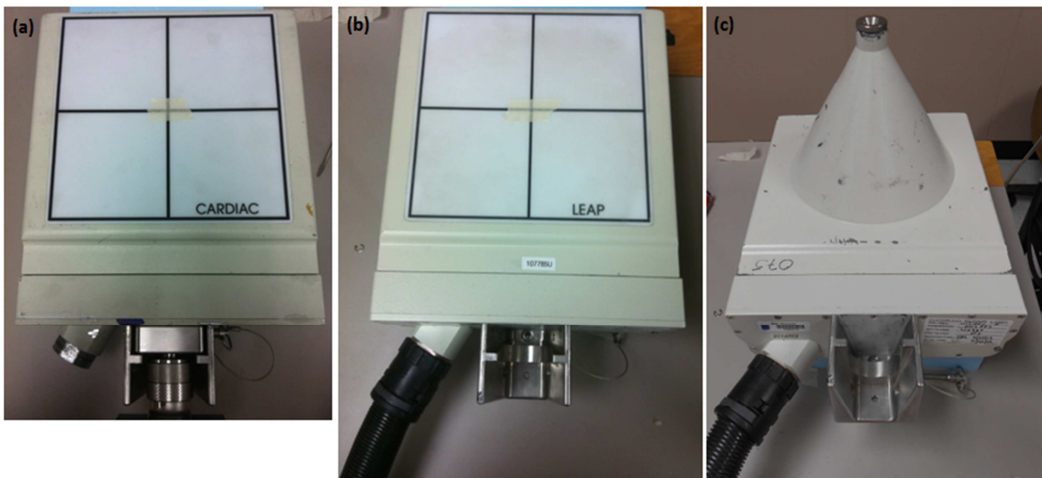
Figure 60: Digirad detector (a) dummy detector housing with parallel-hole collimator used for testing imaging trajectories. Real detector with (b) parallel-hole collimator and (c) pinhole collimator with black conduit containing data line, water hose for chilling purpose and air dryer tube.
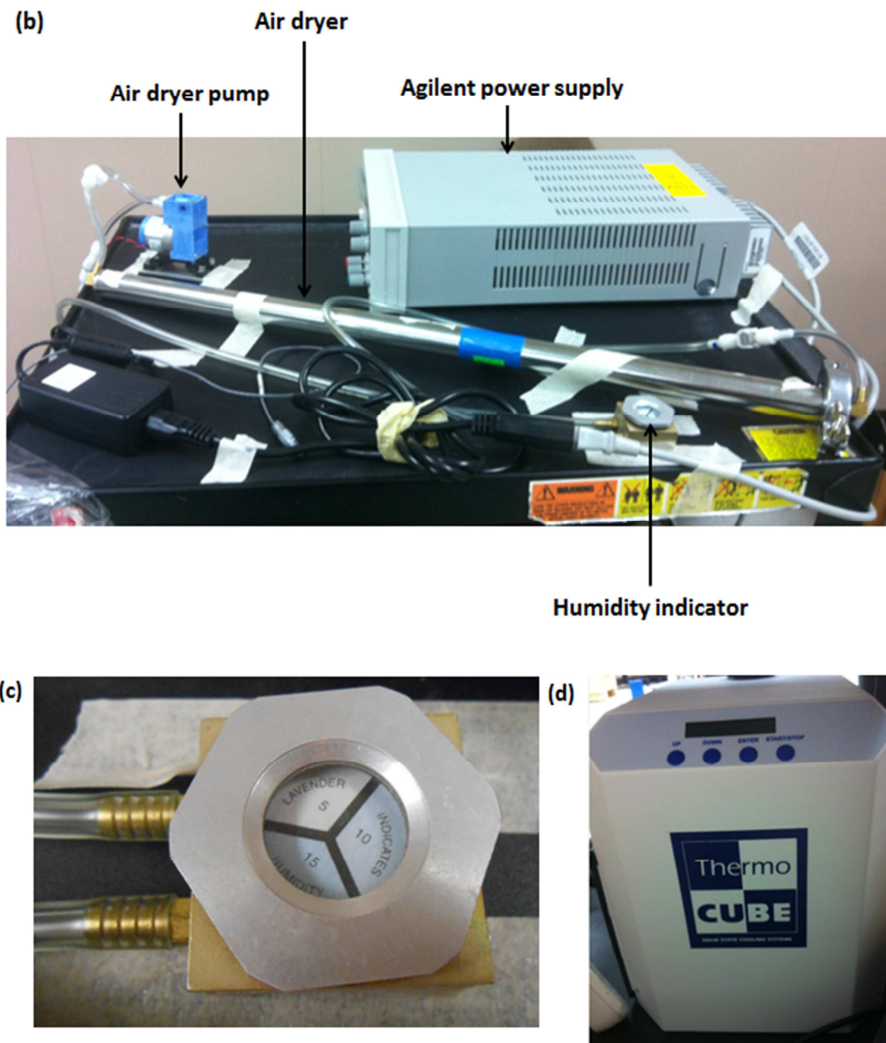
Figure 61: (a) Digirad detector connection to the accessories. The detector data line is connected to the computer for image acquisition. (b) Accessories: air dryer, air dryer pump, humidity indicator, Agilent power supply. (c) Humidity indicator. (d) Water chiller for cooling the detector.

8.2.2 Robot Safety Operation Tests

Two safety operation tests need to be performed immediately after the booting sequence of the robot controller. The mastering test ensures that the current robot position is referenced to the base of the robot. Only if the mastering test is successful, can the robot be operated safely. This test is performed by running the robot with an actuating plate attached to the flange of the robotic arm, as shown in Figure 62(a). A reference switch (Figure 62(b)) is placed on a stand at a fixed position with two sensors (green dots) for actuating. The status of the two sensors is indicated by two lights on the reference switch (Figure 62(c)). For this mastering process, the robot has been programed to approach the reference switch. When the actuating plate actuates the reference switch (Figure 62(d)), the two indication lights are off (Figure 62(e)) which means the mastering test is successful.
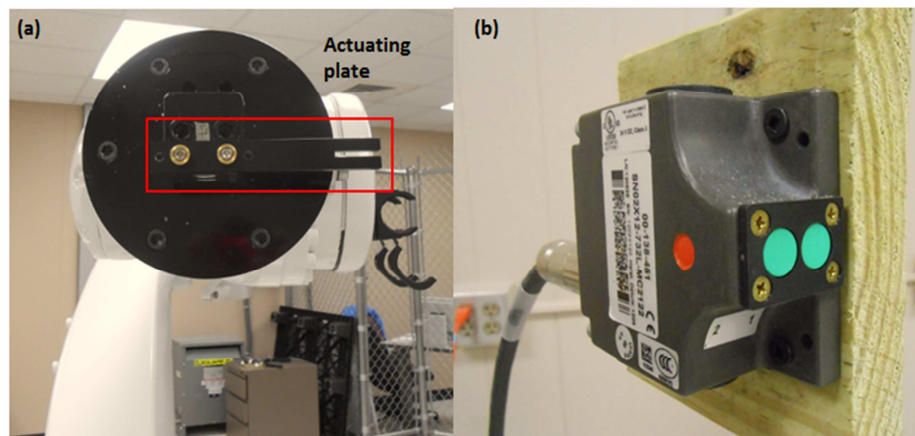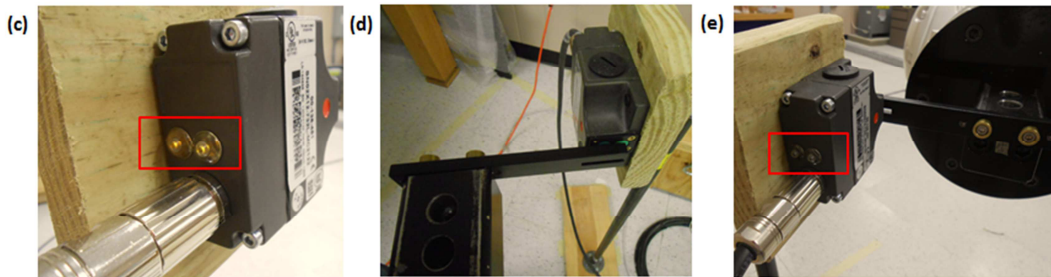
Figure 62: (a) Actuating plate attached to the robotic arm, shown in the red box. (b) Reference switch for the mastering test. The two green dots are for matching the actuating plate pitch fork which is shown in (d). (c) Two indicating lights are on when it is not actuated by the actuating plate. (d) The robotic arm with the actuating plate attached approaches the reference switch. (e) Two indicating lights are off as the actuating plate matches the green dots as shown in (d).

After the mastering test, the brake test needs to be performed. The robot is operated in auto mode to test if each of the six axes can be stopped immediately. This test ensures the functionality of the brakes of each axis. All six axes need to pass the break test.

The procedures of mastering test and break test are included as Appendix A.

8.2.3 Detector Pickup and Set-Down Procedure

To pick up the detector, a male detector-robot joint was constructed as shown in Figure 63(a). The matching female joint is on the robotic arm as shown in Figure 63(b). The male joint can be attached to either the dummy or the real detectors that are set side by side as shown in Figure 64. The robot arm is programed to approach the male joint

and to slowly insert the female joint into the male joint, as shown in Figure 65. Once the

joint is in, two bolts are fastened to secure the attachment (Figure 65(e)). The pickup

code for the dummy detector is shown in Figure 66(a). The code is similar for the real

detector except for the detector position on the table.

After imaging, the detector needs to be set down to its original position on the

table, and the robotic arm needs to be retracted back to the home position. Therefore,

dummy/real detector set-down and release codes have been written for this purpose.

Figure 66(b) and (c) shows the dummy detector set down and release code, respectively.
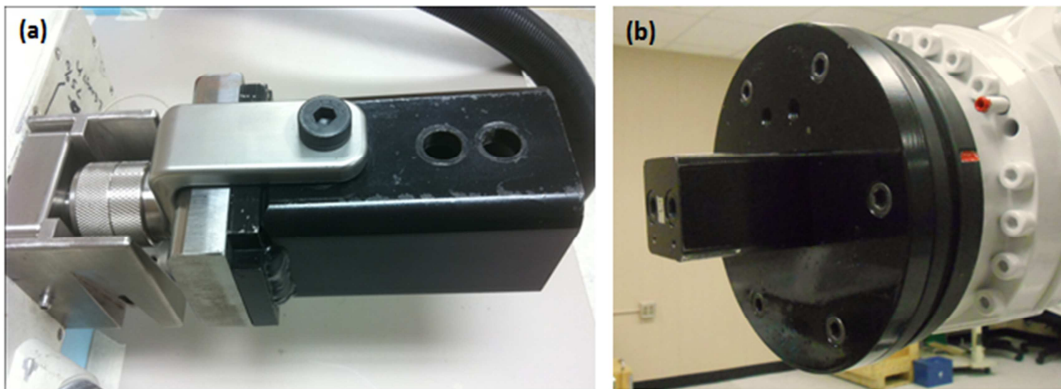
Figure 63: (a) Male detector-robot joint for attaching the detector to the robotic arm. (b) The matching female part of the detector-robot joint is bolted on the robotic arm.
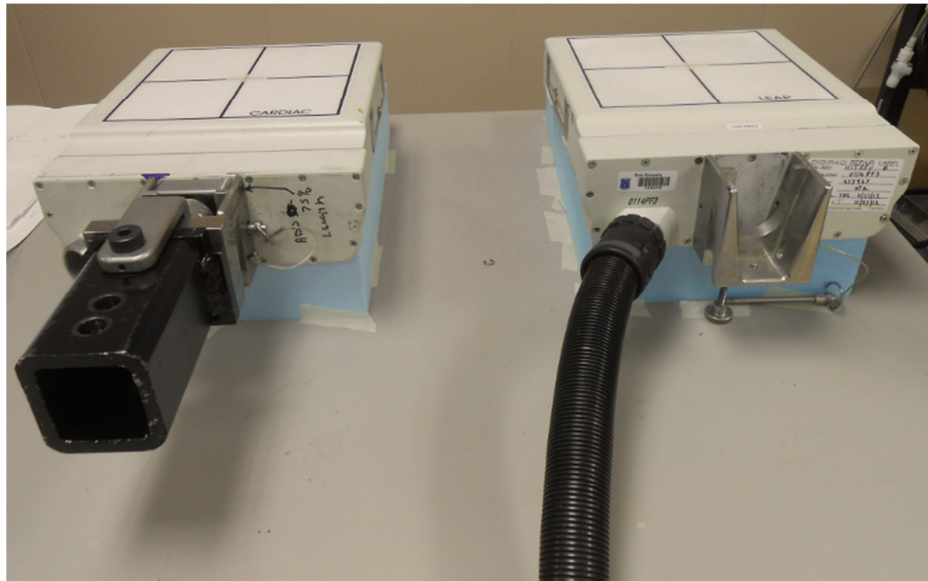
Figure 64: The dummy (left) and the real (right) detectors are set side by side for picking up by the robotic arm. The male detector-robot connection can be switched between the dummy detector and the real detector.
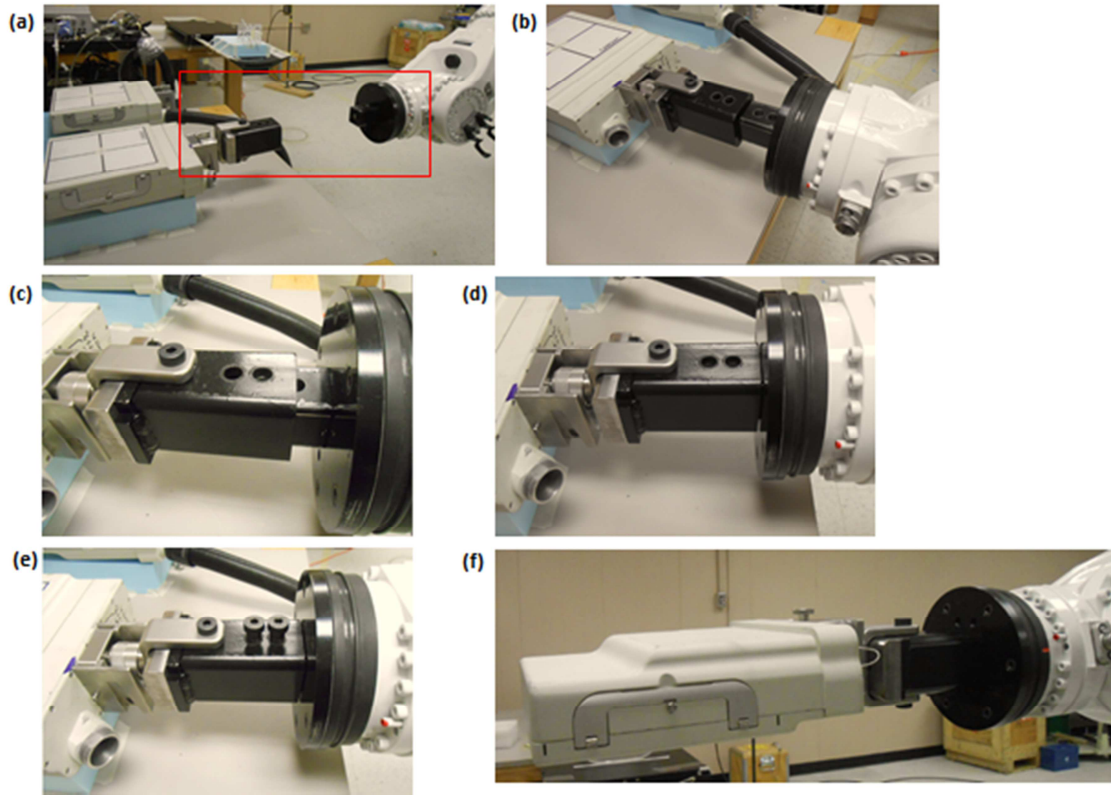
Figure 65: (a)-(d) The robotic arm with the female detector-robot joint attached approaches the detector with the male joint attached. The female joint is inserted to the male joint. (e)Two bolts are used to fasten the joints. (f) The detector is attached to the robotic arm and is ready for robotic SPECT imaging.

(a)

(b)
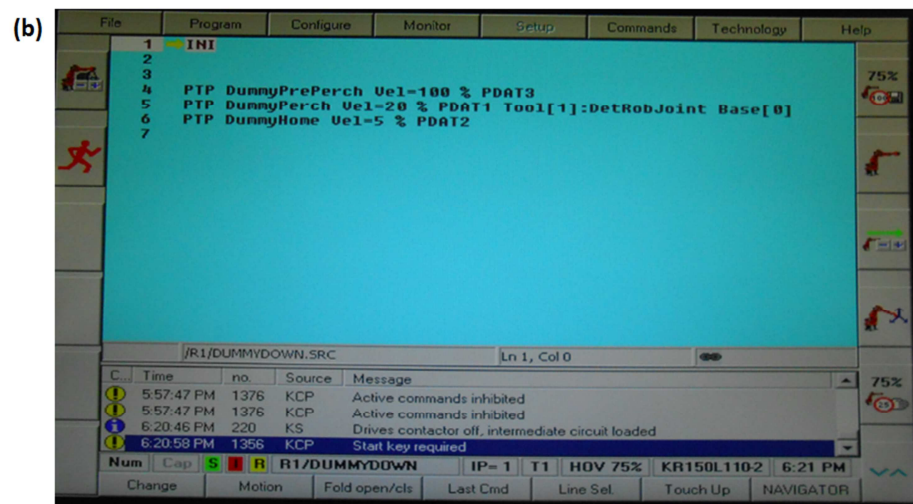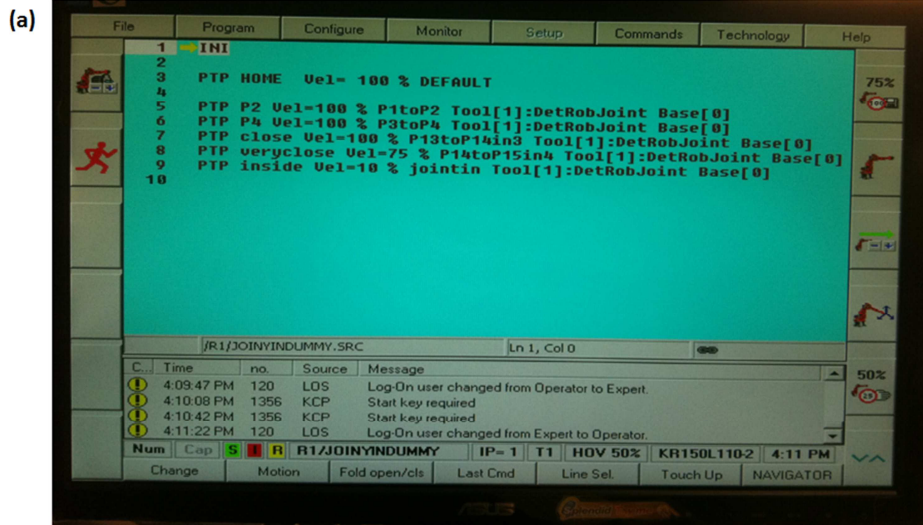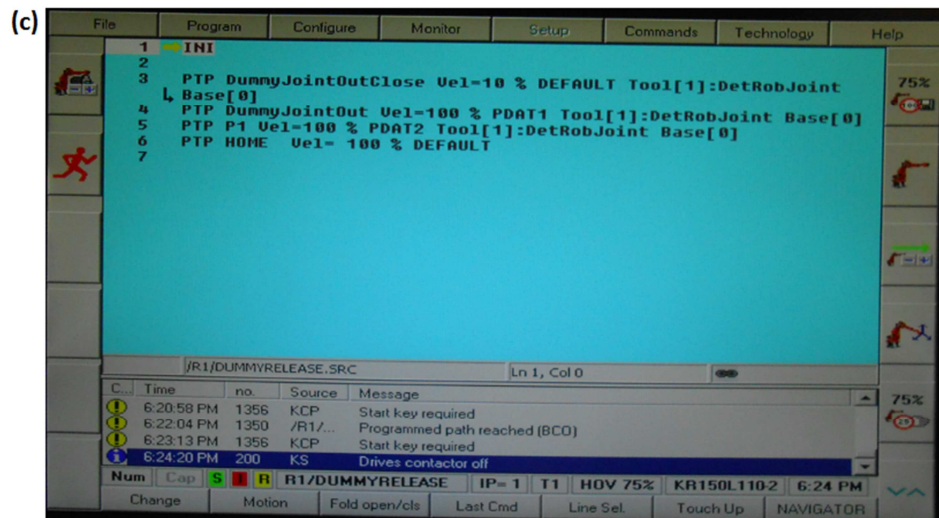
Figure 66: (a) Detector pickup code. (b) Detector set-down code. (c) Detector release and back to home position code.

8.3 A Prototype Robotic SPECT System

8.3.1 Introduction

On-board robotic SPECT has been proposed to provide functional and molecular information of the tumor while the patient is on the radiation therapy table[27, 114]. There are several advantages of robotic SPECT. One is that the robot can bring the SPECT detector to the patient in position for radiation therapy, and after imaging, retract the detector to enable normal operation of the radiation therapy system. A second advantage is that the robot can maneuver the SPECT detector around an offset center of rotation, enabling focused region-of-interest (ROI) imaging at various anatomical sites. A third advantage, notable for on-board imaging, is that a robotic SPECT system could be versatile in navigating the SPECT detector near the radiation-therapy flat-top couch

146

so as to minimize the distance between the detector and the ROI. In our previous work, computer-simulation studies have demonstrated this versatility, and the imaging potential of robotic SPECT[27, 152].

In the present study, we integrate an industrial robot with a gamma camera to construct a hardware robotic SPECT system. This first-ever, robotic SPECT system for onboard imaging is utilized herein for hardware investigations into the versatility of robotic SPECT in maneuvering a gamma camera about a thorax phantom on a widely-used, flat-top radiation-therapy treatment table. Trajectories investigated include parallel-hole imaging of a larger ROI and pinhole imaging of a comparatively small ROI. The two ROIs were centered at different locations to demonstrate the imaging versatility of robotic SPECT.

For typical gantry-based SPECT systems, detector pose (*i.e.* position and orientation) is characterized by a single rotation angle, and SPECT image reconstruction can be performed by obtaining this angle from the gantry system. Here, for robotic SPECT, image reconstruction is performed with detector pose obtained from "base" and "tool" coordinates provided by the robot system. Utilization of these coordinates demonstrates applicability of robot technology, highly developed for precise industrial applications, to SPECT imaging.

8.3.2 Materials and Methods

8.3.2.1 Robotic SPECT system

A robotic SPECT system was constructed (Figure 67) utilizing a Digirad 2020tc detector (Digirad Corporation Poway, CA) and a KUKA KR150 L110 robot (KUKA Robotics, Aktiengesellschaft, Augsburg, Germany). The 2020tc detector consists of a CsI(TI) scintillator with 64x64 pixels on a 3.25 mm pitch. The imaging area is 20.8 x 20.8 cm^2. Attachable to the 2020tc detector were a low-energy medium-resolution parallel-hole collimator and a pinhole collimator. The parallel-hole collimator has hexagonal holes on a hexagonal grid. The parallel-hole collimator has a hole length of 22 mm, a flat-to-flat hole diameter of 1.5 mm and a septal thickness of 0.2 mm. The pinhole collimator has a tungsten pinhole with 3 mm diameter, a 70 degree full pinhole opening angle and a 175 mm focal length.
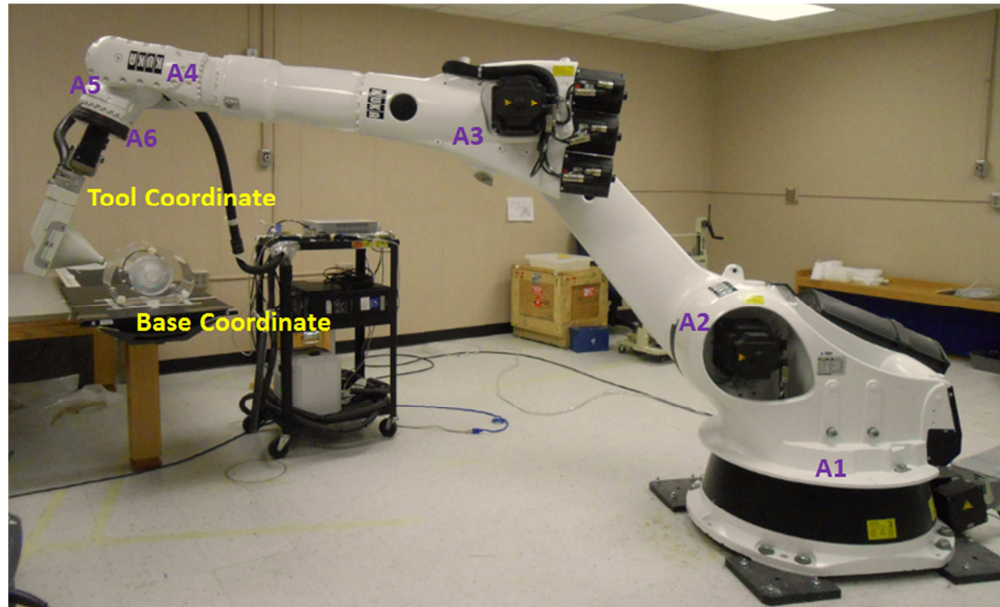
Figure 67: Robotic SPECT system, including a KUKA KR 150 L110 robot and an attached pinhole-collimated SPECT detector, imaging a ROI on the phantom side distal to the robot, with the phantom on a radiation-therapy flat-top patient table. The robot tool coordinate frame is centered at the pinhole. The robot base coordinate frame is centered on the phantom. The robotic arm has 6 axes of rotation, A1 to A6.

8.3.2.2 Robotic Coordinate and Imaging Trajectories

The robot has 6 axes of rotation (Figure 67), which combine to determine the position and orientation of the detector. The robot controller reports position and orientation by several coordinate frames, which include base coordinate frames and tool coordinate frames (Figure 67). The robotic system allows for user calibration of tool and base coordinate frames. Here the tool corresponds to either the pinhole-collimated or parallel-hole-collimated detector. The purpose of tool calibration is to inform the robotic system of the origin and orientation of the tool coordinate frame. The origin was

calibrated to be either the pinhole or the center of the phantom-side surface of the parallel-hole collimator. The base calibration establishes an additional user-specified coordinate frame. This is done by touching the tool coordinate origin to the user-intended base coordinate origin, then with moving the tool coordinate origin along the user-intended base coordinate x-axis, and finally touching the tool coordinate origin to a point in the base coordinate x-y plane. This process is performed with tool y and z axes parallel to the base x and y axes, respectively, such that the orientation between the tool and base coordinate frames is established. By touching the two origins, the displacement between the two coordinate frames is also established. Here one user-determined base coordinate frame was set with axes parallel and perpendicular to the surface and edges of the flat-top. The CT image of the phantom was then used to determine the shift needed to position another, parallel base coordinate frame at a user-specified location in the phantom, as shown in Figure 68(a) for parallel-hole imaging and Figure 68(b) for pinhole imaging. At each detector stop, the robot reports the position and location of the tool coordinate frame relative to the base coordinate frame, and this provides the information needed for image reconstruction.

For broad-cross section parallel-hole imaging, the center of the thorax phantom was the COR, and the common volume (CV) is a 20.8-cm-diamter cylinder which covers all five spheres (Figure 70 (c)). For pinhole imaging, the COR was placed at the center of the 14.7-cm-diameter CV, covering two spheres in the phantom (Figure 70 (a)). For

parallel-hole collimation, the detector rotation angle θ spanned 180 degrees in 3 degrees per steps. The pinhole trajectory spanned 228 degrees with 3 degrees per stop.
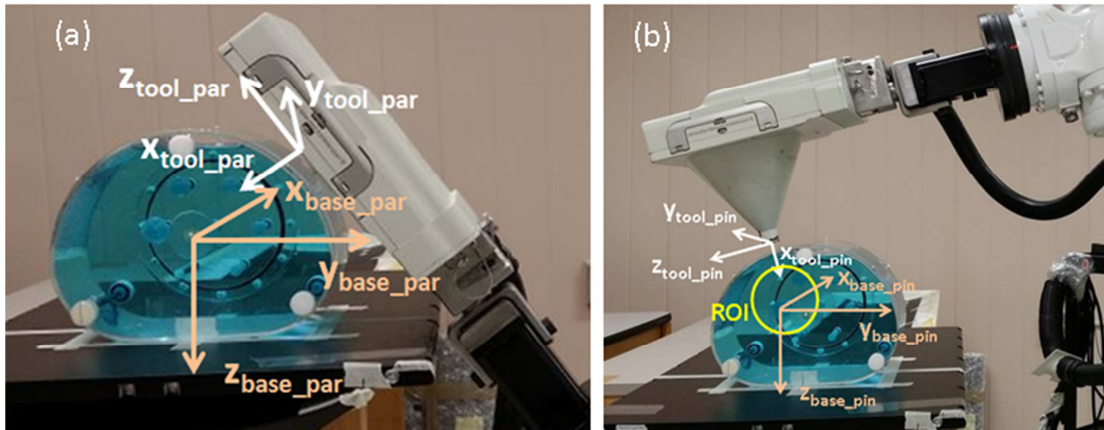
Figure 68: (a) Robot tool coordinates (x_{tool_par}, y_{tool_par}, z_{tool_par}) for parallel-hole collimated detector. The origin is at the center of parallel-hole collimator surface. The corresponding robot base coordinates (x_{base_par}, y_{base_par}, z_{base_par}) were calibrated to be at the center of the phantom. (b) Robot tool coordinates (x_{tool_pin}, y_{tool_pin}, z_{tool_pin}) for pinhole collimated detector. The origin is at the center of the pinhole. The corresponding robot base coordinates (x_{base_pin}, y_{base_pin}, z_{base_pin}) were calibrated to be at the center of the pinhole common volume (CV), which encompasses two spheres in the phantom.

8.3.2.3 Phantom and Imaging

A PET CT Phantom™ (Data Spectrum, Durham, NC), including 5 spheres 10, 13, 17, 22 and 28 mm in diameter, was positioned on a radiation therapy flat-top table, as shown in Figure 4. The filled volume of the phantom excluding the spheres is 10000 ml.

To provide the attenuation map for SPECT image reconstruction, a CT scan of the phantom was acquired (0.6 mm slice thickness and 0.64 mm/pixel pixel size). The CT

image was segmented into water, air and polymethyl methacrylate (PMMA) , and attenuation coefficients of 0.15 cm^{-1}, 0.00017 cm^{-1} and 0.18 cm^{-1} were assigned, respectively.

Four imaging acquisitions were performed using the robotic SPECT system: a parallel-hole collimated and a pinhole collimated scans of the phantom with radioactive filled in the background region (Par-Background and Pin-Background) and parallel-hole collimated and pinhole collimated scans with air in the background region (Par-No-Background and Pin-No-Background).

The Tc-99m activity concentration in each sphere at the start time of image acquisition and the total acquisition time were 3.5 µCi/ml, 26 min and 2.5 µCi/ml, 37 min for Pin-No-Background and Par-No-Background, respectively. The Tc-99m activity concentration in each sphere at the start time of image acquisition and the total acquisition time were 2.0 µCi/ml, 45 min and 1.6 µCi/ml, 61 min for Pin-Background and Par-Background, respectively. Sphere-to- background ratios were 10:1 in the two with-background cases. The Pin-No-Background acquisition was used as a reference such that the acquisition times of other scans were adjusted for radioactivity decay to maintain the equivalent of a 26-minute scan with a background activity concentration of 0.35 µCi/ml. The product of total acquisition time and background activity concentration of each of the four acquisitions was approximately similar.

8.3.2.4 Reconstruction and Image Analysis

SPECT images were reconstructed from the projection data by up to 20 iterations of Maximum-Likelihood Expectation-Maximization (MLEM). The reconstruction modeled attenuation in the phantom, but it did not model the photon scatter.

Profiles of the spheres were plotted in the reconstructed images. The contrast of the spheres relative to background was measured as

$$C = \frac{c_s - c_b}{c_b} \tag{38}$$

where c_s and c_b are the reconstructed activity concentrations in the sphere and background ROIs, as shown in Figure 3(a). The spherical ROI is inside the reconstructed sphere placed off center to avoid the air bubble at the top of the sphere. The background ROI is a 3D shell that co-centric with the corresponding sphere.

Noise was calculated as the standard deviation of the pixel values:

$$Noise = \sqrt{\frac{1}{n-1} \sum_{i=1}^{n} (p_i - \bar{p})^2} \tag{39}$$

where n is the number of pixels in the noise ROI, p_i is the pixel value and $\bar{p}$ is the average pixel value in the ROI. The noise ROI excludes voxels that are within the inner surfaces of the two background shells. The noise ROI for pinhole imaging is shown in Figure 69(b) as the bright region. The noise ROI for parallel-hole imaging is shown in Figure 69(c) as the bright region given by the pinhole noise ROI except excluding voxels not contained in the parallel-hole common volume. Contrast versus iteration, noise

versus iteration and contrast versus noise were plotted for pinhole and parallel-hole images.

RORs for pinhole and parallel-hole imaging trajectories were plotted versus detector angle.
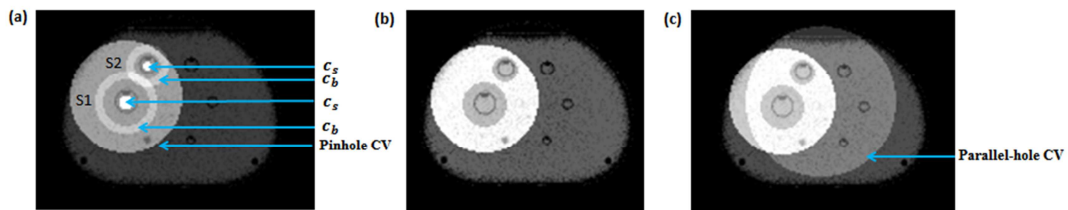
Figure 69: (a) ROIs used to calculate contrast of the spheres relative to background. c_s and c_b are the reconstructed activity concentrations in the sphere and background ROIs. The two 3D ROIs for c_s are indicated by the bright white regions inside the spheres. The background ROIs are the two 3D shells. S1 is the larger sphere and S2 is the smaller sphere. (b) The pinhole noise ROI (white region in (b)) is the pinhole common volume except excluding voxels that are within the inner surfaces of the two background shells. (c) The parallel-hole noise ROI (white region in (c)) is the pinhole noise ROI excluding voxels that are not contained in the parallel-hole CV.

8.3.3 Results

Shown in Figure 70(a) are 4 stops from the 180 degree trajectory of the parallel-hole collimated detector. Four of the stops from the 228 degree are shown in Figure 70(b). The robotic system navigated the detector tracing the flat-top table so as to maintain the closest possible proximity to the phantom, while keeping the target region in the field-of-view (FOV) of the detector and avoiding collision, as shown in Figure 70(c).

154
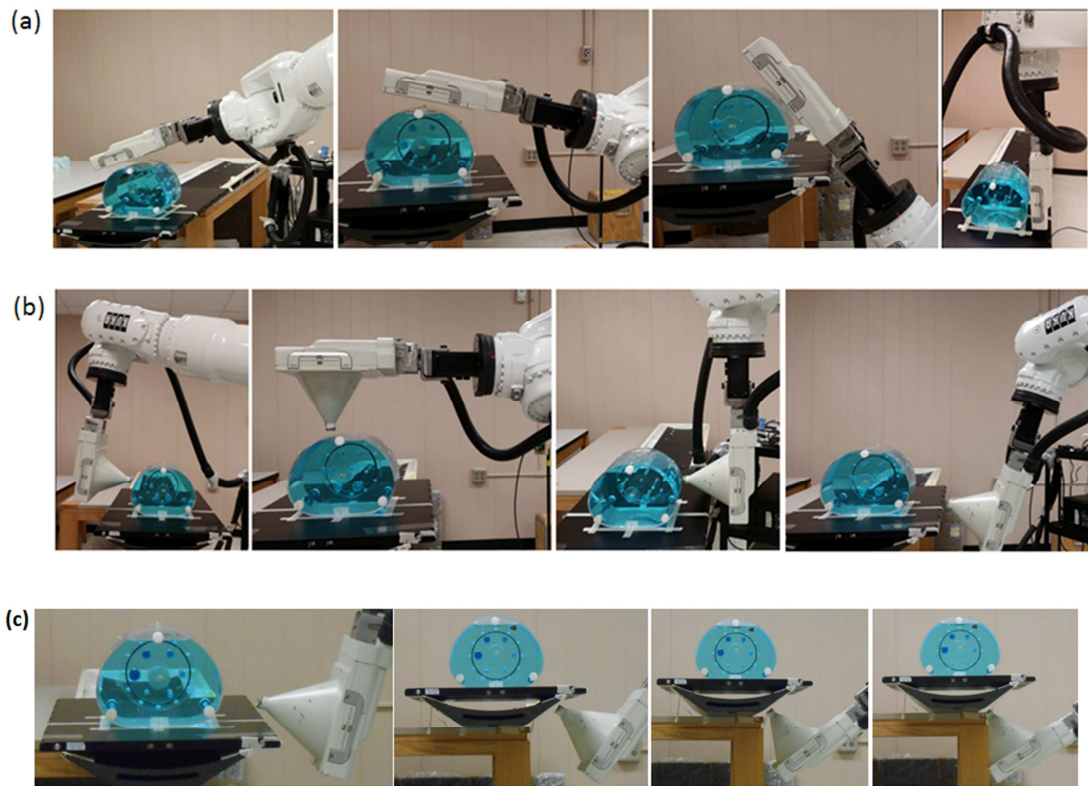
Figure 70: Trajectories for robotic SPECT with (a) parallel-hole collimation (b) pinhole collimation. The phantom is on a radiation-therapy flat-top table. Four of 61 (parallel-hole) or 77 (pinhole) detector stops are shown here. (c) Robotic pinhole SPECT detector navigates near the flat-top table to achieve best-possible proximity to the phantom.

The CT image and the convex hull of the pinhole trajectory containing the entire ROI are shown in Figure 71(a) and (b). The CV of the pinhole imaging system is shown as the bright circle in the phantom with a diameter of 14.7 cm. This CV is centered at the top of the 28-mm-diameter phantom sphere, and covered the 28-mm and 22-mm spheres. The dash line connecting the two pinhole collimator forms the convex hull that covers the CV.
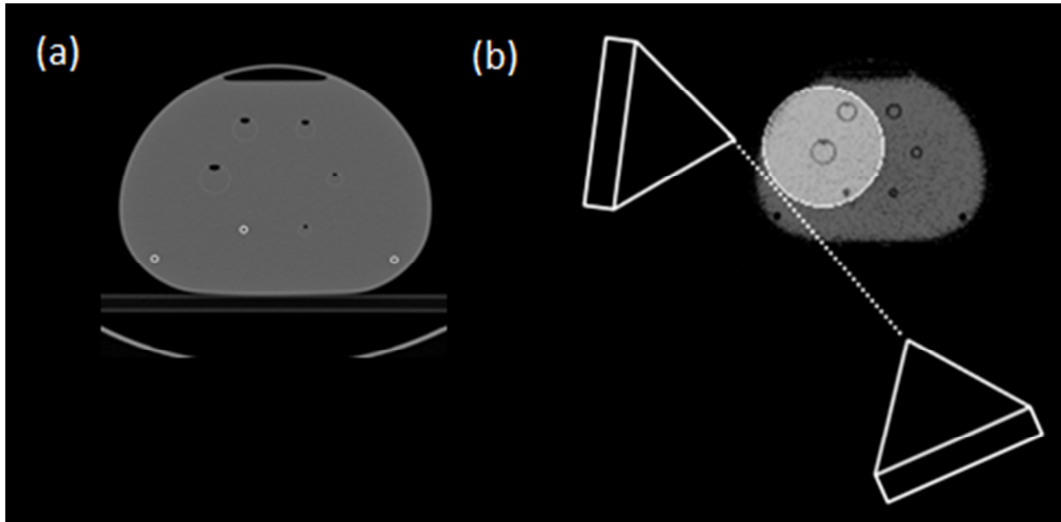
Figure 71: (a) The CT image of the PET-CT phantom with five spheres of 10, 13, 17, 22 and 28 mm diameter. (b) The first (top left) and the last (bottom right) stop of the pinhole detector trajectory are shown here. The dash line connecting the two pinhole collimator forms the convex hull that covers the pinhole CV as shown by the bright circle inside the phantom.

Figure 72 shows transverse views and profiles for images reconstructed from parallel-hole and pinhole collimated SPECT without and with background. In the reconstructed images with no background, all five spheres are visible for both detector systems. In the reconstructed images with background, three of the spheres are visible for parallel-hole system. For the pinhole system, the two spheres in the pinhole common volume are visible, while the three spheres outside the pinhole common volume are not. The image fusion between CT and SPECT shows good overlay of the spheres. The profiles show good sphere-to-background contrast recovery.

Plots in Figure 73 are contrast versus iteration, noise versus iteration, and contrast versus noise. At each iteration, the pinhole image has better contrast (Figure 73(a)) but larger noise (Figure 73(b)) than the parallel-hole image. For pinhole imaging, sphere 2 has higher contrast than sphere 1. For parallel-hole imaging, sphere 1 has higher contrast than sphere 2. Figure 73(c) shows that the contrast-to-noise ratios are comparable for pinhole and parallel images, but the pinhole system achieves higher contrast, e.g. 4.3 versus 4.0 for S1 and 5.3 versus 3.6 for S2 and by iteration 20.
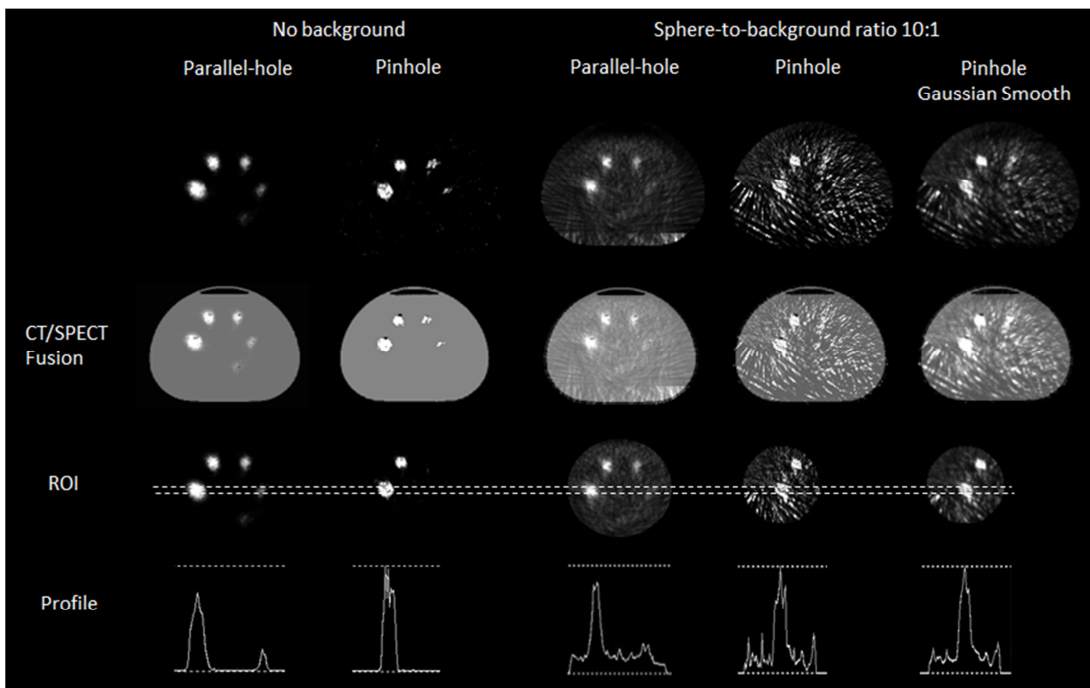
Figure 72: SPECT images for the phantom slice with five spheres without (columns 1-2) and with (columns 3-5) background. The parallel-hole and pinhole images are from iteration 20 of MLEM. The smoothed pinhole image (column 5) was smoothed with a 3D Gaussian kernel of 1.0 sigma. In columns 1-5, SPECT images are shown in row 1 for the entire phantom volume. In row 2, these SPECT images are

fused with the CT image. Row 3 shows the SPECT images that only cover the common volume of the acquisition. A larger common volume for parallel-hole (columns 1 and 3) was used than for pinhole (columns 2, 4 and 5). Row 4 shows profiles through the largest sphere in the row 3 images.
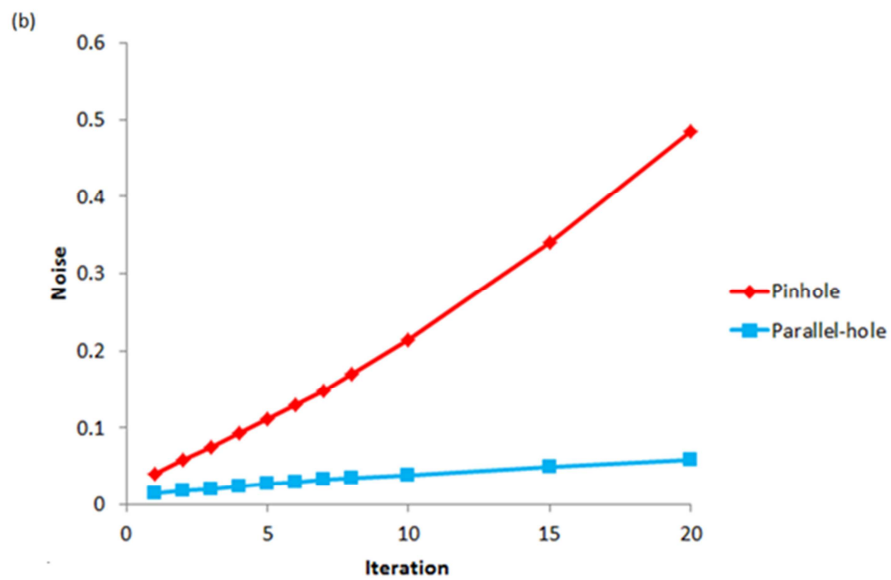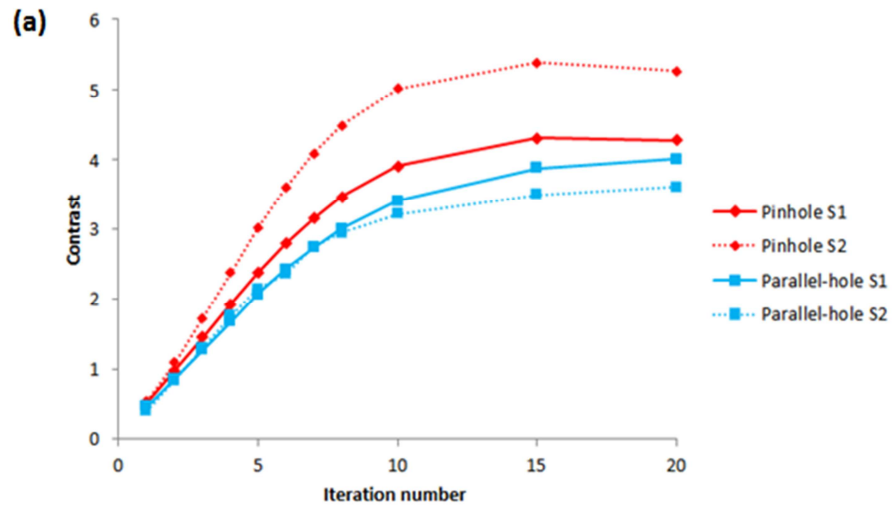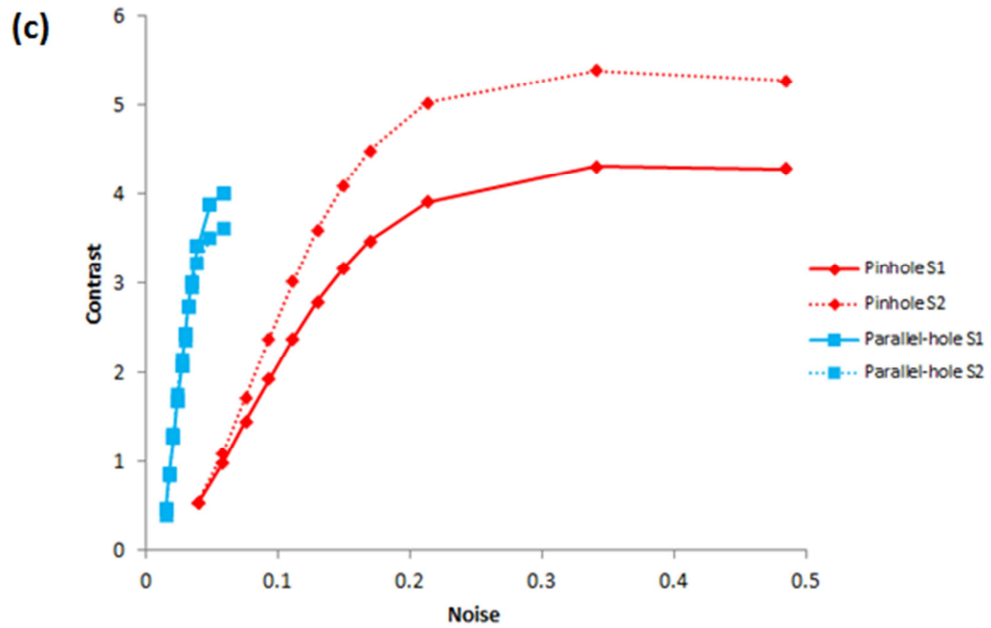
Figure 73: (a) Contrast vs. iteration, (b) noise vs. iteration, and (c) contrast vs. noise for pinhole and parallel-hole images. In (c), the iteration number increases from left to right.

Figure 74 shows the RORs at every detector angle for pinhole and parallel-hole detectors. Angle zero is at left side of the phantom. Plotted in Figure 75Figure 75 is the log-sensitivity versus resolution over these RORs. The pinhole detector resolution of the specific trajectory used in this paper is better than that of parallel-hole detector, but sensitivity of pinhole detector is lower.
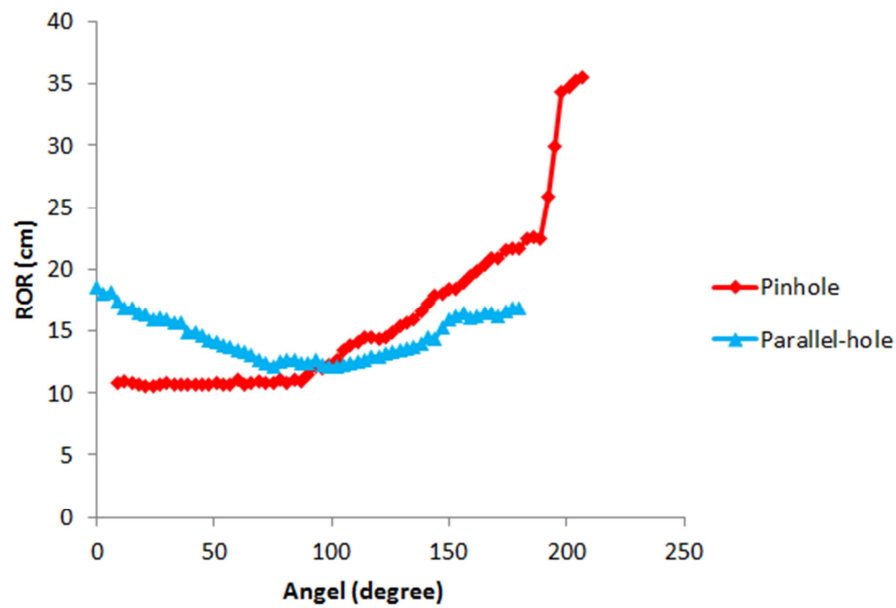
Figure 74: ROR vs. detector angle for pinhole and parallel-hole detector. The zero degree angle is at the left side of the phantom.
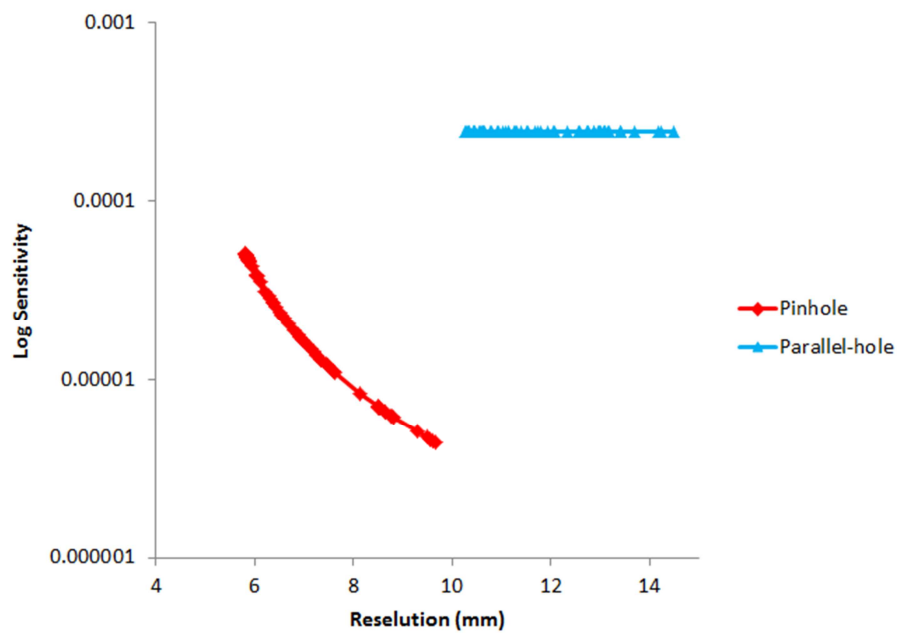
Figure 75: Log-sensitivity vs. resolution for pinhole and parallel-hole detectors over the range of RORs utilized during the SPECT scans. RORs increase from left to right.

8.3.4 Discussion

The experiments of this paper demonstrate a robot maneuvering a gamma camera about a phantom that is on a radiation-therapy flat-top table. The experiments support the proposal that robotic SPECT could provide functional and molecular imaging as patients are in position for radiation therapy. As shown in Figure 70, the robot was versatile in positioning the detector system close to, but not in collision with, the patient table, so as to minimize the distance between the detector collimator and the detector center of rotation. The robot implemented two cases of ROI imaging – a broader ROI for parallel-hole imaging and a smaller ROI for pinhole imaging. As shown in our computer-simulation studies[27] and other studies[17, 20, 108], ROI imaging can be effective at improving image quality within the ROI. Notably, ROI imaging may be particularly relevant to radiation therapy, especially on-board SPECT imaging, since the approximate tumor location is known from the planning CT or CBCT.

In this study, with the robot bolted to the floor, detector maneuverability was versatile enough for pinhole ROI imaging and broad cross-section parallel-hole imaging. Even for an ROI on the phantom side distal to the robot, the robot could maneuver the pinhole detector so as to enclose the ROI central plane in the convex hull of the pinhole trajectory. That noted, as shown in Figure 70 the first stop of the pinhole detector on the distal side of the phantom is at the mechanical limit of the robot, and the inability to achieve additional pinhole positions on the distal side of the phantom necessitates the

161

large-ROR pinhole positions on the proximal phantom side, shown in Figure 70(c). Hence while the robot shows substantial capability, limitations in detector maneuverability are also apparent. In previous computer-aided design (CAD) work we have shown that a robot mounted on a rail could provide more versatile detector motion, as illustrated in Figs. 2 and 1 of references[27, 114], respectively.

The pinhole diameter used here, 3 mm, was the largest available, and better pinhole imaging results might have been obtained with a larger pinhole. The intrinsic detector resolution is about 3.25 mm and the average magnification was about 1. Given the strong contribution of intrinsic detector resolution to total gamma camera resolution, use of a larger pinhole may have improved pinhole efficiency more substantially than it degraded total system spatial resolution. The poor sensitivity of the 3mm pinhole is reflected in the much greater noise levels seen in the pinhole images and noise measurements, and this poor sensitivity is confirmed by the analytic calculations of Figure 75. Hence a larger pinhole might have provided better resolution and sensitivity tradeoffs, and the results here likely do not reflect the full potential of pinhole ROI imaging. The results do however demonstrate the ability of a robotic SPECT system to achieve the π-plus-fan-angle short-scan conditions[155] for acquiring all line integrals through the ROI central plane, accomplishing this for an off-center ROI and in the presence of a radiation therapy flat-top. The robot is also demonstrated to be effective at maneuvering a compact parallel-hole collimated detector in the vicinity of the flat-top.

The images, profiles, and contrast and noise curves reflect this SPECT imaging capability of the robotic approach.

In conventional gantry-based SPECT, detector pose might be given by one rotation angle and an angle-dependent ROR. These angles and RORs would be provided by hardware components of the SPECT gantry and would be utilized for SPECT image reconstruction. Commercial robots typically report a more complex set of coordinates, obtained by hardware components of the robot. The study here shows that these coordinates can be harnessed for SPECT image reconstruction. Because of their wide use in industry for precision tasks, economies of scale and market competition have made robots versatile and precise while also moderately priced. Commercial robots thus present a cost-effective opportunity for expanding the capabilities of SPECT imaging. It is pertinent then that the present study demonstrates the ability of general-purpose commercial robots to provide coordinates that can be transformed into those needed for SPECT image reconstruction.

One specific test for SPECT imaging is the center of rotation (COR) correction[47]. This test is to ensure that the mechanical center of rotation of the system coincides with the COR of the projection data. The misalignment can be caused by detector sags or wobbles during rotation which results in blurring or ring artifacts in the reconstructed images. Procedure for COR correction are considered in references[47, 156, 157]. For our

robotic SPECT system, the COR (x_det) can be estimated from the line source alignment method discussed in Chapter 5.

Here, in the absence of a CBCT or LINAC in the robot laboratory, the initial base coordinate frame was calibrated to align with the flat-top table surface and edges. A CT scan of the phantom was used to determine the shift needed to define a new base coordinate frame with origin at a user-intended location in the phantom. For robotic SPECT imaging at a LINAC with CBCT, the initial base coordinate frame could be calibrated to align with that of the LINAC and CBCT, and onboard CBCT images could be used to determine the shift needed to define a new base coordinate frame with origin at the clinician-intended location in the patient.

Before and after imaging, the robot retracted the SPECT system fully away from the flat-top, as it would also when installed in a LINAC vault, thereby allowing for normal, unhampered operation of the radiation therapy system.

8.3.5 Conclusions

Robotic SPECT was investigated by integrating a gamma camera with a commercial robot. The experiments demonstrated the abilities of a robotic arm to achieve needed detector trajectory range and ROI coverage while maintaining close proximity to the phantom and avoiding collisions. It was shown that inherent robot coordinate frames can be utilized to estimate detector pose for use in SPECT image

reconstruction. This study supports the proposal that robotic SPECT could provide on-board functional and molecular imaging for patients in position for radiation therapy on a standard flat-top table.

Appendix A: Robot Operation Guideline for the Robot Lab in RP-II, Room 0114

I. Robot Startup

1. If the pitch fork is not attached to the robot, verify that the controller cabinet switch is off (down) and then attach the pitch fork.

2. Turn on robot main switch on the wall

3. Turn on cabinet switch

4. Use the blue button to select the window

5. Acknowledge all

II. Mastering Test

1. Change login to expert

2. Configure →user group→log on →"Expert"→log on →password (kuka)→log on

3. Select R1\TP\SafeRobot\MasRefReq.SRC

4. Edit→select→select w/o parameters

5. Operate in T1 mode

6. Execute program

7. Hold white button until "I" turns green→ "start key required'

8. Press the "three people" button

9. Press and hold white button, then press and hold green button → "R" turns green → BCO reached

10. Continue hold white button and press and hold green button → execute each line until "R" turns black

11. If the mastering test is failed, the message will be "mastering test failed". Do Not proceed to brake test. Redo mastering test until pass.

12. Cancel program

III. Brake Test

1. Change mode to Auto

2. Change login to expert

3. Configure →use group→log on →"Expert"→log on →password (kuka)→log on

4. Select and run R1\TP\SafeRobot\BrakeTestReq.SRC

5. Edit→select→select w/o parameters

6. Execute program

7. Press drive on green button on the top right corner→"I" turns green→"start key required"

8. Press and hold green button→ need to acknowledge

9. Press and hold green button →BCO reached

10. Verify nobody inside fence

11. Press and hold green button, and will see message

12. Brake A1, A2, A3 OK

13. Holding torque for A4, A5, A6 reached

14. Brake test successful

15. Press drives off button

16. Cancel program

17. Go back to T1 mode

IV. Shutdown Procedures

1. Remove any payload from the robot so that the pitch fork can be attached on

start up

2. Move the robot back to the home position

    A1 0degree

    A2 -137.52cm

    A3 137.26cm

    A4, A5 and A6 0degree

3. Turn off the switch on cabinet

4. Pad lock the cabinet switch in Off position

5. Turn off robot main switch on the wall

6. Return pendant cable to cable rack on the controller

V. If a Collision Occurs

1. Operating in T1 mode only, run the daily mastering test. Do not proceed

further unless the robot passes the mastering test.

2. Inform Dr. Bowsher or Dr. Yin before proceeding

References

1   C.C. Ling, J. Humm, S. Larson, H. Amols, Z. Fuks, S. Leibel, J.A. Koutcher, "Towards multidimensional radiotherapy (MD-CRT): biological imaging and biological conformality," International Journal of Radiation Oncology* Biology* Physics **47**, 551-560 (2000).

2   I.C.o.R.U.a. Measurements, "ICRU Report 50. Prescribing, recording, and reporting photon beam therapyICRU, Bethesda, MD," 1993).

3   I.C.o.R.U.a. Measurements, "ICRU Report 62. Prescribing, recording, and reporting photon beam therapy (Supplement to ICRU Report 50)ICRU, Bethesda, MD," 1999).

4   H. Zaidi, I. El Naqa, "PET-guided delineation of radiation therapy treatment volumes: a survey of image segmentation techniques," European journal of nuclear medicine and molecular imaging **37**, 2165-2187 (2010).

5   D. Schinagl, J. Kaanders, W. Oyen, "From anatomical to biological target volumes: the role of PET in radiation treatment planning," Cancer Imaging **6**, S107 (2006).

6   S. Mutic, R.S. Malyapa, P.W. Grigsby, F. Dehdashti, T.R. Miller, I. Zoberi, W.R. Bosch, J. Esthappan, D.A. Low, "PET-guided IMRT for cervical carcinoma with positive para-aortic lymph nodes—a dose-escalation treatment planning study," International Journal of Radiation Oncology* Biology* Physics **55**, 28-35 (2003).

7   C. Gillham, D. Zips, F. Pönisch, C. Evers, W. Enghardt, N. Abolmaali, K. Zöphel, S. Appold, T. Hölscher, J. Steinbach, "Additional PET/CT in week 5–6 of radiotherapy for patients with stage III non-small cell lung cancer as a means of dose escalation planning?," Radiotherapy and Oncology **88**, 335-341 (2008).

8   J. Hoang, S. Das, K. Choudhury, D. Yoo, D. Brizel, "Using FDG-PET to measure early treatment response in head and neck squamous cell carcinoma: quantifying intrinsic variability in order to understand treatment-induced change," American Journal of Neuroradiology **34**, 1428-1433 (2013).

⁹ L. Xing, B. Thorndyke, E. Schreibmann, Y. Yang, T.-F. Li, G.-Y. Kim, G. Luxton, A. Koong, "Overview of image-guided radiation therapy," Medical Dosimetry **31**, 91-112 (2006).

¹⁰ J.-P. Bissonnette, P.A. Balter, L. Dong, K.M. Langen, D.M. Lovelock, M. Miften, D.J. Moseley, J. Pouliot, J.-J. Sonke, S. Yoo, "Quality assurance for image-guided radiation therapy utilizing CT-based technologies: A report of the AAPM TG-179," Medical Physics **39**, 1946 (2012).

¹¹ R.A. Vogel, D. Kirch, M. LeFree, P. Steele, "New method of multiplanar emission tomography using a seven pinhole collimator and an Anger scintillation camera," J. Nucl. Med.;(United States) **19**1978).

¹² W. Chang, R.E. Henkin, "Seven-pinhole multigated tomography and its application to blood-pool imaging: technical parameters," J. Nucl. Med.;(United States) **21**1980).

¹³ RB Grove, A Rodewald, R. Bell, "Application of multiple pinhole emission radionuclide tomography to imaging of the brain and thyroid," J Nucl Med **21**1980).

¹⁴ FH. Deland, EE. Kim, P. Domstad, "Contributions of the seven pinhole collimator to cisternography," Journal of Nuclear Medicine **21**, 88 (1980).

¹⁵ Bruce Hasegawa, Dennis Kirch, David Stern, Michael Adams, Joel Sklar, Timothy Johnson, P. Steele, "Single-Photon EmissionTomography with a 12-Pinhole Collimator," J Nuci Med **23**, 606-612 (1982).

¹⁶ M. Ivanovic, D. Weber, S. Loncaric, presented at the Nuclear Science Symposium, 1997. IEEE1997 (unpublished).

¹⁷ T. Funk, D.L. Kirch, J.E. Koss, E. Botvinick, B.H. Hasegawa, "A novel approach to multipinhole SPECT for myocardial perfusion imaging," Journal of Nuclear Medicine **47**, 595-602 (2006).

18   B.J. Min, Y. Choi, N.-Y. Lee, K. Lee, Y.B. Ahn, J. Joung, "Design consideration of a multipinhole collimator with septa for ultra high-resolution silicon drift detector modules," Nuclear Instruments and Methods in Physics Research Section A: Accelerators, Spectrometers, Detectors and Associated Equipment **606**, 755-761 (2009).

19   J.D. Bowen, Q. Huang, G.T. Gullberg, Y. Seo, presented at the Nuclear Science Symposium Conference Record (NSS/MIC), 2010 IEEE2010 (unpublished).

20   E.V. Garcia, T.L. Faber, F.P. Esteves, "Cardiac dedicated ultrafast SPECT cameras: New designs and clinical implications," Journal of Nuclear Medicine **52**, 210-217 (2011).

21   F.J. Beekman, B. Vastenhouw, "Design and simulation of a high-resolution stationary SPECT system for small animals," Physics in medicine and biology **49**, 4579 (2004).

22   T. Funk, P. Després, W.C. Barber, K.S. Shah, B.H. Hasegawa, "A multipinhole small animal SPECT system with submillimeter spatial resolution," Medical physics **33**, 1259 (2006).

23   N. Schramm, G. Ebel, U. Engeland, T. Schurrat, M. Behe, T. Behr, "High-resolution SPECT using multipinhole collimation," Nuclear Science, IEEE Transactions on **50**, 315-320 (2003).

24   G.T. GULLBERG, P.E. CHRISTIAN, G.L. ZENG, F.L. DATZ, H.T. MORGAN, "Cone beam tomography of the heart using single-photon emission-computed tomography," Investigative radiology **26**, 681-688 (1991).

25   R.J. Jaszczak, C.E. Floyd Jr, S.H. Manglos, K.L. Greer, R.E. Coleman, "Cone beam collimation for single photon emission computed tomography: analysis, simulation, and image reconstruction using filtered backprojection," Medical physics **13**, 484-489 (1986).

26   R.J. Jaszczak, K.L. Greer, R.E. Coleman, "SPECT using a specially designed cone beam collimator," J Nucl Med **29**, 1398-1405 (1988).

27   J. Bowsher, S. Yan, J. Roper, W. Giles, F.-F. Yin, "Onboard functional and molecular imaging: A design investigation for robotic multipinhole SPECT," Medical physics **41**, 010701 (2014).

28   H.P. Rodemann, "Molecular radiation biology: perspectives for radiation oncology," Radiotherapy and oncology **92**, 293-298 (2009).

29   S.K. Das, R.K. Ten Haken, presented at the Seminars in radiation oncology2011 (unpublished).

30   M. Höckel, P. Vaupel, "Tumor hypoxia: definitions and current clinical, biologic, and molecular aspects," Journal of the National Cancer Institute **93**, 266-276 (2001).

31   D. Thorwarth, S.-M. Eschmann, F. Paulsen, M. Alber, "Hypoxia dose painting by numbers: a planning study," International Journal of Radiation Oncology* Biology* Physics **68**, 291-300 (2007).

32   S.M. Bentzen, V. Gregoire, presented at the Seminars in radiation oncology2011 (unpublished).

33   B.A. Hoeben, J. Bussink, E.G. Troost, W.J. Oyen, J.H. Kaanders, "Molecular PET imaging for biology-guided adaptive radiotherapy of head and neck cancer," Acta Oncologica **52**, 1257-1271 (2013).

34   D.L. Schwartz, A.S. Garden, J. Thomas, Y. Chen, Y. Zhang, J. Lewin, M.S. Chambers, L. Dong, "Adaptive radiotherapy for head-and-neck cancer: initial clinical outcomes from a prospective trial," International Journal of Radiation Oncology* Biology* Physics **83**, 986-993 (2012).

35   B.F. Hutton, M. Braun, L. Thurfjell, D.Y. Lau, "Image registration: an essential tool for nuclear medicine," European journal of nuclear medicine and molecular imaging **29**, 559-577 (2002).

36   T. Beyer, D.W. Townsend, T. Brun, P.E. Kinahan, M. Charron, R. Roddy, J. Jerin, J. Young, L. Byars, R. Nutt, "A combined PET/CT scanner for clinical oncology," Journal of nuclear medicine **41**, 1369-1379 (2000).

37   G. Mariani, L. Bruselli, T. Kuwert, E.E. Kim, A. Flotats, O. Israel, M. Dondi, N. Watanabe, "A review on the clinical uses of SPECT/CT," European journal of nuclear medicine and molecular imaging **37**, 1959-1985 (2010).

38   G. Antoch, F.M. Vogt, L.S. Freudenberg, F. Nazaradeh, S.C. Goehde, J. Barkhausen, G. Dahmen, A. Bockisch, J.F. Debatin, S.G. Ruehm, "Whole-body dual-modality PET/CT and whole-body MRI for tumor staging in oncology," JAMA: the journal of the American Medical Association **290**, 3199-3206 (2003).

39   M. Ishikawa, S. Yamaguchi, S. Tanabe, G. Bengua, K. Sutherland, R. Suzuki, N. Miyamoto, K. Nishijima, N. Katoh, H. Shirato, "Conceptual Design of PET-linac System for Molecular-guided Radiotherapy," International Journal of Radiation Oncology* Biology* Physics **78**, S674 (2010).

40   N. Darwish, T. Mackie, C. Kao, B. Thomadsen, "TU-C-214-12: On-Board PET with Tomotherapy Using Open Dual Ring Geometry with Consideration to DOI Effect," Medical Physics **38**, 3758 (2011).

41   J.J. Lagendijk, B.W. Raaymakers, A.J. Raaijmakers, J. Overweg, K.J. Brown, E.M. Kerkhof, R.W. van der Put, B. Hårdemark, M. van Vulpen, U.A. van der Heide, "MRI/linac integration," Radiotherapy and Oncology **86**, 25-29 (2008).

42   J.E. Bowsher, S. Yan, J.R. Roper, W.M. Giles, F.-F. Yin, "Onboard Functional and Molecular Imaging: A Design Investigation for Robotic Multi-Pinhole SPECT," Medical physics **41**(2014).

43   J.E. Bowsher, J.R. Roper, S. Yan, W.M. Giles, F.-F. Yin, "Regional SPECT imaging using sampling Principles and Multiple Pinholes," in *Nuclear Science Symposium Conference Record (NSS/MIC), 2010 IEEE* (IEEE, 2010), pp. 2071-2076.

44   S. Yan, J.E. Bowsher, F.-F. Yin, "A Line-Source Method for Aligning On-board and other Pinhole SPECT Systems," Accepted Medical Physics **40**(2013).

45   J.H. Hubbell, S.M. Seltzer, "Tables of X-ray mass attenuation coefficients and mass energy-absorption coefficients 1 keV to 20 MeV for elements Z= 1 to 92 and 48 additional substances of dosimetric interest," (National Inst. of Standards and Technology-PL, Gaithersburg, MD (United States). Ionizing Radiation Div., 1995).

46   Digirad, "2020tc Imager."

47   S.R. Cherry, J.A. Sorenson, M.E. Phelps, *Physics in nuclear medicine*. (Elsevier Health Sciences, 2003).

48   S.D. Metzler, J.E. Bowsher, M.F. Smith, R.J. Jaszczak, "Analytic determination of pinhole collimator sensitivity with penetration," Medical Imaging, IEEE Transactions on **20**, 730-741 (2001).

49   R. Accorsi, S.D. Metzler, "Analytic determination of the resolution-equivalent effective diameter of a pinhole collimator," Medical Imaging, IEEE Transactions on **23**, 750-763 (2004).

50   J.H. Hubbell, S.M. Seltzer, "Tables of x-ray mass attenuation coefficients and mass energy-absorption coefficients," National Institute of Standards and Technology1996).

51   M.B. Williams, A.R. Goode, V. Galbis-Reig, S. Majewski, A.G. Weisenberger, R. Wojcik, "Performance of a PSPMT based detector for scintimammography," Physics in medicine and biology **45**, 781 (2000).

52   G.T. Gullberg, B.M.W. Tsui, C.R. Crawford, J.G. Ballard, J.T. Hagius, "Estimation of geometrical parameters and collimator evaluation for cone beam tomography," Med. Phys **17**, 264-272 (1990).

53   P. Rizo, P. Grangeat, R. Guillemaud, "Geometric calibration method for multiple-head cone-beam SPECT system," Nuclear Science, IEEE Transactions on **41**, 2748-2757 (1994).

54   K.J. Kyriakopoulos, P. Yiannakos, V. Kallipolites, K. Domales, "A geometric calibration methodology for single-head cone-beam x-ray systems," Journal of Intelligent and Robotic Systems **24**, 151-174 (1999).

55   F. Noo, R. Clackdoyle, C. Mennessier, T.A. White, T.J. Roney, "Analytic method based on identification of ellipse parameters for scanner calibration in cone-beam tomography," Physics in medicine and biology **45**, 3489 (2000).

56   D. Beque, J. Nuyts, G. Bormans, P. Suetens, P. Dupont, "Characterization of pinhole SPECT acquisition geometry," Medical Imaging, IEEE Transactions on **22**, 599-612 (2003).

57   S. Metzler, K. Greer, R. Jaszczak, "Determination of mechanical and electronic shifts for pinhole SPECT using a single point source," Medical Imaging, IEEE Transactions on **24**, 361-370 (2005).

58   Y. Wang, B.M.W. Tsui, "Pinhole SPECT with different data acquisition geometries: Usefulness of unified projection operators in homogeneous coordinates," Medical Imaging, IEEE Transactions on **26**, 298-308 (2007).

59   D. Bequé, C. Vanhove, A. Andreyev, J. Nuyts, M. Defrise, "Correction for imperfect camera motion and resolution recovery in pinhole SPECT," IEEE Nuclear Science Symposium Conference Record **4**, 2507-2510 Vol. 2504 (2004).

60   S. Metzler, R. Jaszczak, K. Greer, J. Bowsher, "Angular-dependent axial-shift correction for pinhole SPECT," Nuclear Science, IEEE Transactions on **54**, 124-129 (2007).

61   M. Defrise, C. Vanhove, J. Nuyts, "Perturbative refinement of the geometric calibration in pinhole SPECT," Medical Imaging, IEEE Transactions on **27**, 204-214 (2008).

62   R. Zhou, T. Ma, Y. Liu, X. Sun, X. Kang, Z. Wu, S. Wang, Y. Jing, J. Cheng, "Calibration of pinhole microSPECT system using line sources," IEEE Nuclear Science Symposium Conference Record **5**, 3364-3367 (2007).

63   T. MathWorks, "Optimization Toolbox User's Guide R2011b."

64   S. Metzler, J.E. Bowsher, M. Smith, R.J. Jaszczak, "Analytic determination of pinhole collimator sensitivity with penetration," Medical Imaging, IEEE Transactions on **20**, 730-741 (2001).

65   T. MathWorks, "Statistics Toolbox For Use with MATLAB User's Guide Version 4."

66   M. KUKA Robotics Corporation (Shelby Township, "KUKA Basic Programming Manual."

67   H. Kim, L.R. Furenlid, M.J. Crawford, D.W. Wilson, H.B. Barber, T.E. Peterson, W.C. Hunter, Z. Liu, J.M. Woolfenden, H.H. Barrett, "SemiSPECT: a small-animal single-photon emission computed tomography (SPECT) imager based on eight cadmium zinc telluride (CZT) detector arrays," Medical physics **33**, 465 (2006).

68   T.A. White, T.J. Roney, R.J. Pink, F. Noo, R. Clackdoyle, M. Smith, W.F. Jones, presented at the SPIE's International Symposium on Optical Science, Engineering, and Instrumentation1999 (unpublished).

69   A. Jemal, F. Bray, M.M. Center, J. Ferlay, E. Ward, D. Forman, "Global cancer statistics," CA: a cancer journal for clinicians **61**, 69-90 (2011).

70   B. Fisher, S. Anderson, J. Bryant, R.G. Margolese, M. Deutsch, E.R. Fisher, J.-H. Jeong, N. Wolmark, "Twenty-year follow-up of a randomized trial comparing total mastectomy, lumpectomy, and lumpectomy plus irradiation for the treatment of invasive breast cancer," New England Journal of Medicine **347**, 1233-1241 (2002).

71   A.U. Schratter-Sehn, "Breast cancer radiotherapy," HAMDAN MEDICAL JOURNAL **5**, 51–56 (2012).

72   E.B.C.T.C. Group, "Effect of radiotherapy after breast-conserving surgery on 10-year recurrence and 15-year breast cancer death: meta-analysis of individual patient data for 10 801 women in 17 randomised trials," Lancet **378**, 1707 (2011).

73   H. Bartelink, J.-C. Horiot, P.M. Poortmans, H. Struikmans, W. Van den Bogaert, A. Fourquet, J.J. Jager, W.J. Hoogenraad, S.B. Oei, C.C. Wárlám-Rodenhuis, "Impact of a higher radiation dose on local control and survival in breast-conserving therapy of early breast cancer: 10-year results of the randomized boost versus no boost EORTC 22881-10882 trial," Journal of Clinical Oncology **25**, 3259-3265 (2007).

74   M.D. den Hartogh, M.E. Philippens, I.E. van Dam, C.E. Kleynen, R.J. Tersteeg, R.M. Pijnappel, A.N. Kotte, H.M. Verkooijen, M.A. van den Bosch, M. van Vulpen, "MRI and CT imaging for preoperative target volume delineation in breast-conserving therapy," Radiation Oncology **9**, 63 (2014).

75   M. Palta, S. Yoo, J.D. Adamson, L.R. Prosnitz, J.K. Horton, "Preoperative single fraction partial breast radiotherapy for early-stage breast cancer," International Journal of Radiation Oncology* Biology* Physics **82**, 37-42 (2012).

76   C. Polgár, J. Fodor, T. Major, G. Németh, K. Lövey, Z. Orosz, Z. Sulyok, Z. Takácsi-Nagy, M. Kásler, "Breast-conserving treatment with partial or whole breast irradiation for low-risk invasive breast carcinoma—5-year results of a randomized trial," International Journal of Radiation Oncology* Biology* Physics **69**, 694-702 (2007).

77   P.R. Benitez, M.E. Keisch, F. Vicini, A. Stolier, T. Scroggins, A. Walker, J. White, P. Hedberg, M. Hebert, D. Arthur, "Five-year results: the initial clinical trial of MammoSite balloon brachytherapy for partial breast irradiation in early-stage breast cancer," The American Journal of Surgery **194**, 456-462 (2007).

78   F.A. Vicini, P. Chen, M. Wallace, C. Mitchell, Y. Hasan, I. Grills, L. Kestin, S. Schell, N.S. Goldstein, J. Kunzman, "Interim cosmetic results and toxicity using 3D conformal external beam radiotherapy to deliver accelerated partial breast irradiation in patients with early-stage breast cancer treated with breast-conserving therapy," International Journal of Radiation Oncology* Biology* Physics **69**, 1124-1130 (2007).

79   B.D. Smith, D.W. Arthur, T.A. Buchholz, B.G. Haffty, C.A. Hahn, P.H. Hardenbergh, T.B. Julian, L.B. Marks, D.A. Todor, F.A. Vicini, "Accelerated partial breast irradiation consensus statement from the American Society for

Radiation Oncology (ASTRO)," International Journal of Radiation Oncology* Biology* Physics **74**, 987-1001 (2009).

80   J.S. Vaidya, D.J. Joseph, J.S. Tobias, M. Bulsara, F. Wenz, C. Saunders, M. Alvarado, H.L. Flyger, S. Massarut, W. Eiermann, "Targeted intraoperative radiotherapy versus whole breast radiotherapy for breast cancer (TARGIT-A trial): an international, prospective, randomised, non-inferiority phase 3 trial," The Lancet **376**, 91-102 (2010).

81   C. Vrieling, L. Collette, A. Fourquet, W.J. Hoogenraad, J.-C. Horiot, J.J. Jager, M. Pierart, P.M. Poortmans, H. Struikmans, B. Maat, "The influence of patient, tumor and treatment factors on the cosmetic results after breast-conserving therapy in the EORTC 'boost vs. no boost'trial," Radiotherapy and Oncology **55**, 219-232 (2000).

82   S. Collette, L. Collette, T. Budiharto, J.-C. Horiot, P.M. Poortmans, H. Struikmans, W. Van den Bogaert, A. Fourquet, J.J. Jager, W. Hoogenraad, "Predictors of the risk of fibrosis at 10 years after breast conserving therapy for early breast cancer– A study based on the EORTC trial 22881–10882 'boost< i> versus</i> no boost'," European Journal of Cancer **44**, 2587-2599 (2008).

83   R.K. Benda, G. Yasuda, A. Sethi, S.G. Gabram, R.W. Hinerman, N.P. Mendenhall, "Breast boost: are we missing the target?," Cancer **97**, 905-909 (2003).

84   M. den Hartogh, B. van Asselen, E. Monninkhof, M. van den Bosch, M. van Vulpen, P. van Diest, K. Gilhuijs, A. Witkamp, L. van de Bunt, W. Mali, "Excised and irradiated volumes in relation to the tumor size in breast-conserving therapy," Breast cancer research and treatment **129**, 857-865 (2011).

85   J.T. Hepel, M. Tokita, S.G. MacAusland, S.B. Evans, J.R. Hiatt, L.L. Price, T. DiPetrillo, D.E. Wazer, "Toxicity of three-dimensional conformal radiotherapy for accelerated partial breast irradiation," International Journal of Radiation Oncology* Biology* Physics **75**, 1290-1296 (2009).

86   R. Jagsi, M.A. Ben-David, J.M. Moran, R.B. Marsh, K.A. Griffith, J.A. Hayman, L.J. Pierce, "Unacceptable cosmesis in a protocol investigating intensity-modulated radiotherapy with active breathing control for accelerated partial-

breast irradiation," International Journal of Radiation Oncology* Biology* Physics **76**, 71-78 (2010).

87   H. Chaudhry, A.L. Hanlon, S.B. Kesmodel, E.C. Bellavance, K.H. Tkaczuk, C.L. Drogula, W.K. Citron, R.J. Cohen, W.F. Regine, S.J. Feigenberg, "A Prospective Trial of Preoperative Accelerated Partial Breast Irradiation (APBI): Predictors of Asymptomatic and Symptomatic Seroma Formation," Int J Radiat Oncol Biol Phys **87**, S215-S216 (2013).

88   E.M. Nichols, A.A. Dhople, M.M. Mohiuddin, T.W. Flannery, C.X. Yu, W.F. Regine, "Comparative analysis of the post-lumpectomy target volume versus the use of pre-lumpectomy tumor volume for early-stage breast cancer: implications for the future," International Journal of Radiation Oncology* Biology* Physics **77**, 197-202 (2010).

89   C.B. Hruska, M.K. O'Connor, "Nuclear imaging of the breast: Translating achievements in instrumentation into clinical use," Medical physics **40**, 050901 (2013).

90   S.C. Formenti, M.T. Truong, J.D. Goldberg, V. Mukhi, B. Rosenstein, D. Roses, R. Shapiro, A. Guth, J.K. Dewyngaert, "Prone accelerated partial breast irradiation after breast-conserving surgery: preliminary clinical results and dose–volume histogram analysis," International Journal of Radiation Oncology* Biology* Physics **60**, 493-504 (2004).

91   S.C. Formenti, H. Hsu, M. Fenton-Kerimian, D. Roses, A. Guth, G. Jozsef, J.D. Goldberg, J.K. DeWyngaert, "Prone accelerated partial breast irradiation after breast-conserving surgery: five-year results of 100 patients," International Journal of Radiation Oncology* Biology* Physics2012).

92   J. Buijsen, J.J. Jager, J. Bovendeerd, R. Voncken, J.H. Borger, L.J. Boersma, L.H. Murrer, P. Lambin, "Prone breast irradiation for pendulous breasts," Radiotherapy and oncology **82**, 337-340 (2007).

93   L.F. Paszat, W.J. Mackillop, P.A. Groome, K. Schulze, E. Holowaty, "Mortality from myocardial infarction following postlumpectomy radiotherapy for breast

cancer: a population-based study in Ontario, Canada," International Journal of Radiation Oncology* Biology* Physics **43**, 755-762 (1999).

94   L.F. Paszat, W.J. Mackillop, P.A. Groome, C. Boyd, K. Schulze, E. Holowaty, "Mortality from myocardial infarction after adjuvant radiotherapy for breast cancer in the surveillance, epidemiology, and end-results cancer registries," Journal of clinical oncology **16**, 2625-2631 (1998).

95   M. Deutsch, S.R. Land, M. Begovic, H.S. Wieand, N. Wolmark, B. Fisher, "The incidence of lung carcinoma after surgery for breast carcinoma with and without postoperative radiotherapy," Cancer **98**, 1362-1368 (2003).

96   A.M. Kirby, P.M. Evans, E.M. Donovan, H.M. Convery, J.S. Haviland, J.R. Yarnold, "Prone versus supine positioning for whole and partial-breast radiotherapy: a comparison of non-target tissue dosimetry," Radiotherapy and Oncology **96**, 178-184 (2010).

97   S. Yoo, R. Blitzblau, F. Yin, J.K. Horton, "Comparison of pre-operative partial breast radiosurgery treatment techniques: 3D CRT, non-coplanar IMRT, coplanar IMRT, and VMAT," Int J Radiat Oncol Biol Phys **87**, S215 (2013).

98   P. La Riviere, X. Pan, B. Penney, "Ideal-observer analysis of lesion detectability in planar, conventional SPECT, and dedicated SPECT scintimammography using effective multi-dimensional smoothing," Nuclear Science, IEEE Transactions on **45**, 1273-1279 (1998).

99   S. Majewski, D. Kieper, E. Curran, C. Keppel, B. Kross, A. Palumbo, V. Popov, A. Wisenberger, B. Welch, R. Wojcik, "Optimization of dedicated scintimammography procedure using detector prototypes and compressible phantoms," Nuclear Science, IEEE Transactions on **48**, 822-829 (2001).

100   B.C. Pieper, J.E. Bowsher, M.P. Tornai, G. Peter, K. Greer, R.J. Jaszczak, "Breast tumor imaging using a tiltable head SPECT camera," Nuclear Science, IEEE Transactions on **48**, 1477-1482 (2001).

101   M.P. Tornai, J.E. Bowsher, C.N. Archer, J. Peter, R.J. Jaszczak, L.R. MacDonald, B.E. Patt, J.S. Iwanczyk, "A 3D gantry single photon emission tomograph with hemispherical coverage for dedicated breast imaging," Nuclear Instruments and Methods in Physics Research Section A: Accelerators, Spectrometers, Detectors and Associated Equipment **497**, 157-167 (2003).

102   H. Wang, C. Scarfone, K. Greer, R. Coleman, R. Jaszczak, "Prone breast tumor imaging using vertical axis-of-rotation (VAOR) SPECT systems: an initial study," Nuclear Science, IEEE Transactions on **44**, 1271-1276 (1997).

103   W.H. Baird, E.C. Frey, B.M. Tsui, Y. Wang, D.E. Wessell, "Evaluation of rotating slant-hole SPECT mammography using Monte Carlo simulation methods," Nuclear Science, IEEE Transactions on **50**, 105-109 (2003).

104   K.V. Bobkov, J.E. Bowsher, K.L. Greer, R.J. Jaszczak, K.E. Braun, T.J. Lee, "Phantom assessment of new acquisition geometries for breast pinhole SPECT imaging," Nuclear Science, IEEE Transactions on **53**, 1162-1167 (2006).

105   C. Scarfone, R. Jaszczak, J. Li, M. Soo, M. Smith, K. Greer, R. Coleman, "Breast tumour imaging using incomplete circular orbit pinhole SPET: a phantom study," Nuclear medicine communications **18**, 1077 (1997).

106   L. Moliner, A. González, A. Soriano, F. Sánchez, C. Correcher, A. Orero, M. Carles, L. Vidal, J. Barberá, L. Caballero, "Design and evaluation of the MAMMI dedicated breast PET," Medical physics **39**, 5393-5404 (2012).

107   A. Seret, "Will high-resolution/high-sensitivity SPECT ensure that PET is not the only survivor in nuclear medicine during the next decade?," European journal of nuclear medicine and molecular imaging **36**, 533-535 (2009).

108   M.U. Zaman, I. Hashmi, N. Fatima, "Recent developments and future prospects of SPECT myocardial perfusion imaging," Annals of nuclear medicine **24**, 565-569 (2010).

¹⁰⁹ E.G. DePuey, "Advances in SPECT camera software and hardware: currently available and new on the horizon," Journal of nuclear cardiology **19**, 551-581 (2012).

¹¹⁰ W. Segars, G. Sturgeon, S. Mendonca, J. Grimes, B. Tsui, "4D XCAT phantom for multimodality imaging research," Medical physics **37**, 4902 (2010).

¹¹¹ J.-P.D.B. Poppe, N. Chofor, A. Rühmann, W. Kunth, A. Djouguela, R. Kollhoff, K.C. Willborn, "The effect of a carbon-fiber couch on the depth-dose curves and transmission properties for megavoltage photon beams," Strahlentherapie und Onkologie **183**, 43-48 (2007).

¹¹² J. Roper, J. Bowsher, F.-F. Yin, "Direction-dependent localization errors in SPECT images," Medical physics **37**, 4886 (2010).

¹¹³ T. Colton, *Statistis in Medicine*. (Little, Brown and Company 1974).

¹¹⁴ S. Yan, J. Bowsher, F.-F. Yin, "A line-source method for aligning on-board and other pinhole SPECT systems," Medical physics **40**, 122501 (2013).

¹¹⁵ G. Jozsef, J.K. DeWyngaert, S.J. Becker, S. Lymberis, S.C. Formenti, "Prospective study of cone-beam computed tomography image-guided radiotherapy for prone accelerated partial breast irradiation," International Journal of Radiation Oncology* Biology* Physics **81**, 568-574 (2011).

¹¹⁶ R. Siegel, D. Naishadham, A. Jemal, "Cancer statistics, 2012," CA: a cancer journal for clinicians **62**, 10-29 (2012).

¹¹⁷ O. Schillaci, "Single-photon emission computed tomography/computed tomography in lung cancer and malignant lymphoma," Seminars in nuclear medicine **36**, 275-285 (2006).

¹¹⁸ O. Schillaci, A. Spanu, G. Madeddu, "99mTc] sestamibi and [99mTc] tetrofosmin in oncology: SPET and fusion imaging in lung cancer, malignant lymphomas and brain tumors," The quarterly journal of nuclear medicine and molecular imaging: official publication of the Italian Association of Nuclear Medicine (AIMN)[and]

the International Association of Radiopharmacology (IAR),[and] Section of the Society of Radiopharmaceutical Chemistry and Biology **49**, 133 (2005).

[119]   M. Nosotti, L. Santambrogio, M. Gasparini, A. Baisi, N. Bellaviti, L. Rosso, "Role of 99mTc-hexakis-2-methoxy-isobutylisonitrile in the diagnosis and staging of lung cancer," CHEST Journal **122**, 1361-1364 (2002).

[120]   O. Schillaci, F. Monteleone, N. D'Andrea, V. Picardi, R. Cangemi, V. Cangemi, F. Scopinaro, "Technetium-99m tetrofosmin single photon emission computed tomography in the evaluation of suspected lung cancer," Cancer biotherapy & radiopharmaceuticals **14**, 129-134 (1999).

[121]   A. Spanu, F. Ginesu, P. Pirina, M.E. Solinas, O. Schillaci, A. Farris, F. Chessa, G. Madeddu, P. Marongiu, A. Falchi, "The usefulness of 99mTc-tetrofosmin SPECT in the detection of intrathoracic malignant lesions," International journal of oncology **22**, 639-649 (2003).

[122]   M. Ishibashi, T. Fujii, H. Yamana, K. Fujimoto, T. Rikimaru, A. Hayashi, S. Kurata, N. Hayabuchi, "Relationship between cancer cell proliferation and thallium-201 uptake in lung cancer," Annals of nuclear medicine **14**, 255-261 (2000).

[123]   K. Suga, N. Kume, K. Nishigauchi, N. Ogasawara, A. Hara, G. Miura, T. Matsumoto, N. Matsunaga, "201Tl SPECT as an indicator for early prediction of therapeutic effects in patients with non-small cell lung cancer," Annals of nuclear medicine **12**, 355-362 (1998).

[124]   Y. Yamamoto, Y. Nishiyama, K. Fukunaga, T. Kobayashi, K. Satoh, J. Fujita, M. Ohkawa, "Evaluation of histopathological differentiation in lung adenocarcinoma patients using 201Tl-chloride and 99Tcm-MIBI SPET," Nuclear medicine communications **22**, 539-545 (2001).

[125]   Y. Nishiyama, Y. Kawasaki, Y. Yamamoto, K. Fukunaga, K. Satoh, H. Takashima, M. Ohkawa, M. Tanabe, "Technetium-99m-MIBI and thallium-201 scintigraphy of primary lung cancer," Journal of nuclear medicine: official publication, Society of Nuclear Medicine **38**, 1358-1361 (1997).

126   E. Ikeda, J. Taki, S. Kinuya, K. Nakajima, N. Tonami, "Thallium-201 SPECT with triple-headed gamma camera for differential diagnosis of small pulmonary nodular lesion 20 mm in diameter or smaller," Annals of Nuclear Medicine **14**, 91-95 (2000).

127   F. Cuttitta, S. Rosen, A.F. Gazdar, J.D. Minna, "Monoclonal antibodies that demonstrate specificity for several types of human lung cancer," Proceedings of the National Academy of Sciences **78**, 4591-4595 (1981).

128   J. Machac, B. Krynyckyi, C. Kim, "Peptide and antibody imaging in lung cancer," in *Seminars in nuclear medicine*, *Vol. 32* (Elsevier, 2002), pp. 276-292.

129   G.W. Goerres, E. Kamel, T.-N.H. Heidelberg, M.R. Schwitter, C. Burger, G.K. von Schulthess, "PET-CT image co-registration in the thorax: influence of respiration," European journal of nuclear medicine and molecular imaging **29**, 351-360 (2002).

130   C. Cohade, M. Osman, L.T. Marshall, R.L. Wahl, "PET-CT: accuracy of PET and CT spatial registration of lung lesions," European journal of nuclear medicine and molecular imaging **30**, 721-726 (2003).

131   M.M. Osman, C. Cohade, Y. Nakamoto, L.T. Marshall, J.P. Leal, R.L. Wahl, "Clinically significant inaccurate localization of lesions with PET/CT: frequency in 300 patients," Journal of Nuclear Medicine **44**, 240-243 (2003).

132   L. Ketai, M. Hartshorne, "Potential uses of computed tomography-SPECT and computed tomography-coincidence fusion images of the chest," Clinical nuclear medicine **26**, 433-441 (2001).

133   S. Katyal, E.L. Kramer, M.E. Noz, D. McCauley, A. Chachoua, A. Steinfeld, "Fusion of immunoscintigraphy single photon emission computed tomography (SPECT) with CT of the chest in patients with non-small cell lung cancer," Cancer Research **55**, 5759s-5763s (1995).

134   C. Pérault, C. Schvartz, H. Wampach, J.-C. Liehn, M.-J. Delisle, "Thoracic and abdominal SPECT-CT image fusion without external markers in endocrine carcinomas," The Journal of nuclear medicine **38**, 1234-1242 (1997).

135   J.N. Yu, F.H. Fahey, H.D. Gage, C.G. Eades, B.A. Harkness, C.A. Pelizzari, J.W. Keyes Jr, "Intermodality, retrospective image registration in the thorax," Journal of nuclear medicine: official publication, Society of Nuclear Medicine **36**, 2333-2338 (1995).

136   P.J. Keall, G.S. Mageras, J.M. Balter, R.S. Emery, K.M. Forster, S.B. Jiang, J.M. Kapatoes, D.A. Low, M.J. Murphy, B.R. Murray, "The management of respiratory motion in radiation oncology report of AAPM Task Group 76," Medical physics **33**, 3874 (2006).

137   K. Cho, S.-i. Kumiata, S. Okada, T. Kumazaki, "Development of respiratory gated myocardial SPECT system," Journal of Nuclear Cardiology **6**, 20-28 (1999).

138   W.P. Segars, B.M. Tsui, "Study of the efficacy of respiratory gating in myocardial SPECT using the new 4-D NCAT phantom," Nuclear Science, IEEE Transactions on **49**, 675-679 (2002).

139   G. Kovalski, O. Israel, Z. Keidar, A. Frenkel, J. Sachs, H. Azhari, "Correction of heart motion due to respiration in clinical myocardial perfusion SPECT scans using respiratory gating," Journal of Nuclear Medicine **48**, 630-636 (2007).

140   W. Segars, S.P. Mok, B. Tsui, "Investigation of respiratory gating in quantitative myocardial SPECT," Nuclear Science, IEEE Transactions on **56**, 91-96 (2009).

141   H. Ue, H. Haneishi, H. Iwanaga, K. Suga, "Nonlinear motion correction of respiratory-gated lung SPECT images," Medical Imaging, IEEE Transactions on **25**, 486-495 (2006).

142   K. Suga, Y. Kawakami, M. Zaki, T. Yamashita, K. Shimizu, N. Matsunaga, "Clinical utility of co-registered respiratory-gated 99mTc-Technegas/MAA SPECT-CT images in the assessment of regional lung functional impairment in patients with lung cancer," European journal of nuclear medicine and molecular imaging **31**, 1280-1290 (2004).

143   K. Suga, K. Yasuhiko, M. Zaki, T. Yamashita, A. Seto, T. Matsumoto, N. Matsunaga, "Assessment of regional lung functional impairment with co-

registered respiratory-gated ventilation/perfusion SPET-CT images: initial experiences," European journal of nuclear medicine and molecular imaging **31**, 240-249 (2004).

144   K. Suga, Y. Kawakami, M. Zaki, T. Yamashita, T. Matsumoto, N. Matsunaga, "Pulmonary perfusion assessment with respiratory gated 99mTc macroaggregated albumin SPECT: preliminary results," Nuclear medicine communications **25**, 183-193 (2004).

145   S. Nehmeh, Y. Erdi, C. Ling, K. Rosenzweig, O. Squire, L. Braban, E. Ford, K. Sidhu, G. Mageras, S. Larson, "Effect of respiratory gating on reducing lung motion artifacts in PET imaging of lung cancer," Medical physics **29**, 366 (2002).

146   Y. Kawakami, K. Suga, T. Yamashita, H. Iwanaga, M. Zaki, N. Matsunaga, "Initial application of respiratory-gated 201Tl SPECT in pulmonary malignant tumours," Nuclear medicine communications **26**, 303-313 (2005).

147   J.E. Bowsher, S. Yan, J.R. Roper, W.M. Giles, F.-F. Yin, "Onboard Functional and Molecular Imaging: A Design Investigation for Robotic Multi-Pinhole SPECT," Medical physics (Under revision2013).

148   E.L. Kramer, M.E. Noz, "CT-SPECT fusion for analysis of radiolabeled antibodies: applications in gastrointestinal and lung carcinoma," International journal of radiation applications and instrumentation. Part B. Nuclear medicine and biology **18**, 27-42 (1991).

149   O. Schillaci, R. Danieli, C. Manni, G. Simonetti, "Is SPECT/CT with a hybrid camera useful to improve scintigraphic imaging interpretation?," Nuclear medicine communications **25**, 705-710 (2004).

150   S. Vedam, V. Kini, P. Keall, V. Ramakrishnan, H. Mostafavi, R. Mohan, "Quantifying the predictability of diaphragm motion during respiration with a noninvasive external marker," Medical physics **30**, 505-513 (2003).

151   M. Dawood, N. Lang, X. Jiang, K.P. Schafers, "Lung motion correction on respiratory gated 3-D PET/CT images," Medical Imaging, IEEE Transactions on **25**, 476-485 (2006).

152   S. Yan, J. Bowsher, R. Blitzblau, F.-F. Yin, "Prone Breast Imaging for On-Board and Other Applications with a Robotic Multi-pinhole SPECT System: A Simulation Study," Medical physics2014).

153   L. Cheng, Phantom Studies for On-board Biological Imaging by Robotic SPECT, University of Heidelberg Thesis, 2013.

154   I. American National Standards Institute, "American National Standard for Industrial Robots and Robot Systems — Safety Requirements," (Robotic Industries Association, June 21, 1999).

155   F. Noo, M. Defrise, R. Clackdoyle, H. Kudo, "Image reconstruction from fan-beam projections on less than a short scan," Physics in Medicine and Biology **47**, 2525 (2002).

156   J. Li, R. Jaszczak, K. Greer, R. Coleman, "A filtered backprojection algorithm for pinhole SPECT with a displaced centre of rotation," Physics in medicine and biology **39**, 165 (1994).

157   K. Ogawa, T. Kawade, K. Nakamura, A. Kubo, T. Ichihara, "Ultra high resolution pinhole SPECT for small animal study," Nuclear Science, IEEE Transactions on **45**, 3122-3126 (1998).

Biography

Name: Susu Yan

Date of birth: January 25, 1988

Place of birth: Beijing, China

Education

Duke University, Durham, NC

 Medical Physics Graduate Program, Ph.D., expected summer 2014

 Dissertation: "On-board Robotic Multi-pinhole SPECT System for Region-of-interest (ROI) Imaging"

Mount Holyoke College, South Hadley, MA

 Physics, B.A., magna cum laude, 2010

Publications

A. Refereed Journals

1. **S Yan**, JE Bowsher, F-F Yin, "A Line-Source Method for Aligning On-board and other Pinhole SPECT Systems," *Medical Physics*, 40(12):122501, 2013.

2. **S Yan**, JE Bowsher, RC Blitzblau, F-F Yin, "Prone Breast Imaging for On-Board and Other Applications with a Robotic Multi-pinhole SPECT System: A Simulation Study," (Submitted to *Medical Physics*)

3. **S Yan**, JE Bowsher, M Touch, L Cheng, F-F Yin, "A Hardware Investigation of Robotic SPECT for Onboard and Other Functional and Molecular Imaging Applications," (Submitted to *Medical Physics*)

4. JE Bowsher, **S Yan**, JR Roper, WM Giles, F-F Yin, "Onboard Functional and Molecular Imaging: A Design Investigation for Robotic Multi-Pinhole SPECT," Medical physic, 41(1): 010701, 2014.

B. Conference Proceedings

1. JE Bowsher, JR Roper, **S Yan**, WM Giles, F-F Yin, "Regional SPECT Imaging Using Sampling Principles and Multiple Pinholes," In Conference Record of the 2010 IEEE Nuclear Science Symposium and Medical Imaging Conference, 2010:2071-2076, Knoxville, TN, 2010.

C. Selected Abstracts

1. JE Bowsher, **S Yan**, L Cheng, F-F Yin: Robotic SPECT for region-of-interest imaging onboard radiation therapy systems and in other applications, Oral presentation at the 2014 Annual Meeting of the Society of Nuclear Medicine and Molecular Imaging, St. Louis, MO, June 7-11, 2014.

2. **S Yan**, JE Bowsher, M Touch, L Cheng, F-F Yin: A Hardware Implementation and Evaluation of Robotic SPECT: Toward Molecular Imaging Onboard Radiation Therapy Machines, Oral presentation at the 56th Annual Meeting of the American Association of Physicists in Medicine, Austin, Texas, July 20-24, 2014.

3. L Cheng, J Bowsher, **S Yan**, F-F Yin: Computer Simulation Studies for On-Board Functional and Molecular Imaging of the Prostate Using a Robotic Multi-Pinhole SPECT

System, Oral presentation at the 56th Annual Meeting of the American Association of Physicists in Medicine, Austin, Texas, July 20-24, 2014.

4. M Touch, JE Bowsher, **S Yan**, F-F Yin: Effect of Number of Pinholes in Onboard Robotic Multi-Pinhole SPECT System, Poster presentation at the 56th Annual Meeting of the American Association of Physicists in Medicine, Austin, Texas, July 20-24, 2014.

5. **S Yan**, JE Bowsher, F-F Yin: A Simulation Study of Treatment Verification Using On-board Multi-pinhole SPECT, Poster presentation at the 55th ASTRO Annual Meeting, Atlanta, GA, September 22 - 25, 2013.

6. H Li, JE Bowsher, Y Jiang, T Pang, Q Wu, **S Yan**, B Czito, C Willett, F-F Yin: Effects of PET Reconstruction Parameters on Region-of-Interest Contouring by SUV Threshold, Poster presentation at the 55th ASTRO Annual Meeting, Atlanta, GA, September 22 - 25, 2013.

7. **S Yan**, JE Bowsher, F-F Yin: On-Board Robotic Multi-Pinhole SPECT System for Prone Breast Imaging, Oral presentation at the 55th AAPM Annual Meeting, Indianapolis, IN, August 4-8, 2013.

8. **S Yan**, JE Bowsher, F-F Yin: Respiratory Sorted Imaging Using Region-of-Interest Robotic Multi-Pinhole SPECT System, Oral presentation at the 55th AAPM Annual Meeting, Indianapolis, IN, August 4-8, 2013.

9. JE Bowsher, **S Yan**, F-F Yin: Robotic Multi-Pinhole Scenarios for SPECT Molecular and Functional Imaging Onboard and in Other Applications, Oral presentation at the 55th AAPM Annual Meeting, Indianapolis, IN, August 4-8, 2013.

10. **S Yan**, JE Bowsher, F-F Yin: Functional and Molecular Imaging of the Axilla as the Patient Is in Position for Radiation Therapy Using a Robotic Multi-Pinhole SPECT System, Poster presentation at the 54th ASTRO Annual Meeting, Boston, MA, October 28-31, 2012.

11. **S Yan**, JE Bowsher, Will Giles, F-F Yin: A Line-Source Method for Aligning Onboard-Robotic-Pinhole and other SPECT-Pinhole Systems. Oral presentation at the 54th AAPM Annual Meeting, Charlotte, NC, July 29-August 2, 2012.

12. JE Bowsher, **S Yan**, JR Roper, W Giles, F-F Yin: Robotic Multi-Pinhole SPECT System for Onboard and Other Region-of-Interest Imaging. Oral presentation at the 54th AAPM Annual Meeting, Charlotte, NC, July 29-August 2, 2012.

13. **S Yan**, JE Bowsher, F-F Yin: Design of Robotic Multi-Pinhole SPECT for Use Onboard Radiation Therapy Systems. Oral presentation at the World Congress on Medical Physics and Biomedical Engineering, Beijing, China, May 26-31, 2012.

14. JE Bowsher, **S Yan**, JR Roper, WM Giles, F-F Yin: SPECT Imaging Onboard Radiation Therapy Machines. Invited Talk at the SPIE Optics and Photonics: Optical Engineering and Applications: Medical Applications of Radiation Detectors, San Diego, CA, August 21-25, 2011.